2014

Non-Equilibrium Models for High Temperature Gas Flows

Daniil Andrienko
Wright State University

Non-equilibrium Models for High Temperature Gas Flows

A dissertation submitted in partial fulfillment of the
requirements for the degree of
Doctor of Philosophy

By

DANIIL A. ANDRIENKO
Ph.D., Moscow Institute of Physics and Technology, 2013

2014
Wright State University

Wright State University
GRADUATE SCHOOL

May 19, 2014

I HEREBY RECOMMEND THAT THE DISSERTATION PREPARED UNDER MY SUPERVISION BY Daniil A. Andrienko ENTITLED Non-equilibrium Models for High Temperature Gas Flows BE ACCEPTED IN PARTIAL FULFILLMENT OF THE REQUIREMENTS FOR THE DEGREE OF Doctor of Philosophy.

George Huang, Ph.D., P.E.
Thesis Director

Joseph Shang, Ph.D.
Thesis Co-Director

Ramana V. Grandhi, Ph.D.
Director, Ph.D. program

Robert E. W. Fyffe, Ph.D.
Vice President for Research and
Dean of the Graduate School

Committee on
Final Examination

Joseph Shang, Ph.D., WSU

George Huang, Ph.D., WSU

James Menart, Ph.D., WSU

William Bailey, Ph.D., AFIT

Paul King, Ph.D., AFIT

Viswanath Katta, Ph.D., ISS Inc.

ABSTRACT

Andrienko, Daniil. Ph.D., Department of Mechanical and Materials Engineering, Engineering Ph.D. Program, Wright State University, 2014. *Non-equilibrium Models for High Temperature Gas Flows.*

A multi-physical approach is developed for non-equilibrium high enthalpy flows to cover a wide range of interdisciplinary studies. Compressible Navier-Stokes equations are coupled with the chemical model and equation of energy conservation for internal degrees of freedom. The model is capable of accounting for the non-equilibrium dissociation and thermal radiation heat transfer in gas flows. The methodology covers a range of problems from the combustion in subsonic counter-flowing jets to the hypersonic re-entry flows. The present approach attempts to validate the finite rate chemistry mechanisms by modeling the diffusive non-premixed flame of hydrogen at a very low Mach number. The comparison with the artificial compressibility method provides some insights into the compressible Navier-Stokes equations when applied to the flow with nearly constant pressure. High Mach number flow is assessed by a TVD flux splitting scheme applied to model the re-entry of RAM-C II probe. The chemical composition of the air plasma is validated against available experimental and theoretical data. The uncertainty in electron concentration, measured by microwave reflectometers and a Langmuir probe, is examined in the light of chemical reactions, multi-temperature models, boundary conditions and a vibrational-dissociation coupling model. The heating rates are reported on a wide range of trajectory points.

A novel approach is used to improve the accuracy of the radiation transfer model based on the ray tracing method by introducing Gauss-Lobatto quadrature and space partition algorithms to the nearest neighbor search. The accuracy of the method is analyzed for hypersonic flows and for laser-supported combustion waves. The approach revealed an increased efficiency of two orders of magnitude when solving the radiation transfer energy

along the line of sight. Finally, the concept of the view factor is applied to assess the radiation transfer in high temperature absorbing gas flows. This concept was verified against the ray tracing method and demonstrated several important advantages. The semi-analytical solution for the radiation flux density in axisymmetric geometry is obtained in terms of elliptic integrals. The cost of the radiation transfer model based on the view factor approach in weakly absorbing media is comparable with the cost of the tangent slab approximation and achieves the asymptotic accuracy of the ray tracing method.

LIST OF SYMBOLS

ρ	Density of mean flow, kg/m^3
p	Pressure of mean flow, kg/m^3
t	Time, s
$\mathbf{u}$	Convective velocity vector, m/s
$\mathbf{v}$	Vector of diffusion velocity, m/s
$\mathbf{q}$	Heat flux vector, W/m^2
D	Diffusion coefficient of mean flow, m^2/s
E	Total energy of mean flow, J/m^3
H	Total enthalpy of mean flow, J/m^3
$\tilde{\mathbf{E}}$	Vector of electric field, V/m
k	Boltzmann constant, 1.38x10^{-23} J/K
e	Electric charge, 1.60x10^{-19} C
M	Molar mass, kg/mole
N_J	Total number of reaction
λ	Thermal conductivity, W/m/K
Y_i	Mass fraction of species i
X_i	Molar fraction of species i
T	Translation temperature of heavy particles, K
P	Total pressure of mean flow, Pa
x, y	Cartesian coordinates, m
ξ, η	Curvilinear coordinates, m
k_{fk}	Forward rate of reaction k, m^3/s/mol or m^6/s/mol^2
k_{rk}	Backward rate of reaction k, m^3/s/mol or m^6/s/mol^2
K_k	Equilibrium constant of k reaction
μ	Dynamic viscosity, kg/m/s
λ	Thermal conductivity, W/m/K
c_v	Heat capacity at constant volume, J/kg/K
c_p	Heat capacity at constant pressure, J/kg/K
S	Entropy, J/kg/K
θ_ν	Characteristic vibrational temperature, K
U	Empirical parameter in dissociation models, K
i, j	Cartesian grid indexes
κ	Coefficient of absorption, cm^{-1}
J	Spectral intensity of radiation, J cm/s/sr/cm^2
J^{em}	Spectral emissivity, J cm/s/cm^3
J_b	Spectral intensity of the black body, J cm/s/sr/cm^2
$\mathbf{s}$	Vector of spatial coordinates, cm
T	Attenuation factor
Ω	Solid angle, sr
κ_ν	spectral coefficient of absorption, cm^{-1}
τ	Optical thickness

q_ν	Spectral density of radiation flux, W cm/cm^2
A	Surface of participating element, cm^2
V	Volume of participating element, cm^3
subscript	
ν	Spectral index
i, j	Indexes of gasdynamic grid
i	Species index
v	Index of vibrational degree of freedom
m	Index of vibrational mode
tr	Index of translation degree of freedom
rot	Index of rotational degree of freedom
el	Index of electron-electronic degree of freedom

TABLE OF CONTENTS

Page

List of Figures

List of Tables

Acknowledgment

I am very grateful to my advisor Professor Joseph Shang for his constant guidance, support and encouragement. I have been amazingly fortunate to have an advisor who gave me a freedom to explore science on my own and created favorable conditions to do so. I also very pleased with his hospitality and help during my adaptation in a new country and to new conditions.

I would like to thank my co-advisor Professor George Huang, who was always there to give me an advise. His guidance for the computer program TURCOM is deeply appreciated.

I am also indebted to the members of my committee: Professor James Menart, Professor William Bailey, Professor Paul King and Dr. Viswanath Katta for their valuable comments on my research proposal. I also appreciate knowledge and recommendations on the combustion of hydrogen Dr. Katta shared with me in the beginning of my work.

I am also thankful to Professor Sergey Surzhikov for his valuable comments on radiation transfer models and opportunity to use computer code ASTEROID.

Last but not least I would like to thank my family and Samane. They provided me with all the support and love that I needed.

Dedicated to Samane

1. INTRODUCTION

1.1 Motivation and goals

The goal of the proposed study is motivated by the growing interest in developing, validating, and improving existing models for high enthalpy gas flows in engineering and aerospace applications. General features of these problems are the chemical and thermodynamic non-equilibrium conditions as well as the radiation transfer. The significant amount of experimental and theoretical data is accumulated up to now. A substantial portion of current studies has been utilized to address the correlation between experimental results and conventional theoretical models as well as to develop a unified approach for the non-equilibrium phenomena at atomic and molecular scales in high energy gas flows.

The present approach attempts first to increase the range of practical applications from subsonic to hypersonic domain by loosely coupling the finite rate chemical model to the compressible Navier-Stokes (N-S) equations. In this sense the diffusive flames at a low Mach number are probably the most suitable approach to develop and verify a numerical procedure for a multi-physical combustion model.

The combustion in counter-flowing hydrogen-air jets is the classic approach for studying the diffusive flame (Bilger, 1976; Katta et al., 2007; Katta and Roquemore, 2008; Shang and Surzhikov, 2010). As the velocity of the fuel and oxidizer increases, the flame becomes stretched and its temperature decreases. The flame becomes unstable as the global strain rate approaches the flame-extinction process. Stable flame of hydrogen in the counter-

flowing jets occurs typically at a Reynolds number based on the nozzle diameter less than one thousand. At an ambient temperature of 300 K, the Mach number is less than $2x10^{-3}$. One of the aims of the present study is to duplicate the physical behavior of the hydrogen flame by adopting the finite rate chemistry module that is loosely coupled with compressible Navier-Stokes equations.

The flow at the low Mach number is nearly incompressible and the numerical approach typically adopted for this type of flow is different from the methods describing compressible fluid flows (Anderson et al., 2012). The most widely used solving scheme for incompressible Navier-Stokes equations has its root in the method of artificial compressibility by Chorin (1967). The hydrogen diffusion flame in counter-flowing jets at a subsonic speed using the conventional numerical method has been successfully modeled by means of a projection method with a direct solver in (Katta et al., 2007; Katta and Roquemore, 2008). The projection approximation is achieved through the continuity equation by coupling the pressure with velocity components iteratively by the Poisson formulation. The Poisson equation is then solved directly using the matrix inversion method in conjunction with the lower and upper decomposition technique at every time step. This approach is efficient in simulating stiff kinetic models with a large set of chemical reactions.

In the present approach, compressible Navier-Stokes equations are loosely coupled with the finite rate chemistry and solved by the basic scheme of the ADI (alternating direction implicit) in the delta formulation (Beam and Warming, 1978; Douglas and Gunn, 1964). The main reason for adopting this formulation is that the numerical accuracy can be drastically improved by a diminishing residual method. The right-hand-side (RHS) and the left-hand-side (LHS) of governing equations are solved by different algorithms. The

RHS is required only to maintain the computational stability in the process of driving the residual to a minimum, and the LHS produces a high resolution of the solution whenever the residual of the differencing approximation vanishes (Shang et al., 2010).

Three chemical kinetic models of hydrogen flame are employed in the present study: global single-step model, Gas Research Institute model (GRI version 3.0), (Smith et al., 1999) and the model by (Evans and Schexnayder, 1980). A chemical model derived from the GRI data set has also been used in a reference solution by (Katta and Roquemore, 2008) for describing the hydrogen-air combustion in the counter-flowing jets. This model consists of 13 species, namely H_2, O_2, H, O, OH, H_2O, HO_2, H_2O_2, N, NO, NO_2, N_2O, N_2, and 74 elementary reactions. However, by examining the chemical composition of the flame, a further simplification excluding N_2 derivatives is suggested, since these species appear only in the trace amount.

The validation of the adopted approach in high Mach number flows is provided by modeling the hypersonic flow at the orbital re-entry. The flow generated in the vicinity of a spacecraft possess significantly different physical features comparing to the combustion process in the incompressible flows. It becomes necessary to model dissociation and ionization in the low temperature air plasma and account for the thermodynamic nonequilibrium and radiation transfer behind the shock wave. Numerical models of these flows appear to be a complex problem involving different physical backgrounds. The verification of models has to be done thoroughly in many aspects according to the flow field structure. For these purposes the re-entry experiment of RAM-C II probe is chosen for the present effort. The reason is that the re-entry occurs at a moderate hypersonic velocity allowing the implementation of multi-temperature models, which are among present interests. Addition-

ally, a significant amount of theoretical data and experimental measurements is available up to now. However a certain diversity exists in published results. The present effort attempts to understand the uncertainty of the numerical result due to various components of the multi-physical model.

The simulation of non-equilibrium radiative gas flow is built on the coupling phenomena of quantum physics, aerothermodynamics and radiation transfer. Most of the chemical-physical phenomena occur at the atomic scales abandoning the classical physics approach (Capitelli et al., 2000; Michalak and Ollivier-Gooch, 2008; Surzhikov, 2002; Zeldovich et al., 1985). Meanwhile, one of most challenging problems is the modeling of the radiation heat transfer in high temperature non-equilibrium flows. The reason is that the radiation is tied to almost all components of flow physics. The transfer of radiation energy follows the line-of-the-sight path of electromagnetic waves. The emission and absorption of the radiative energy take place during quantum transitions, and the optical property is exclusively tied to the local thermodynamic state and compositions of the flow medium. The most accurate radiation transfer models naturally describe quanta propagation on two intrinsically different systems of coordinates and are computationally inefficient for accurate engineering applications.

The thermal radiation of gas medium typically is in the spectrum defined from 1000 to 150,000 cm^{-1} of wavelength. The spectral range of thermal radiation starts from the far-infrared to near-infrared domain for rotational degrees of excitation, then shifts to the near-infrared and the lower limit of visible spectrum for vibrational degrees of excitation. Finally the electronic degrees of excitation occupy the spectra from visible to violet and fringe onto the ultraviolet wavelength (Goody and Yung, 1996; Siegel and Howell, 2002).

The spectra of possible quantum transitions in a high temperature gas are overlapped by the relaxation of energy between internal degrees of freedom (DOF) of atoms and molecules. It is important to note that free electrons play the dominant role in the excitation and emission processes because of the relatively efficient collisions of atoms or molecules with electrons rather than with other neutral particles and ions (Zeldovich et al., 1985).

In engineering and aerospace applications the most efficient and accurate approach for solving the radiative transfer equation (RTE) is based on statistical mechanics by following the progress of discrete amounts of energy. A very wide range of approximations for solving the radiation transfer equation has been developed from the classic tangent slab (TS) approximation and spherical harmonic method (SHM) to the most rigorous and accurate ray tracing method (RTM) (Siegel and Howell, 2002; Surzhikov, 2002). The high physical fidelity of the radiation simulation however is achievable only by an accurate and compatible description of the thermodynamically non-equilibrium flow and an RTE solution procedure. An attractive approach for solving the RTE is exemplifying by the ray tracing technique derived from the Monte-Carlo method (Galvez, 2005; Kong et al., 2008). The basic idea of the RTM is the line of sight solution of the RTE as well as the determination and interpolation of the optical and thermodynamic data on the tracing ray.

In order to include the most pertaining optical model, the amount of data to be transferred and processed is enormous for an acceptable engineering prediction of radiation energy and flux density. In Earth re-entry, wherein the spectral computations are in the wavelength range from 80 to 1,400 nm, nearly 10^4-10^5 spectral lines are required to provide an adequate representation of the radiating spectrum. The Voigt profile of line is usually described by at least 10 discrete points. Then nearly 10^6 spectral points are processed just

for a simple 11 species air models (Olynick et al., 1999; Surzhikov, 2004b). The radiative field may not always have a weak dependence on the numbers of spectral groups; thereby, the number of optical groups must be increased to meet the accuracy requirement. For the most existed modeling and simulation procedures, a low resolution numerical algorithm was often adopted but focused on the complex and intricate physics. As the consequence, a substantial improvement to the computational efficiency becomes a pacing item.

A new approach is addressed to remove the deficiency in the existing radiation transfer model based on the ray tracing method by a combination of a more efficient nearest neighbor search (NNS) algorithm for interpreting emission data from the flow field onto tracing rays and an advanced high-resolution orthogonal polynomial refinement technique for the radiation computation. The adopted Gauss-Lobatto polynomial refinement technique (Carnahan et al., 1969; Gautschi, 2004) will not only reduce the required number of points along the tracing ray for computational accuracy, but also concentrate the grid density in the regions of active radiative transition. Previously, Gauss-Lobatto quadrature has been successfully applied to resolve the thin flame structure in the hydrogen-air combustion problem (Shang et al., 2010).

Most importantly, a more efficient optimization problem for the nearest neighbor search is built on the space partition concept. The basic idea is eliminating the unnecessary searching domain that will drastically reduce the computer query time along tracing rays (Arya et al., 1994; Fridman, 2008; McNames, 2001). The merit of the developed technique is verified by the comparative studies with the conventional methodology referred to as brute algorithm, when search is performed over the entire grid.

One of the drawbacks of the ray tracing method is the approximation of thermody-

namic properties from the fundamental Cartesian grid onto the tracing ray. An alternative to the RTM is the view-factor (VF) approach. The viable feature of the VF approach is the direct calculation of the radiation transfer between elementary surfaces and volumes formed by the Cartesian grid that contain originally computed thermodynamic and optical properties. In the case of optically thin media the problem of NNS is completely eliminated and the VF approach is expected to demonstrate the overwhelming efficiency compared to the RTM. The possibility to obtain analytical form of the view factor is another distinct advantage of the VF approach.

1.2 Specific aims

1. Develop and integrate the finite rate chemistry module with the compressible Navier-Stokes equations to verify the proposed approach by investigating the physical behavior of the hydrogen-air flame at different strain rates.

2. Develop a multi-temperature model to describe the chemical composition of the air plasma and heating rates on the surface of a re-entry spacecraft. Validate the model against the experimental data and explore the uncertainty due to the different components of the multi-physical model.

3. Investigate the opportunity to apply Gauss-Lobatto quadrature to solve the radiation transfer equation along the selected direction. Explore the advantages of the RTE solution by quadrature in the problem of laser-supported combustion waves and re-entry of a space vehicle.

4. Develop a space partition algorithm for the nearest neighbor search on grids with different topologies. Integrate an improved search algorithm with the quadrature integration of the RTE into the unified approach.

5. Explore the concept of the view-factor approach for the RTE solution. Perform the comparison of accuracy and efficiency with the existing radiation transfer models.

1.3 Thesis proposal structure

The structure of the present work is as follows. First, Chapter 2 introduces the background of the adopted approach. It provides the description of the developed research methodology to analyze the flame structure at a low Mach number and the extension of the approach to capture Earth entry phenomena including the radiation transport. Chapter 3 provides the results of the flame structure and validates it against the conventional incompressible approach. The analysis of the non-equilibrium flow field around the RAM-C II probe at different altitudes in the Earth atmosphere is given in Chapter 4. The assessment of the efficiency of the ray tracing method and accuracy by means of Gauss-Lobatto quadrature is presented in Chapter 5. The view-factor approach is generalized to calculate the radiation flux on a surface of space vehicle and in laser-supported combustion waves in Chapter 6. Finally, Chapter 7 summarizes the developed approach and provides recommendations on its efficiency and the range of applicability.

2. BACKGROUND AND RESEARCH METHODOLOGY

2.1 Introduction

The core features of problems formulated by the modern science lay at the intersection of multiple disciplines of physics. The aerospace science also inherits the multi-physical aspects of goals due to relatively recent breakthroughs in the knowledge in physical chemistry (Capitelli et al., 2000), quantum mechanics (Dirac, 1981), flight technologies (Shang, 2001) and computational methodologies (Shang, 2004).

Generally speaking, the problems that involve high speed gas flows and conversion of the kinetic energy into the thermal motion of particles require the formulation of a chemical model to resolve the species composition in the control volume and at the gas-solid boundary interface. The rate of chemical reactions has an exponential dependence on temperature and significantly changes the properties of the gas flow in the region of active chemical transformations. The range of such problems spans widely from the essentially laminar diffusive flames to the hypersonic flights in the Earth's atmosphere.

The chemical model is inevitably coupled with the thermodynamics and kinetics of the fluid. Generally speaking, transport and thermodynamic properties of individual species as well as the mixture of gases has to be calculated in order to solve governing equations of the fluid flow. At this level of multi-physical problem the such disciplines as statistical mechanics, thermodynamics and kinetic theory are involved. The partition functions and solution of Boltzmann equation are generally required to assess gas properties at conditions

different from room temperature.

Aerospace applications are associated with flight at high velocity. It is known that at a Mach number higher than four the process of dissociation in the vicinity of the vehicle occurs. The number of physical processes involved in the problem formulation grows with the flight velocity. As a matter of fact, the ionization and non-equilibrium excitation of the internal degrees of freedom occur at a higher Mach number (Park, 1989).

The process of excitation and relaxation of electronic, rotational and vibrational degrees of freedom leads to radiation energy exchange between molecules and atoms behind the shock wave. The radiation phenomenon effects the heating rates on the surface of space vehicle and disturbs the population of energy levels of species immediately behind the shock front and in the relaxation zone. The latter is known as the radiative cooling (Goulard, 1961). The radiation heating and cooling are two phenomena that play important role in the aerospace physics.

The radiation properties of participating media are strongly dependent on the temperature, pressure, gas composition, wavelength and spectroscopic properties of gas and plasma (Goody and Yung, 1996; Surzhikov, 2003). This fact indicates that the standard tools of quantum chemistry and quantum mechanics are inevitably involved to obtain absorption and emission coefficients of electromagnetic radiation.

It is worthwhile to note that the increasing complexity of physical models demands higher and more accurate numerical methods to solve the coupled problem. It is a great challenge to match the adopted physical and numerical models and to quantify the uncertainty to analyze and process the results.

The numerical model employed to capture chemical transformation in the gas mixture

plays an important role and is subject to verification. While the entry problem of spacecraft is a multi-physics problem with the uncertainty caused by different factors, the combustion in the counter-flowing jets can be used for the verification of chemical and transport properties of gas mixture model. The diffusive mechanism of flame formation at low Mach number serves as a classical tool for chemical model verification (Bilger, 1976).

The organization of this chapter proceeds as follows. The Section 2.2 presents the concept of diffusion flames as it is the classical tool for understanding chemical transformations at a very low Mach number. The Section 2.3 presents high Mach number re-entry problem for gas flows when chemical reactions play an important role. Section 2.4 presents the governing equations of the continuum gasdynamics. The formulation of Navier-Stokes equations, mass conservation of the mean flow and individual species and energy conservation are included. Conventional methods for transport properties are described in Section 2.7. The boundary conditions imposed for flow variables, species and parameters describing internal degrees of freedom are given in Section 2.8. The important aspects of radiation transfer in hypersonic flows, such as optical and spatial models are presented in Section 2.9.

2.2 Diffusion flames

The concept of the diffusion flame as well as the properties of non-premixed flames are significantly different from the situation where fuel and oxidizer are initially premixed and delivered to the reaction zone. When the fuel/oxidizer ratio and thermodynamic conditions are defined, the properties of the premixed flames are uniquely defined. However, in the

situation of non-premixed reactants, the flame properties also depend on the aerodynamics of the reacting flows. Thereby, the diffusion flame opens a broader range of possible configurations and physical conditions (Tsuji, 1982).

One of the simplest and, at the same time, effective methods to assess some properties of the diffusion flame is the concept of the *flame sheet*. First introduced by Burke and Schumann (1928), this concept rests on the assumption of an infinitesimally short reaction time of reactants. In other words, the reaction zone in flame sheet concept is represented as a infinitesimally thin area with zero concentrations of fuel and oxidizer on the opposite sides of reactants.

The main disadvantage of the flame sheet concept is that the extinction of the flame can not be described within the framework of this approach. In order to be able to capture the extinction phenomenon the characteristic time of reaction has to be finite compared to the time of the flow passing the burner zone. In this sense the more rigorous approach which allows to implement the concept of the finite rate chemistry is required.

Apparently, one of the first works intended to describe the shape, properties and chemical composition of the diffusion flame is the paper by Burke and Schumann (1948). The two coaxial tubes carrying the air and fuel have been theoretically investigated by the equation of diffusion in an axisymmetric geometry. Some essential simplifications of the flow configuration have been made. This includes the constant flow velocity and diffusion properties as well as negligible contribution to mass transfer by the convective component and diffusion in the axial direction. However, despite that some of these assumption may be improbable, the author accurately predicted the chemical composition of under- and overventilated flames, compared with the experiment.

With the progress in computational technologies more sophisticated models of diffusion flames have been incorporated. Some of noteworthy works in this field have been done by Katta et al. (1994); Kirkbey and Schmitz (1966); Mitchell et al. (1980); Peters (1984); Roper (1977); Smooke et al. (1986). Modern multi-dimensional models of non-premixed flames include the appropriate treatment of diffusion phenomenon, heat conduction and heat losses, finite rate chemistry, soot formation, sensitivity analysis, turbulence and radiation transfer (Tsuji, 1982).

One of the classical tools to study diffusion flames is when fuel and oxidizer are brought together by the counter-flow jets. The configuration consists of two coaxial opposed tubes. The schematic of the counter-flowing jets is given in Fig. 2.1. The jets of gaseous reactants can form the pure diffusion flame since the fuel and oxidizer decelerate down to the rest at the stagnation point. This is an efficient tool for studying the detailed composition of the flame and global rate of the combustion process.

Because of the extinction of the diffusion flame at high speeds of jets, the flame is usually studied at a very low Mach number. At this speed the gas flow is nearly incompressible. Over the years a number of approaches have been proposed to solve the incompressible Navier-Stokes equations. One of the earliest methods is artificial compressibility method by Chorin (1967). The key idea of this method is to introduce the artificial compressibility of the flow:

$$p^\star = \beta \rho^\star,$$

where the parameter β is to be defined. The analysis of eigenvalues for the mixed parabolic-

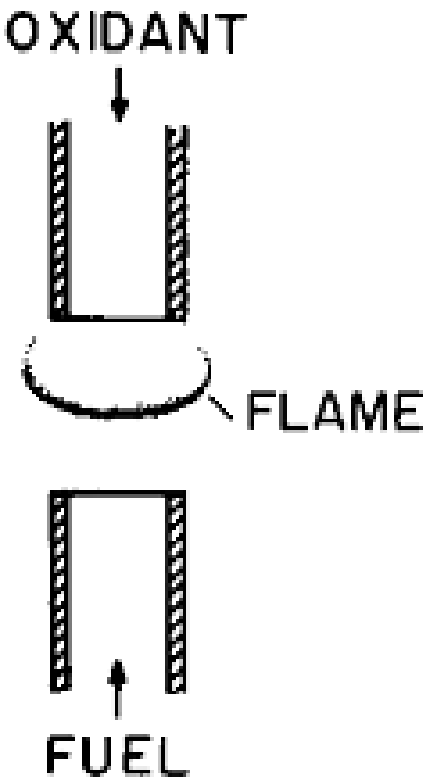

Fig. 2.1: Schematic of counter-flow jets flow, credit Tsuji, 1982

hyperbolic system of governing equations gives the following result:

$$\lambda_u = \left\{ u, u, u \pm \sqrt{u^2 + \beta} \right\}.$$

In order to retain the similarity to the incompressible flow the parameter β has to be chosen close to the convective velocity. A value in the range of 0.1 - 10 is generally adopted (Kwak et al., 1986). Since the time parameter is modified appropriately, the artificial compressibility method cannot be used for transient problems.

Another method to obtain steady-state solution of incompressible Navier-Stokes equa-

tions is the pressure correction approach (Harlow and Welch, 1965), when the momentum equations are solved using the best available approximation for the pressure field. Generally, the Poisson equation is used for this purposes:

$$\nabla^2 p = 2\rho \left(\frac{\partial u}{\partial x} \frac{\partial v}{\partial y} - \frac{\partial u}{\partial y} \frac{\partial v}{\partial x} \right) \tag{2.1}$$

Equation (2.1) can be obtained within the framework of the vorticity-stream function approach (Pletcher et al., 2012). The pressure correction method was used in recent studies for the flame composition in counter-flowing jets (Katta et al., 2007).

The chemical reaction occurs over a wider range of flow velocities that the above mentioned techniques are applicable to. The approach of the compressible Navier-Stokes equations is adopted in present work to extend the conventional approach of high speed flows to the low Mach number limit. An efficient alternating direction implicit scheme in the delta formulation is able to generate a high order accurate solution whenever the residual of errors is driven to zero. The proposed approach is validated against the classical artificial compressibility method by comparing the flame thickness, species composition and extinction conditions with the existed data (Katta, 2011).

2.3 Hypersonic flow

An important class of problems where the chemical composition is critically important is the shock heated flows in aerospace and aerodynamic applications. The flight of hypersonic airplane or the re-entry of the space vehicle are the examples of the problem where the chemical reactions and thermodynamics of the excited internal degrees of particles in the

flow are critical. At a Mach number higher than four, chemical transformations in the flow occur (Park, 1989). At first the dissociation of the flow happens. By the increasing velocity of the vehicle the amount of kinetic energy of the incoming flow converted into the thermal energy of gas is inevitably increasing. When a significant fraction of molecules break up into atoms, free electrons are born by collision process between atoms. This mechanism is called the associative ionization and it is the major reason for the presence of free electrons behind the shock front at moderate velocities ($V_\infty < 10$ km/s) (Josyula and Bailey, 2003). This situation takes place at the re-entry of space vehicle at the orbital velocity. At superorbital entry the ionization by electron impact mechanism prevails (Bose and Candler, 1997). Internal thermal energy contained in the flow around spacecraft is not sufficient to ionize particles more than once, but the nearly total dissociation of molecular species may take place.

Besides the chemical transformations taking place in the flow heated by shock wave, the hypersonic flows may encounter the phenomenon of non-equilibrium excitation of internal degrees of freedom in the gas as well as emission and absorption of radiation in high temperature gas. A significant amount of work has been done in the direction of accurate and effective prediction of hypersonic flowfield. However the development and validation of high fidelity models of non-equilibrium, state resolved air chemistry and radiation process of particular atomic and molecular transitions are still subject to intense investigation.

The approach which allows to create high fidelity models of hypersonic flow has to combine itself in several areas of knowledge databases such as computational fluid dynamics, continuum mechanics of fluids, thermodynamics, chemistry, quantum physics, radiation gasdynamics, statistical physics and etc. The structure of the present chapter reflects

some of these aspects as required for creation of a model intended to access the flowfield of the re-entry vehicle.

2.4 Governing equations of gasdynamics

The gas flow can be characterized by the set of nondimensional parameters. Among them the two are always important: the Reynolds number, Re, equal to the ratio of viscous and inertial forces acting in the flow and the Mach number, M, equal to the ratio of fluid speed to the speed of sound.

Low Reynolds number simply means that the flow can be considered as laminar and the natural perturbations in the flow are dumped by viscous forces. As Reynolds number increases, the role of perturbations in the flow increases too and at some critical value of Re the flow becomes turbulent. The stochastic behavior of the flow can be described by random generation and dissipation of eddies at different scales. The fundamental theorem by Kolmogorov (Landahl and Mollo-Christensen, 1992) states that in order to accurately describe the turbulent flow, the structure of the flow must to be resolved up to finite size $\eta_k = \left(\nu^3/\epsilon\right)^{1/4}$, where ν is the kinematic viscosity and ϵ is the average rate of dissipation of turbulence kinetic energy per unit mass. The scale η_k is so small that the direct models (DNS) (Moin and Mahesh, 1998) of the turbulent flow still present problems for modern computational capabilities. Instead of this, some other techniques have been proposed in order to model the presence of turbulence in the flow or to resolve some specific scales of the turbulent motion.

The turbulent phenomenon is present in combustion as well as in the re-entry of a

descending space vehicle, which are considered in the present research. However many theoretical works attempt to avoid the inclusion of turbulence model in their study and concentrate on the physical and chemical aspects of the problem in the stagnation point. For example, in case of counter-flowing jets the turbulence phenomenon can be omitted from the study if the inlet velocity of two jets is small and Reynolds number is below its critical value.

The study of the spacecraft re-entry in principle should include the turbulent model, since the heating rates are strongly affected by the turbulent mixing in the flow (Olejniczak et al., 2003). However, a significant amount of investigations on the entry problem do not introduce the turbulence model but rather concentrate on the chemical composition near the stagnation point. This is explained by a low Reynolds number in the stagnation region and strong favorable pressure conditions, which delay the laminar-turbulent transition. It is therefore the same approach of present study.

The Mach number defines the numerical approach to be used to solve governing equation of gas dynamics. However, equations themselves are essentially the same for any type of the flow and are described in the following section. The Navier-Stokes equations together with the species mass conservation and equation for internal energy conservation are the main frame of the present approach. The conservation equation of the total energy is expanded to the energy conservation equations with individual internal degrees of freedom. The latter is the conventional multi-temperature approach that is often used in the physics of hypersonic flow (Anderson, 1989).

Mass conservation

Mass conservation of the mean flow is formulated as follows:

$$\frac{\partial \rho}{\partial t} + \frac{\partial}{\partial x^j}\left(\rho u^j\right) = 0. \tag{2.2}$$

Equation (2.2) is valid for the entire range of Mach number and in case of incompressible flow can be simplified to:

$$\frac{\partial}{\partial x^j}\left(u^j\right) = 0. \tag{2.3}$$

The mass conservation of individual species is written in the form similar to Eq. (2.2) form:

$$\frac{\partial \rho_i}{\partial t} + \frac{\partial}{\partial x^j}\left(\rho_i u^j\right) = \frac{\partial}{\partial x^j}\left(\rho_i v_i^j\right) + \dot{\omega}_i,\ i = 1...N_c \tag{2.4}$$

The first term in the right hand side of Eq. (2.4) represents the diffusive flux of species i due to the diffusion velocity $\mathbf{v}_i$. There are a number of ways to evaluate the diffusion flux (Coffee and Heimerl, 1981). The theory of mass and heat transport was extensively developed for the past four decades and the accurate approach is available (Hirshfelder et al., 1964). However, the straightforward application of general formalism is computationally expensive, especially in the case of large number of reactants, such as complex hydrocarbon fuels. Some approximations intended to simplify the calculation of the transport properties have been developed (Dixon-Lewis, 1979; Warnatz, 1981). The details of the adopted formulation are given in the corresponding section.

Momentum conservations

The conservation of the momentum of the mean flow is given by the Navier-Stokes equations:

$$\frac{\partial}{\partial t}\left(\rho u^i\right) + \frac{\partial}{\partial x^j}\left(\rho u^j u^i\right) = -\frac{\partial p}{\partial x^i} + \frac{\partial \tau^{ij}}{\partial x^j}, \tag{2.5}$$

where the stress tensor τ^{ij} is dependent on the dynamic viscosity μ:

$$\tau^{ij} = \mu\left[\frac{\partial u^i}{\partial x^j} + \frac{\partial u^j}{\partial x^i}\right] - \frac{2}{3}\mu\frac{\partial u^k}{\partial x^k}\delta^{ij}. \tag{2.6}$$

Energy conservations

The conservation of the total energy of the mean flow is given by Eq. (2.7):

$$\frac{\partial \rho E}{\partial t} + \frac{\partial}{\partial x^j}\left(\rho u^j H\right) = -\frac{\partial q^j}{\partial x^j} + \frac{\partial}{\partial x^j}\left(u^j \tau^{ij}\right) - \frac{\partial q^j_{rad}}{\partial x^j}, \tag{2.7}$$

where the total energy E includes the standard enthalpy of species formation and kinetic energy of the flow:

$$E = \sum_{i \in S} y_i \left(\Delta h^f_{i,0} + e_i\right) + \frac{u^i \cdot u^i}{2}. \tag{2.8}$$

The thermal energy e_i of species i includes translational, rotational, vibrational and electronic components:

$$e_i = e_{tr,i} + e_{rot,i} + e_{v,i} + e_{el,i}, \tag{2.9}$$

$$e_{tr,i} = \frac{3}{2}\frac{R}{M_i}T, \quad e_{tr,el}\frac{3}{2}\frac{R}{\mu_{el}}T_{el},$$

$$e_{rot,i} = \frac{2+\chi}{2}\frac{R}{M_i}T,$$

$$e_{v,i,m} = \frac{R}{M_i}\frac{\theta_{i,m}}{exp\left(\theta_{i,m}/T_{vib,i,m}\right)-1},$$

$$e_{e,i} = \frac{R}{M_i}\frac{\sum_j g_{i,j}\theta_{i,j}exp\left(-\theta_{i,j}/T_e\right)}{\sum_j g_{i,j}exp\left(-\theta_{i,j}/T_e\right)}, i \in N_c,$$

where χ is equal to -2 for monoatomic, 0 for diatomic and 1 for triatomic species. The vector of heat flux $\mathbf{q}$ in Eq. (2.7) includes the effect of thermal conductivity and diffusivity:

$$q^j = q^j_{cond} + q^j_{i,diff} = \lambda\frac{\partial T}{\partial x^j} + \sum_{i\in S}\mathbf{j}^j_i h_i \tag{2.10}$$

Sometimes it is convenient to use the conservation energy equation only for translational and rotational modes. The physical base of this formulation is in the fact that the translational and rotational degrees of freedom are fully exited at very low temperatures, while vibrational and electronic degrees of freedom are active at much higher temperatures. The mathematical convenience of such modification is that the translational and rotational energy have linear dependence on temperature and the heat flux $\mathbf{q}$ can be easily linearized along the vector of primitive variables. This approach is adopted in the present work to build the numerical scheme for Eq. (2.2), (2.5) and (2.7) and is described in Huang and Coakley (1992). Following this approach, the energy equation can be written in the following form:

$$\frac{\partial \rho E_{tr-rot}}{\partial t} + \frac{\partial}{\partial x^j}\left(\rho u^j H_{tr-rot}\right) = -\frac{\partial q^j_{tr-rot}}{\partial x^j} + \frac{\partial}{\partial x^j}\left(u^j\tau^{ij}\right) - Q_{vT} - Q_{eT} - \frac{\partial q^j_{rad}}{\partial x^j}, \tag{2.11}$$

where

$$E_{tr-rot} = \sum_{i \in N_c} Y_i \left(e_{tr,i} + e_{rot,i} \right),$$

$$H_{tr-rot} = \sum_{i \in N_c} Y_i \left(e_{tr,i} + e_{rot,i} \right) + \frac{p}{\rho},$$

$$q^j_{tr-rot} = q^j_{cond,tr-rot} + q^j_{i,diff,tr-rot} = \lambda_{tr-rot} \frac{\partial T}{\partial x^j} + \sum_{i \in S} \mathbf{j}^j_i h_{i,tr-rot},$$

where $h_{i,tr-rot}$ is the species enthalpy only for translational and rotational modes.

The contribution of the radiation losses in the RHS of Eq. (2.7) and (2.11) is, strictly speaking, incorrect. It is more appropriate to include the fraction of this term into the conservation of vibrational and electron-electronic energy, since the emission and absorption of radiation quanta are observed also for vibrational and electronic levels. The accurate distribution of this term due to radiation transfer modes requires quantum-mechanical computations and, in general, involves the state-to-state approach, which is out of the scope of the present work.

Vibrational energy conservation

Because of the equilibration lag between the vibrational and translational modes in a strong shock wave or in the rarefied gas flows, the conservation equation of vibrational energy is often solved separately from the governing conservation laws. The particular formulation should involve models of internal modes for energy exchange and account for the sink and source of vibrational energy due to reactions of molecule dissociation and recombination. All these models have some degrees of uncertainty and require rigorous investigation of their individual contribution. The governing conservation equation of the vibrational en-

ergy in vibrational mode m of molecule i is formulated as follows:

$$\frac{\partial}{\partial t}\left(\rho_i e_{v,i,m}\right) + \frac{\partial}{\partial x^j}\left(\rho_i e_{v,i,m} u^j\right) = +$$
$$\frac{\partial}{\partial x^j}\left(\rho \sum_{i=mol} h_{v,i} D_i \frac{\partial Y_i}{\partial x^j}\right) + Q_{vT} - Q_{ev} + Q_{vv'} + D_{v,i,m}\dot{w}_i, \tag{2.12}$$

where terms Q_{vT}, Q_{ev} and $Q_{vv'}$ describe the relaxations processes of vibrational mode with translational, electron-electronic and vibrational modes of other molecules. The last term in Eq. (2.12) is called the vibrational reactive term and accounts for the sink and generation of vibrational energy due to molecule dissociation and recombination. Several empirical models have been proposed in literature to estimate the vibrational reactive term (Gnoffo et al., 1989; Park, 1988; Sharma et al., 1988). In Park (1988) it was proposed that the energy $D_{v,i,m}$ should account for the energy gain or loss and thus is related to the dissociation energy $\tilde{D}$:

$$D_{v,i,m} = \tilde{D}_{v,i,m} - kT. \tag{2.13}$$

It is assumed in Eq. (2.13) that the vibrational energy loss due to dissociation is less than dissociation energy $\tilde{D}$ of corresponding molecule by the average energy of translational motion. For a dissociation occurred from the high vibrational levels the model by Eq. (2.13) is close to reality, however it tends to substantially underestimate the translational temperature for the relaxation zone and overestimate for the boundary layer, where the recombination occurs. A similar to Eq. (2.13) expression is proposed in Gnoffo et al. (1989):

$$D_{v,i,m} = C\tilde{D}_{v,i,m}, \tag{2.14}$$

where it is recommended to take constant C in the range between 0.3 - 0.8. However, Eq. (2.14) is quite inaccurate to account for the dissociation or recombination involving either low or high vibrational levels, depending from the value of C.

Another model is used in Surzhikov (2014) and accounts only for the sink of vibrational energy. The vibrational reactive term has appearance $e_{v,i,m}\left(\dot{w}_i - |\dot{w}_i|\right)$ and thus equals to zero when molecule is formed. It is assumed that molecules are generated at the ground state. However the simple model

$$D_{v,i,m} = e_{v,i,m} \tag{2.15}$$

is recommended in Gnoffo et al. (1989) if the non-preferential dissociation model is applied. Relaxation terms $Q_{vv'}$, Q_{vT} and Q_{ev} in Eq. (2.12) are described in the Section 2.6.

Electron-electronic energy conservation

Because of a great difference in mass, the thermal energy of free electrons can be significantly different from the energy of heavy particles. Under the equilibrium conditions it is assumed that the free electron temperature is equal to the translation temperature of heavy particles. This approach is referred to as the one-temperature model.

However at non-equilibrium conditions the populations of electronic and vibrational levels can be different from Boltzmann distribution at a translational temperature of heavy particles. Since the interaction of free electrons with vibrational mode of molecules and with bounded electrons on the electronic levels of particles is very efficient, it is often assumed that T_e follows T_v in a shock wave and in a relaxation zone. For the re-entry

problem it is found that the cross section of $N_2 - e$ interaction is two orders of magnitude larger than $O_2 - e$ and $NO - e$. Thus it is assumed that T_e = T_{v,N_2}. This model is referred to as the two-temperature model (Park, 1988).

Recent experimental data (Bourdon and Vervisch, 1997; Domingo et al., 1995) on vibrational-electron relaxation indicates that the relaxation time between vibrational mode of N_2 and free electrons is comparable to the characteristic time of the flow. Thus the energy is carried by free electron gas should be modeled separately. The multi-temperature model that assumes different translational-rotational, vibrational and free-electron temperature is usually called three-temperature model.

The governing equation for the free electron energy is given by Eq. (2.16):

$$\frac{\partial}{\partial t}\left(\rho e_e\right) + \frac{\partial}{\partial x^j}\left(u^j\left(\rho e_e + p_e\right)\right) = \frac{\partial}{\partial x^j}\left(v_e^j\left(\rho e_e + p_e\right)\right) + N_e e\tilde{E}_j\left(u^j + v_e^j\right) + Q_{eT} + Q_{ev} - Q_{imp-ioniz} - Q_{imp-diss} + Q_{ass-ioniz}, \tag{2.16}$$

where the second term in the left hand side and first term in the right hand side describe the enthalpy transfer of free electrons due to the convection and diffusion, second term in the right hand side describes the change of energy due to the presence of the electric field and the last five terms are included for the relaxation of translational-electron mode, vibrational-electron mode and loss of free electron energy due to the chemical reactions, respectively.

Note, that in general, the equation for the electric field potential has to be solved in order to account for the electrostatic force acting on charged particles. The potential ϕ of

the electric field is governed by Poisson equation:

$$\epsilon_0 \nabla^2 \phi = -\sum_{i \in \Omega_c} N_i q_i, \tag{2.17}$$

where Ω_c is all charged species, q_i is a charge of particular species. The electric field can be calculated as $\tilde{E}^i = -\partial\phi/\partial x^i$. However the numerical solution of Eq. (2.17) is often tedious and does not necessarily benefit the overall accuracy of the solution.

A number of simplifications can be used to estimate the contribution of the electric field in Eq. (2.16). The assumption of ambipolar diffusion states that the flux of ions $\mathbf{j}_{ion}$ and electrons $\mathbf{j}_e$ is nearly the same and governed by the mobility μ and diffusion coefficient D:

$$\mathbf{j}_{ion} = N_{ion} e \tilde{\mathbf{E}} \mu_{ion} - D_{ion} \nabla N_{ion}.$$

$$\mathbf{j}_e = N_e e \tilde{\mathbf{E}} \mu_e - D_e \nabla N_e.$$

Under the assumption of ambipolar diffusion: $\mathbf{j}_{ion} = \mathbf{j}_e$, the vector of electrical field:

$$\tilde{\mathbf{E}} = \frac{1}{e} \frac{D_{ion} \nabla N_{ion} - D_e \nabla N_e}{N_{ion} \mu_{ion} + N_e \mu_e}.$$

If the plasma is electro-neutral, then $N_{ion} \approx N_e = N$ and

$$\tilde{\mathbf{E}} = \frac{1}{e} \frac{D_{ion} - D_e}{\mu_{ion} + \mu_e} \frac{\nabla N}{N}.$$

The mobility μ of charged particles is given by Einstein relation: $D_e = kT_e \mu_e$, and $D_{ion} =$

$kT_{ion}\mu_{ion}$. The final expression for the electric field is given as:

$$\tilde{\mathbf{E}} = \frac{k}{e}\frac{D_{ion} - D_e}{D_{ion}T_e + D_eT_{ion}}T_{ion}T_e\frac{\nabla N}{N}. \tag{2.18}$$

A more computationally efficient approach is proposed in Candler and MacCormack (1991) and based on the analysis of conservation of momentum for free electrons. Omitting the details, one can deduce that the electric field is approximately proportional to p_e of the gas of free electrons:

$$\tilde{\mathbf{E}} = -\frac{\nabla p_e}{N_e e}. \tag{2.19}$$

Substituting Eq. (2.19) into Eq. (2.16) one can obtain the following form of the equation of electron energy conservation:

$$\frac{\partial}{\partial t}\left(\rho e_e\right) + \frac{\partial}{\partial x^j}\left(u^j\left(\rho e_e + p_e\right)\right) = \frac{\partial}{\partial x^j}\left(v_e^j\left(\rho e_e + p_e\right)\right) + u_j\frac{\partial p_e}{\partial x^j} + Q_{eT}$$
$$-Q_{imp-ioniz} - Q_{imp-diss} + Q_{ass-ioniz} + Q_{ev}. \tag{2.20}$$

The model employed in a present work to assess the change of electron energy due to chemical reactions is discussed in Section 2.6.

2.5 Chemical kinetics

Chemical model plays an important role in the accurate description of composition of the high temperature gas. For the combustion problem, considered in present work, an appropriate set of reactions and reaction rates defines the physical behavior of hydrogen flame:

ignition delay, extinction parameters, flame thickness and composition. Chemical models of combustion in counter-flow jets include only neutral particles that are formed by reactions between hydrogen and oxygen (nitrogen does not participate in chemical reactions at these temperatures) and are valid in the narrow temperature range. For hydrogen flames the upper limit of temperature is nearly 3200 K as the typical temperature of hydrogen flame burning in the oxygen. The chemical model is not coupled to the equations for the thermodynamic state of the gas, since the latter is assumed to be in thermal equilibrium.

In hypersonics the chemical model has to include charged particles such as single-ionized atoms, molecules as well as electrons. There is no need to include ions with higher degree of ionization if temperature does not exceed 20000 K in the non-equilibrium flow (Surzhikov, 2011). For flows with shock the temperature changes from ambient to a few thousand degrees and the reaction rates are usually tailored to the entire temperature range observed in the shock layer. Another important feature of hypersonic chemical models is that the reaction rates are tightly coupled to the thermodynamic state of reactants. The rate of dissociation reactions should be reduced at non-equilibrium conditions when the vibrational mode is not fully excited and temperature of electrons significantly differs from the temperature of heavy reactants. The reactions involving electrons are likely to be governed by temperature of free electrons rather than heavy particles (Park, 1989).

The mass conservation of species given by Eq. (2.4) is rewritten for the mass fraction of species i:

$$\frac{\partial Y_i}{\partial t} + \rho u^j \frac{\partial Y_i}{\partial x^j} = \frac{\partial}{\partial x^j}\left(\rho_i v^j\right) + \dot{\omega}_i. \tag{2.21}$$

The law of mass action establishes the species production rate:

$$\dot{w}_i = M_i \sum_{j=1}^{N_J} (\nu''_{i,j} - \nu'_{i,j}) \left\{ k_{f,j} \prod_{k=1}^{N_{kf}} \left(\frac{\rho_k}{M_k} \right)^{\nu'_{k,j}} - k_{b,j} \prod_{k=1}^{N_{kb}} \left(\frac{\rho_k}{M_k} \right)^{\nu''_{k,j}} \right\}, \tag{2.22}$$

where $\nu''_{i,j}$ and $\nu'_{i,j}$ are the forward and backward stoichiometric coefficients of species i in reaction j, N_{kf} and N_{kb} are the number of species participating in the forward and backward reactions, respectively. The forward reaction rate $k_{f,k}$ is calculated based on the Arrhenius equation:

$$k_{f,k} = A_{f,k} T^{B_{f,k}} \exp\left(\frac{-E_{f,k}}{T} \right). \tag{2.23}$$

The backward reaction rate k_{b_k} can be calculated in two ways. In the work by Dunn and Kang (1973) the backward reaction rate is given by a similar Arrhenius equation:

$$k_{b,k} = A_{b,k} T^{B_{b,k}} \exp\left(\frac{-E_{b,k}}{T} \right). \tag{2.24}$$

However, another straightforward way to obtain backward reaction rate is by means of equilibrium constant:

$$k_{b,k} = k_{f,k} / K_{eq,k}. \tag{2.25}$$

The chemical model by Park for weakly ionized air plasma (Park, 1993) and GRI model for natural gas combustion (Smith et al., 1999) are adopted Eq. (2.25) to obtain $k_{b,k}$. The dependence of equilibrium constant on temperature is usually approximated by a polynomial expansion (Park, 1989).

2.6 Thermodynamics

At thermodynamical equilibrium conditions the population of energy levels is established by Boltzmann distribution at temperature T equal to the translational temperature T_{tr}:

$$N_i = \frac{N}{Z} g_i exp\left(-\frac{E_i}{kT}\right), \tag{2.26}$$

where N_i - population of energy level i, N is the total number of particles on all energy levels and Z is the partition function:

$$Z = \sum_{i=1}^{i=N_E} g_i exp\left(-\frac{E_i}{kT}\right),$$

N_E is the maximal number of energy levels and g_i corresponds to the degeneracy of energy level i, E_i - energy on level i. The thermal equilibrium between modes of energy (translational, rotational, vibrational and electronic) is reached by collisions between particles with different energies. At low temperatures or when the density of the flow is high the gas is assumed to be in thermal equilibrium and the population of all energy levels of all particles is described only by translational temperature. The flame in counter-flowing jets is assumed to be in thermal equilibrium and rotational and vibrational degrees of freedom are excited according to Eq. (2.26). However, in hypersonic flow the situation is more complicated.

In the shock layer the population of energy levels of atoms and molecules may vary from Boltzmann distribution. The time, necessary for equilibration of internal degrees of freedom with translational mode, is comparable with the characteristic time of the flow.

To model the non-equilibrium phenomena two major approaches are available: multi-temperature models (Gnoffo et al., 1989; Park, 1989) and radiative-collisional models (Bourdon and Bultel, 2007; Capitelli et al., 2007; Laux, 2002).

The essence of the multi-temperature approach is in the assumption that rotational, vibrational and electronic levels of particles are populated according to the Boltzmann distribution but with temperature, generally not equal to T_{tr}. Strictly speaking, if equilibrium is not present in the ensemble of particles no temperature definition can be introduced. In the light of this fact the multi-temperature models seems to be somewhat empirical. However the modern theory of multi-temperature models demonstrates satisfactory accuracy when applied to a flow with small deviation from Boltzmann equilibrium. The accuracy of these models suffers with the increasing velocity of re-entry and in the rarefied flows (Panesi, 2009).

It is assumed that the rotational and translational modes are in equilibrium: $T_{tr} = T_{rot}$. The population of vibrational levels depends on the characteristic frequency of molecular bond and, thus, is different for individual sorts of molecules. In present work three vibrational temperatures are considered: T_{v,N_2}, T_{v,O_2}, $T_{v,NO}$. The vibrational temperature of molecular ions is assumed to follow the vibrational temperature of corresponding neutral molecule (Josyula and Bailey, 2003). Additionally, the minor contribution of molecular ions to the energy balance should be taken into account. The electron-electronic temperature is governed by a separate energy equation, as it is shown later.

Vibrational-Translational relaxation

The relaxation of vibrational degree of freedom requires a greater number of collisions than the relaxation of rotational degree of freedom. An important mechanism of vibrational mode relaxation is the interaction with the translational mode. The fundamental result in the energy transfer between translational and vibrational modes was derived by Landau and Teller (1936). The rate of energy exchange $Q_{vT,i,m}$ is proportional to the difference between the vibrational energies evaluated at T and $T_{v,i,m}$:

$$Q_{vT,i,m} = \rho_{i,m} \frac{e_v\left(T\right) - e_v\left(T_{v,i,m}\right)}{\tau_{vT,i,m}}, \tag{2.27}$$

where $\rho_{i,m}$ is the density of particles with the vibrational mode m, $\tau_{vT,i,m}$ is the relaxation time of species i with mode m. For diatomic species the relation between i and m is unique and the mode index m is omitted for brevity. Landau-Teller model assumes that the rate of change of vibrational energy varies linearly with the difference $e_v\left(T\right) - e_v\left(T_{v,i,m}\right)$. According to this assumption, the vibrational excitation rate, coefficient K, changes with temperature as follows: $lnK \sim T^{-1/3}$. Several factors have to take place in order for Eq. (2.27) to be valid. First of all, Landau-Teller model considers harmonic oscillator. The spacing between levels of vibrational energy in the model of the harmonic oscillator is described by the following relation:

$$D\left(\nu\right) = \omega_e \left(\nu + \frac{1}{2}\right), \tag{2.28}$$

where ν is the vibrational quantum number. Then, only single quantum transitions are allowed: $\Delta\nu = \nu \pm 1$. The last assumption states that all vibrational levels have to follow Boltzmann distribution at the vibrational temperature.

Previously it was stated (Park, 1989) that at higher temperatures the equilibration of vibrational temperature is similar to the diffusion process and the vibrational relaxation is generally governed by the Fokker-Plank equation in a space of vibrational quantum ν (Park, 1989):

$$\frac{1}{N_x}\frac{\partial \rho_\nu}{\partial t} = \frac{\partial}{\partial \nu}\left(M\frac{\partial \rho_v}{\partial \nu}\right) + K\left(\nu, c\right)\left(\rho_a \rho_b - \rho_v\right), \tag{2.29}$$

where ρ, ρ_a and ρ_b are the number of density normalized with respect to their equilibrium value, M is the second order transition moment and $K\left(\nu, c\right)$ is the rate of vibrational excitation. Using Eq. (2.29) one may show that the Landau-Teller relaxation time relates to the time derived under assumption of Eq. (2.29) validity as follows:

$$\frac{\tau_D}{\tau_{L-T}} \approx \frac{4}{\pi}\frac{T_v}{T_{v,char}}\frac{T^2}{\left(T - T_v\right)^2} \tag{2.30}$$

The diffusion approximation for vibrational relaxation is valid for the entire relaxation zone except immediately behind the shock. To connect the Landau-Teller and diffusion formalism by Park the bridging model (Park, 1989) was suggested to modify the relaxation time in Eq. (2.27):

$$\frac{1}{\tau'_{vT}} = \frac{1}{\tau_{vT}}\left|\frac{T_{sh} - T_v}{T_{sh} - T_{sh,v}}\right|^s, \tag{2.31}$$

where T_{sh} and $T_{sh,v}$ are transnational and vibrational temperatures along the streamline where the initial excitation of the vibrational mode occurred and the exponent s is defined as

$s = 3.5exp\left(-5000/T_{sh}\right) - 1$. In case of one dimensional flow the application of Eq. (2.31) is straightforward, however in case of multidimensional flows it can be tricky. In Gnoffo et al. (1989) it is recommended to define characteristic temperature in the shock front for the entire flow.

The relaxation time in Eq. (2.27) is usually taken from the classical work by Millikan and White (1963):

$$p\tau'_{vT,i} = \sum_{i \neq j} n_j exp\left(A_{ij}\left(T^{-1/3} - 0.015\mu_{ij}^{1/4}\right) - B_{ij}\right) / \sum_{i \neq j} n_j, \tag{2.32}$$

where n_j is the number density of particles j. For temperature over 8000 K the Park's correction should be used (Park, 1984). This correction accounts for the non-adiabatic effects in the flow:

$$\tau_{park,i} = \frac{1}{\sigma_i v_i n_i}, \tag{2.33}$$

where v_i is the mean thermal velocity of molecules, $\sigma_i = \sigma'_i exp(50000/T)^2$. The resulting vT-relaxation time for species i is calculated as $\tau_{vT,i} = \tau'_{VT,i} + \tau_{park,i}$. It is worthwhile to note that Eq. (2.27) is acceptable if the information on rates of the vibrational relaxation is not available from other sources. For well studied molecules, such as nitrogen, oxygen, CO_2, the data on $\tau_{vT,i}$ is available by means of SSH theory (Sharma et al., 1988). This approach is generally more accurate and was previously used to compute the non-equilibrium vibrational relaxation in strong shock waves for air (Losev et al., 1995; Vlasov et al., 1997).

In present work the cross section σ' is chosen to be equal to 3x10^{-21} m^2 for N_2 and O_2 and 3x10^{-22} m^2 for NO, by recognizing that relaxation process involving NO is slower

Pair	A_{ij}	B_{ij}	Source
N_2 - N	180.	0.0262	(Park, 1993)
N_2 - O	72.4	0.015	(Park, 1993)
N_2 - N_2	221.	0.0290	(Park, 1993)
N_2 - O_2	245.	0.0305	(Park, 1993)
O_2 - N	72.4	0.015	(Park, 1993)
O_2 - O	47.7	0.059	(Park, 1993)
O_2 - N_2	134.	0.0295	(Park, 1993)
O_2 - NO	138.	0.03	(Park, 1993)
O_2 - O_2	136.	0.0298	(Park, 1993)
NO - NO	49.5	0.042	(Park, 1993)
NO - N, O	47.7	0.05	(Surzhikov, 2012)
NO - N_2, NO	198.	0.029	(Surzhikov, 2012)
NO - O_2	218.	0.0305	(Surzhikov, 2012)

Table 2.1: Parameters of vT-relaxation time

(Park, 1989). Parameters A_{ij} and B_{ij} in Eq. (2.32) are given in Table 2.1.

Vibrational-vibrational relaxation

The model proposed by Knab et al. (1995) is used to account for vibrational-vibrational energy transfer:

$$Q_{vv',i} = \sum_{j \neq i} N_A \sigma_{i,j} P_{i,j} \sqrt{\frac{8RT}{\pi \mu_{i,j}}} \frac{\rho_j}{M_j} \rho_i \left(e_{v,i}(T) \frac{e_{v,j}(T_{v,j})}{e_{v,j}(T)} - e_{v,i}(T_{v,i}) \right), \tag{2.34}$$

where $\mu_{i,j}$ is the reduced mass of i and j oscillators. Probability $P_{i,j}$ is recommended to chose a value equal to 10^{-2} (Candler and MacCormack, 1991). Due to the relatively insignificant difference of vibrational temperature of molecules in air, the vibrational-vibrational relaxation mechanism is expected to play a secondary role in vibrational energy

exchange.

Relaxation of free electrons

Because of significantly lower mass, the energy carried by free electrons in the ionized plasma is considered separately. Interaction with heavy particles Q_{Te}, the energy exchange between free electrons and vibrational mode and the change of thermal energy due to the chemical reactions govern the electron temperature.

Sink or source of free electrons in air plasma is due to the reactions of associative ionization, Eq. (2.35), (2.36), (2.37), electron impact ionization, (2.38), (2.39) and radiative recombination (2.41), (2.40):

$$N + O \rightarrow NO^+ + e^-, \tag{2.35}$$

$$N + N \rightarrow N_2^+ + e^-, \tag{2.36}$$

$$O + O \rightarrow O_2^+ + e^-, \tag{2.37}$$

$$O + e^- \rightarrow O^+ + 2e^-, \tag{2.38}$$

$$N + e^- \rightarrow N^+ + 2e^-, \tag{2.39}$$

$$O^+ + e^- \rightarrow O + h\nu, \tag{2.40}$$

$$N^+ + e^- \rightarrow N + h\nu. \tag{2.41}$$

Immediately behind the shock front the concentration of free electrons is vanishing and the associative ionization is responsible for the source of free electrons. The exponential factor, often interpreted as an activation energy for the reaction (2.35) is postulated for

E_{act} = 31900 K according to Park (1993), while for reactions (2.36) and (2.37) it is 67500 K and 80600 K, respectively. One may conclude that the associative ionization reaction (2.35) is dominant for the primary generation of free electrons.

Energy transformation of free electrons due to associative ionization is given by following expression:

$$Q_{ass-ion} = C_v \sum_{k \in \Omega_{ass-ion}} \left(\alpha_{ass-ion} k_{k,f} X_A X_B T - \beta_{ass-ion} k_{k,r} X_{AB+} X_e T_e \right), \qquad (2.42)$$

where $\Omega_{ass-ion}$ stands for the array of reactions of associative ionization and coefficients $\alpha_{ass-ion}$ and $\beta_{ass-ion}$ are intended to describe the efficiency of energy transformation. The sensitivity study of these parameters is provided earlier in the work by Surzhikov et al. (2006). In present work it is assumed that $\alpha_{ass-ion}$ and $\beta_{ass-ion}$ are equal to unity due to the large uncertainty of the model. Energy balance in reactions of electron impact ionization is accounted in the next way:

$$Q_{imp-ioniz} = \sum_{k \in \Omega_{ion}} k_{k,f} X_i X_e E_{ion,i}, \qquad (2.43)$$

where $E_{ion,i}$ is the ionization energy of molecule i from the ground level. Change in the electron energy is also possible in the reaction of electron impact dissociation:

$$N_2 + e^- \rightarrow 2N + e^-, \qquad (2.44)$$

however, due to the high activation energy, this reaction is relatively unimportant in flows generated by re-entry velocities below 10 km/s (Josyula and Bailey, 2003). Nevertheless,

in present work the energy balance of reaction, Eq. (2.44) is accounted for as follows:

$$Q_{imp-diss} = \sum_{k \in \Omega_{diss}} k_{k,f} X_i X_e E_{diss,i}, \tag{2.45}$$

where $E_{diss,i}$ is the dissociation energy of N_2.

Energy transfer $Q_{eT,i}$ due to the elastic collisions of free electrons with heavy particles is usually described by the following expression (Appleton and Bray, 1964):

$$Q_{eT,i} = \frac{3}{2} n_e k_B \left(T - T_e\right) \frac{1}{\tau_{eT,i}\left(T_e\right)}, \tag{2.46}$$

where n_e is the electron number density, k_B is the Boltzmann constant. Parameter $\tau_{eT,i}$ is the relaxation time of electron - heavy particle i:

$$\tau_{eT,i} = \sum_{i \neq e} \frac{m_e}{m_i} \nu_{i,e},$$

where $\nu_{i,e} = 8 v_e n_i \Omega_{i,e}^{(1,1)}/3$. Collision frequency can be calculated with data provided in Vanden Abeele (2000).

A model of electron-vibrational relaxation has been proposed by Chernyi et al. (2002):

$$Q_{ev} = 2 \cdot 10^{-17} \sum_{i \in \Omega_v} n_e n_i \omega_{ev,i} P_{1,0,i} \left[\frac{exp\left(-1.44 \omega_{ev,i}/T_e\right)}{\left[1 - exp\left(-1.44 \omega_{ev,i}/T_e\right)\right]^2} - \frac{exp\left(-1.44 \omega_{ev,i}/T_{v,i}\right)}{\left[1 - exp\left(-1.44 \omega_{ev,i}/T_{v,i}\right)\right]^2} \right], \tag{2.47}$$

where Q_{ev} is the rate of energy exchange and is measured in $J/m^3/s$, $P_{1,0,V}$ is the proba-

bility of the excitation of ground level due to the electron impact:

$$P_{1,0,V} = 0.45 \cdot 10^{-10} exp\left(-\frac{10000}{T_e}\right). \tag{2.48}$$

Besides the model of Chernyi, a similar formula to Landau-Teller model is proposed by Lee (1984):

$$Q_{ev,i} = \rho_i \frac{e_{v,i}\left(T_{v,i}\right) - e_{v,i}\left(T_e\right)}{\tau_{ev,i}}, \tag{2.49}$$

where i is molecular species index. Although besides nitrogen other types of neutral molecules and molecular ions are present in the relaxation zone, only the interaction with molecular nitrogen is significant in ev-relaxation. Other channels are relatively unimportant due to small concentrations of molecular species after dissociation and small cross section of interaction (Park, 1989).

The analytical estimation of $\tau_{ev,i}$ is provided in Lee (1984). However it is shown in work by Bourdon and Vervisch (1997) that the relaxation rates by Lee is overestimated by the factor of 2-3. The relaxation times, derived in Bourdon and Vervisch (1997) are curved fitted for the electron temperature in the range of $3000 < T_e < 20000$ K as follows:

$$log_{10}\left(p_e \tau_{ev}\right) = A\, log_{10}\left(T_e\right)^2 + B\, log_{10}\left(T_e\right) + C \tag{2.50}$$

where τ_{ev} measured in s, p_e measured in atm, the curve fit parameters are given in Table 2.2:

T_e, K	A	B	C
3000-7000	5.019	238.625	64.219
7000-20000	2.448	218.704	25.635

Table 2.2: Curve fit parameters of ev-relaxation time

2.7 Transport properties

At low temperatures (T $<$ 3000 K) the molecular viscosity can be estimated from the well know Sutherland's law:

$$\mu = \mu_0 \frac{T_0 + C}{T + C} \left(\frac{T}{T_0} \right)^{3/2}.$$

The diffusion coefficient of gas can be calculated by means of Schmidt number Sc $= \mu/\rho D$, which is in the range of 0.9 - 1 for gases of interest. The heat conductivity is then calculated by using Prandtl number Pr = $c_p \mu/\lambda$, which is approximately 0.72 for the air at standard conditions.

However, at high temperatures the transport properties of gases significantly differ from those that are obtained by assuming constant Sc and Pr numbers. The accurate approach to obtain transport properties of gas valid for a wide temperature range is established by the kinetic theory. The solution of Boltzmann equation for gas accounting for collision between particles has to be performed.

One of the methods is the linearizion of governing equation by using an expansion according to the small parameter. This approach is used by Chapman-Enskog approximation. The Knudsen number serves as a small parameter in this case. By using this approach the Boltzmann transport equation can be transformed into a system of linear equations (Bird

and Stewart, 2007; Ferziger et al., 1973; Vincenti and Kruger, 1965). The approximated solution of linearized Boltzmann equation for velocity distribution function can be written in the form of truncated Sonine polynomials and the accuracy is defined by the number of the retained terms.

The transport properties for gas mixture can be obtained in many ways. The most effective approach is the approximate mixture rules that allow to obtain the effective transport properties of gas mixture at specific composition. Another approach is to use the iterative methods that are shown to be more accurate for gases when dissociation and ionization are present (Magin, 2004). There is also a direct way to calculate transport of species by accounting for the diffusion process between each sort of particles using Stefan-Maxwell relations:

$$\nabla X_i = \sum_{j=1}^{N_c} \frac{X_i X_j}{D_{ij}} \left(\mathbf{v}_j - \mathbf{v}_i \right), \tag{2.51}$$

where X is the molar fraction, D_{ij} is the binary diffusion coefficient, $\mathbf{v}_i$ is the diffusion velocity of species i and N_c is the number of all species.

Equation (2.51) can be obtained retaining one term in the Sonine polynomial expansion (Coffee and Heimerl, 1981). It is worthwhile to note that the thermal diffusion in Stefan-Maxwell equation is essentially zero. Besides, it is computationally demanding and may lead to some computational difficulties (Smooke, 2013).

Another method is proposed by Curtiss and Hirschfelder (1949). It is assumed that all species except i-th component are moving with the same diffusion velocity $\mathbf{v}$. This gives

the next relation for the diffusion velocity of i-th component:

$$\mathbf{v}_i = \frac{(1 - Y_i)}{X_i \sum_{j \neq i}^{N_c} X_j / D_{ij}} \nabla X_i. \tag{2.52}$$

In case of a binary mixture Eq. (2.52) is transformed to the Fick's law and the effective diffusion coefficient D_{im} can be introduced to generalize the results on multicomponent mixture:

$$Y_i \mathbf{v}_i = -D_{im} \nabla Y_i, \tag{2.53}$$

where

$$D_{im} = \frac{1 - X_i}{\sum_{j \neq i}^{N_c} X_j / D_{ij}}. \tag{2.54}$$

One may introduce the constraint on the net diffusion velocity:

$$\sum_{i=1}^{N} Y_i \mathbf{v}_i = 0. \tag{2.55}$$

Both simplifications by Curtis and Hirshfelder, Eq. (2.52) and Fick's law, Eq. (2.53) do not satisfy the constraint (2.55). An efficient and relatively simple way to satisfy Eq. (2.55) is to introduce the correction velocity (Oran and Boris, 1980), which does not depend on the composition but is spatially varying:

$$\sum_{i=1}^{N_c} Y_i \left(\mathbf{v}_i + \mathbf{v}_{corr} \right) = 0, \tag{2.56}$$

which results to the expression:

$$\mathbf{v}_{corr} = -\sum_{i=1}^{N_c} Y_i \mathbf{v}_i. \tag{2.57}$$

Calculation of the binary diffusion coefficient in Eq. (2.52) and (2.54) can be done through the binary collision integral $\overline{\Omega}_{ij}^{(1,1)}$:

$$D_{ij} = \frac{3}{8} \frac{\sqrt{\pi m_{ij} kT}}{p\pi\sigma_{ij}^2 \overline{\Omega}_{ij}^{(1,1)}}, \tag{2.58}$$

The temperature dependence of the collisional integral is usually approximated by the polynomial expansion (Anfimov et al., 1981; Gupta et al., 1990) or a more complex expression (Capitelli et al., 2000). The calculation of thermal conductivity can be performed on a different level of approximation in a similar manner to the diffusion coefficient. The three terms of Sonine polynomials expansion are also available to compute conductivity in the accurate manner, however it is computationally prohibitive (Coffee and Heimerl, 1981). Expression by Mason and Saxena (1958) is used in the present work:

$$\lambda = \sum_{i}^{N_c} \frac{\lambda_i}{\sum_{j\neq i}^{j=N_c} \Phi_{ij} X_j / X_i}, \tag{2.59}$$

where

$$\Phi_{i,j} = \left[1 + \left(\frac{\mu_i}{\mu_j}\right)^{1/2} \left(\frac{M_i}{M_j}\right)^{1/4}\right]^2 \left[8\left(1 + \frac{M_i}{M_j}\right)\right]^{-1/2}. \tag{2.60}$$

where μ_i and M_i are the viscosity and molar mass of species i. Another empirical equation to estimate conductivity of gas mixture has been proposed in Burgoyne and Weinberg

(1953):

$$\lambda = \frac{1}{2}\left(\sum_{i=1}^{N_c} X_i\lambda_i + \sum_{i=1}^{N_c}\frac{X_i}{\lambda_i}\right). \tag{2.61}$$

The thermal conductivity of individual species in Eq. (2.61) can be calculated using the second binary collision integral $\overline{\Omega}_{ij}^{(2,2)}$:

$$\lambda_i = \frac{75}{64}\frac{k\sqrt{\pi kT/m_i}}{\pi\sigma_i^2\overline{\Omega}_{ij}^{(2,2)}},. \tag{2.62}$$

where k is the Boltzmann constant and m_i is the mass of particle of species i and σ_i is the Lennard-Jones collision cross section. Viscosity of the gas mixture is calculated by the following expression:

$$\mu = \sum_{i=1}^{N_c}\frac{X_i\mu_i}{\sum_{j\neq i}^{N_c} X_j\Phi_{i,j}}, \tag{2.63}$$

where $\Phi_{i,j}$ is given by Eq. (2.64) and single species viscosity is defined by Eq. (2.65).

$$\Phi_{i,j} = \frac{1}{\sqrt{8}}\left(1+\frac{M_i}{M_j}\right)^{-1/2}\left[1+\left(\frac{\mu_i}{\mu_j}\right)^{1/2}\left(\frac{M_i}{M_j}\right)^{1/4}\right]^2, \tag{2.64}$$

$$\mu_i = \frac{5}{16}\frac{\sqrt{\pi m_i kT}}{\pi\sigma_i^2\overline{\Omega}_{ii}^{(2,2)}}. \tag{2.65}$$

2.8 Boundary conditions

Setting up boundary conditions for the problem related to the fluid motion defines the structure of the flow in the entire computational domain. The choice of boundary conditions has to be made along with the analysis of the eigenvalues of the governing system of equations.

The conditions at the boundary domain are defined by the type of equations to be solved. Both steady and unsteady supersonic flows are described by the hyperbolic system of equations. The number of boundary conditions are determined by the analysis of characteristics directed to the boundary from the exterior domain. The steady subsonic flow is described by the elliptic system of equations. For this type of flow the boundary conditions are also defined by the sign carried by characteristics and usually results into a set of dependent variables.

For the subsonic flow on the incoming boundary three characteristics carry positive sign and only one has a negative slope; this means that all variables but one have to be specified on the inlet boundary. Pressure and temperature are the physical quantities that can be controlled when flow goes through the incoming boundary. In present work the total pressure and temperature of the flow are specified at the inlet boundary:

$$T_{total} = T_{ini}\left(1 + (\gamma - 1)\, M^2/2\right), \tag{2.66}$$

$$P_{total} = P_{ini}/(T_{ini}/T_{total})^{(\gamma/\gamma-1)} \tag{2.67}$$

where initial temperature T_{ini} is equal to 295 K, initial pressure P_{ini} is equal to 100,135 Pa and specific heat ratio γ is equal to 1.4. To derive the boundary condition for the velocity, the characteristic equation on the inlet boundary is considered. When the tangential component of velocity is neglected, the characteristic equation in the normal direction to the inlet boundary takes the appearance as:

$$\frac{\partial p}{\partial t} - \rho c \frac{\partial u}{\partial t} = -\left(u - c\right)\left(\left(\mathbf{n} \cdot \vec{\nabla} p\right) - \rho c \left(\mathbf{n} \cdot \vec{\nabla} u\right)\right) \tag{2.68}$$

Assuming that only the steady state solution is of interest, time derivative can be omitted. Since the flow in present study is nearly incompressible, the spatial derivative of pressure can be also neglected. After these simplifications, the boundary condition for the axial component of velocity takes the appearance as:

$$\mathbf{n} \cdot \vec{\nabla} u = 0. \tag{2.69}$$

The derived BC for velocity can be easily implemented in numerical procedure but should be used with precautions. This BC does not satisfy the equation of characteristic for the transient flow and has to be appropriately modified when pressure changes significantly. The radial component of the inlet velocity is set to zero.

No-change boundary condition, Eq. (2.69), does not allow to control the inlet velocity explicitly. However, having control over the inlet velocity is the convenient tool of verification against available data. Following this idea, the equation of characteristic wave propagation can be introduced in the form

$$\frac{\partial R_{\pm}}{\partial t} + (u \pm c) \frac{\partial R_{\pm}}{\partial x} = 0 \tag{2.70}$$

where R is the Riemann invariant (RI) (Dafermos, 2005):

$$R_{\pm} = u \pm \frac{2c}{\gamma - 1}. \tag{2.71}$$

Different signs of the invariant in Eq. (2.71) correspond to two opposite directions of characteristic waves. Implementation of RI allows explicit control over the inlet velocity.

Introducing the farfield RI and extrapolated RI as:

$$R_\infty = u_\infty - \frac{2c_\infty}{\gamma - 1},$$

$$R_e = u_e - \frac{2c_e}{\gamma - 1},$$

which correspond to the incoming and outgoing characteristic waves, subtraction and adding of these invariants give the flow velocity and the speed of sound at the inlet boundary:

$$u = \frac{1}{2}\left(R_\infty + R_e\right)$$

$$c = \frac{\gamma - 1}{4}\left(R_\infty + R_e.\right)$$

Typically the farfield invariant is calculated using incoming parameters of the flow, while extrapolated invariant is calculated using values from the grid next to boundary. In present study the farfield invariant is calculated using given inlet speed of the flow $U_\infty = U_{ini}$, and corresponding speed of sound $c_\infty = \sqrt{\gamma R T_{ini}}$. Temperature on the inlet boundary comes from the equation for the speed of sound: $T = c^2/\left(\gamma R\right)$. Density and pressure on the inlet boundary are calculated from the relation $\rho^\gamma/p = const$ and the ideal gas equation of state.

For the supersonic flow all characteristics carry positive sign and information about the flow has to be entirely specified on the inlet boundary. The outflow boundary requires a bit more of attention. Since all characteristics carry positive sign, the acoustic characteristic does not propagate upstream. The usual approach is to set no-change condition for all dependent variables. A more complicated situation takes place when the flow is subsonic

at the outflow boundary. Only one variable can be specified, while other variables have to be approximated. An ideal boundary condition on the outflow boundary will let the characteristics to leave the computational domain without reflecting back to the interior (Keller and Givoli, 1989; Rudy and Strikwerda, 1980; Yee, 1981).

One of the variables that can be controlled at the outflow boundary is the gas pressure. At the same time it is shown (Oliger and Sundström, 1978) that the simple boundary condition

$$p = p_{out} \tag{2.72}$$

is mathematically well posed, although it does not completely eliminate the reflections from the outflow boundary. However when the outer boundary is located sufficiently far away, the influence of the reflections on the subsonic flame can be minimized. This approach is applied in the present study. Other primitive variables (**u**, ρ, T) are obtained with the zero order approximation. No higher order approximation is introduced to avoid typical "saw-tooth" behavior of solution.

2.9 Radiation

The radiation emitted by atoms and molecules exited by the compression shock wave is important for engineering design of the thermal protection system of hypersonic vehicles and spacecrafts (Andrienko et al., 2013). At the same time it is clear that the effect of radiative cooling can be a significant term in the overall balance of energy (Palmer et al., 2011). Another important process is known as the precursor radiation (Hammerling, 1960) which occurs when the emission from the relaxation zone is so strong that it can ionize the

gas ahead of the shock wave. This happens due to the fact that the radiation propagates with the speed of light rather than the flow speed.

For the re-entry problem the radiation component of the flux becomes detectable when the spacecraft enters the atmosphere with a speed of more than 7 km/s. A significant effort has been invested in the direction of an accurate radiative heating prediction for the atmospheric entry problem. The radiation phenomenon occurs at the speed of light rather than the sonic speed for aerodynamic phenomena. Therefore, the most convenient approach to address the additional energy exchange process is by integrating the radiative heat transfer as a heat source or sink into the global energy conservation law (Shang and Surzhikov, 2012; Siegel and Howell, 2002). While the problems of radiation-gasdynamic interaction and precursor ionization are studied less often, the main effort is spent to develop efficient optical and spatial models of radiation transfer to predict the radiation flux.

The radiation transport equation at local thermodynamic equilibrium in nonscattering media satisfying the law of detailed balance can be expressed as a partial differential equation in space and time (Mihalas and Mihalas, 1999; Siegel and Howell, 2002; Surzhikov, 2002):

$$\frac{1}{c}\frac{\partial J_\nu(\vec{s},\Omega,t)}{\partial t}+\frac{\partial J_\nu(\vec{s},\Omega,t)}{\partial s}+\kappa_\nu\left(s\right)J_\nu(\vec{s},\Omega,t)=\kappa_\nu\left(s\right)J_{b,\nu}\left(T\left(s\right)\right) \tag{2.73}$$

The scattering terms can be neglected in RTE because of the relative low scattering at the temperature of interest. The dependent variable $J_\nu(\vec{s},\Omega,t)$ is the spectral intensity of radiation at the location s along the direction given by Ω, as shown in Fig. 2.2. The symbol κ denotes the volumetric spectral absorption coefficient of radiation. The transient term in

Eq. (2.73) is usually neglected, and RTE becomes:

$$\frac{\partial J_\nu(\vec{s},\Omega)}{\partial s} + \kappa_\nu\left(s\right) J_\nu(\vec{s},\Omega) = \kappa_\nu\left(\vec{s}\right) J_{b,\nu}\left(T\left(\vec{s}\right)\right) \tag{2.74}$$

The absorption coefficient κ is to be obtained from the local gas properties. In general, the optical data generation process is built upon the ab initio application of quantum mechanics and/or physical-based approximation from the molecular and atomic spectral structures. However, the most commonly accepted data bases under the local thermodynamic equilibrium (LTE) approximation have been provided by NASA (Whiting et al., 1996), NIST (Ralchenko et al., 2010), and by Russian Academy of Sciences (Surzhikov, 2000, 2006). These optical data bases are adopted for the present simulation. In present work optical properties are calculated using program code ASTEROID by Prof. Surzhikov.

There is a very large group of numerical models for solving the RTE equation (2.74). The angular dependence of spectral radiation intensity is often approximated as a polynomial expansion by the spherical harmonic method or half-moment method. The more recent ray tracing method (see, for example, Siegel and Howell (2002)) performs direct angular integration of radiation intensity, thus it is more accurate. At the same time, the accounting for the spectral dependence of radiation intensity is usually given by multi-group approach. It is a convenient engineering technique to divide the entire spectral domain into multiple groups and average the optical properties within each of them. The numerical accuracy can be improved by increasing number of the spectral groups. However, this approach is not always necessarily more accurate to simulate a medium of varying opacity. On the other hand, the Monte-Carlo method, ray tracing and view-factor methods are more

appealing because of their intrinsic computational procedure which closely represents the physical process of propagation of the radiation quanta in the participating media.

The coupling of the thermodynamic state to the optical properties of any gaseous medium is unique for the fundamental bound-bound, bound-free, and free-free quantum transition processes (Surzhikov, 2002; Zeldovich et al., 1985). Generally speaking, the aerothermodynamic conservation equations of a flow field must be solved iteratively in conjunction with the radiative energy transfer equation. This coupling appears in the radiative heat generation term in the right hand side of energy Eq. (2.11). However, at low entry velocities this coupling is unnecessary. The relevant Goulard number (Goulard, 1961) is calculated as:

$$\Gamma = \frac{2q_{rad}}{\frac{1}{2}\rho v_{\infty}^{3}}$$

and provides a qualitative assessment on the importance of the coupling of radiation transfer equation with the flow field governing equations. Typically, the coupling becomes necessary when Γ is greater than 10^{-2}. For the orbital re-entry, considered in the present study (Grantham, 1970) Γ is of the order of 10^{-4}, and the RTE can be solved only once after solution of gasdynamic system of equations is obtained.

Tangent slab approximation

The radius of curvature of the re-entry body can be significant compared to the characteristic size of the vehicle, as it was in mission of Apollo and FIRE II. In these cases, the radiation transfer equation can be reduced to a one-dimensional problem along the normal vector emitted from the surface. If the optical and thermodynamic properties vary only

along a chosen direction, the solution of radiation transfer equation can be obtained in terms of integral-exponential functions (Chandrasekhar, 1960). In case of non-scattering media and in the absence of incoming radiation the radiation energy density and radiation flux density are determined by Eq. (2.75) and (2.76):

$$U(\tau) = \frac{2\pi}{c} \int_{\tau'=0}^{\tau'=\tau} J_b(\tau') E_1(\tau - \tau') d\tau' + \frac{2\pi}{c} \int_{\tau'=\tau}^{\tau'=\tau_H} J_b(\tau') E_1(\tau' - \tau) d\tau', \quad (2.75)$$

$$W(\tau) = 2\pi \int_{\tau'=0}^{\tau'=\tau} J_b(\tau') E_2(\tau - \tau') d\tau' + 2\pi \int_{\tau'=\tau}^{\tau'=\tau_H} J_b(\tau') E_2(\tau' - \tau) d\tau', \quad (2.76)$$

where J_b is the radiation intensity of black body, τ and τ_H correspond to the current and total optical thickness of flat layer, E_1 and E_2 are integro-exponential functions of first and second order:

$$E_n(x) = \int_0^1 exp(-x/\mu) \mu^{n-2} d\mu. \quad (2.77)$$

The direct calculation of Eq. (2.77) is computationally prohibitive if performed at every grid point, specially in case of $x \ll 1$, i.e. in optically thin gas. The tables of integro-exponential functions are usually used to avoid repetitive calculations.

The tangent slab (TS) approximation is a relatively simple method to obtain radiative flux density distribution by approximating the radiating media as an infinite slab (Chandrasekhar, 1960). It was shown (Whiting et al., 1996; Wright et al., 2005) that TS can be applied with a good accuracy only for the front shield of the space vehicle body, where the bow shock can be approximated as a flat layer. The computational cost of the tangent slab approximation is relatively low. It is worthwhile to notice that besides the flux component at the surface of the vehicle, the TS approximation can be used to calculate the density of

the radiation energy. Thus, the TS approximation can be efficiently used to account for the strong interaction of radiation with the flow field. The disadvantage of the TS method is its inaccuracy: the implementation of a correction factor is needed because of the curvature of the bow shock and the body surface. The emission coming from the shock layer is different from the infinite slab with the same distribution of parameters. The radiative heating rate appears to be very sensitive to the radius of curvature and requires a separate study for each new geometry.

$\mathbf{P}_1$ approximation

One of the most popular and relative simple methods to implement the multi-dimensional model of radiation transfer is the spherical harmonics method (SHM). The main idea of the SHM is approximation of the radiation intensity by the number of Legendre polynomials in spherical coordinates with weight, dependent only on the spatial coordinates, as it is given by Eq. (2.78):

$$J = \sum_{l=0}^{\infty} \frac{1}{2} \alpha_{l,0} P_l(\mu) + \sum_{m=1}^{l} P_l^m(\mu) \left(\alpha_{l,m} cos(m\varphi) + \beta_{l,m} sin(m\varphi) \right), \tag{2.78}$$

where $\mu = cos\theta$, ϕ is the angle of spherical coordinates, P_l^m is the associated Legendre polynomial, α, β are the coefficients to be determined.

The spherical harmonics method was proposed in the work by Jeans (1917). The further development of the SHM was suggested by Chandrasekhar (1960); Davison and Sykes (1957). One of the distinct advantages of the SHM is its straightforward and efficient application in complex and multi-dimensional domains as well as on grids of different

topologies (Andrienko and Surzhikov, 2012; Andrienko et al., 2013). The most simple realization of SHM is called as the P_1-approximation (or the P_1 method), where only two terms in Eq. (2.78) are retained. The P_1-approximation presents radiation intensity as the sum of two spherical functions:

$$J = \frac{c}{4\pi}U + \frac{3}{4\pi}W cos\theta, \tag{2.79}$$

Using the expansion (2.79), the radiation transfer equation is transformed to the elliptic equation in terms of radiation energy under conditions of local thermodynamic equilibrium:

$$\nabla\left(\frac{c}{3\kappa}U_\nu\left(s\right)\right) + \kappa c U_\nu\left(s\right) = 4\pi\kappa J_b, \nu\left(s\right). \tag{2.80}$$

The disadvantages of the P_1 method are well known and discussed in literature (Chandrasekhar, 1960; Davison and Sykes, 1957; Surzhikov, 2009). The P_1-approximation may be inaccurate in the vicinity of boundaries of the computational domain, in optically thin media and when strong gradient occurs (Dombrovsky, 1996). On the other hand, the high efficiency of the P_1 method allows application in case of strong radiation-flowfield interaction. The P_1-approximation can be used also for the surface flux density calculation in the case of strong ablation of the SV capsule, when ablation products can significantly change the optical properties of the flow around the capsule.

Ray tracing method

The solution of RTE, Eq. (2.74), along the selected direction Ω is given by:

$$J_\nu(\tau) = J_\nu^+(\tau_0)e^{-\tau} + \int_{\tau_0}^{\tau} \kappa_\nu(\tau')J_{b,\nu}(\tau')e^{-(\tau-\tau')}d\tau', \tag{2.81}$$

where J_ν^+ is the spectral intensity of the incoming radiation. Then, the vector of the spectral radiation flux density is calculated as:

$$W_\nu(\vec{s}) = \int_0^{2\pi} J_\nu(\Omega, \vec{s})\Omega d\Omega, \tag{2.82}$$

where the infinitesimal increment of solid angle $\partial\Omega$ of the above equation is defined by the azimuthal and latitude angles, $d\varphi$ and $d\theta$ as shown in Fig. 2.2.

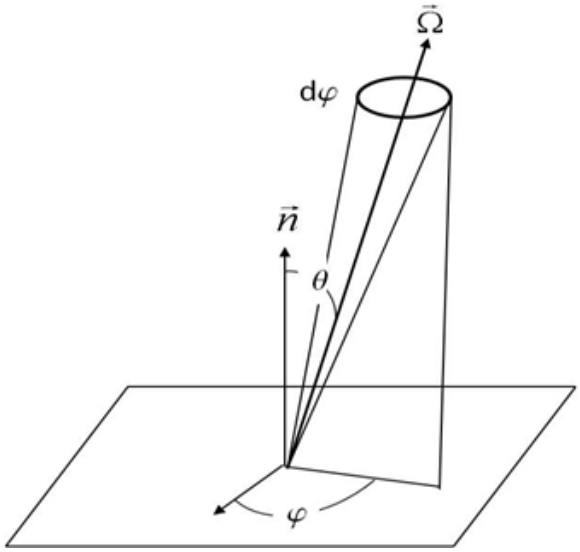

Fig. 2.2: Solid angle of integration by ray tracing method

The volumetric density of radiation energy is calculated as:

$$U_\nu(\vec{s}) = \frac{1}{c}\int_0^{4\pi} J_\nu(\Omega, \vec{s}) d\Omega, \tag{2.83}$$

The ray tracing method models the radiation quanta propagation by emitting a group of rays from a designated point in a discretizing solid angle. The radiation flux density on the surface of the body is obtained by integrating the radiative spectral intensity over half of the entire solid angle and over all spectra, if the integral characteristic of radiation field is required. When the RTM is applied to obtain the density of radiation energy, emitted rays should discretize the entire solid angle. Typically several hundred surface points on an axisymmetric configuration are calculated for a single earth re-entry simulation (Liu et al., 2010; Shang and Surzhikov, 2012; Surzhikov and Shang, 2011), and an order of 10^2 points along each tracing ray is distributed. For accurate angular integration of radiation intensity emitted from the shock wave the number of rays should be nearly 50 to 100 in each direction, leading to a 50^2 - 100^2 of a total, if the flux density is desired, and twice more if the density of radiation energy is calculated. Integration over the spectral variable involves at least 10^2-10^3 points of integration, if the multi-group approach is applied. The line-by-line calculations are not available by ray tracing method in the current formulation because of computational limitations and the specifics of radiation transfer in atomic lines (Surzhikov, 2004b). One may conclude that the RTM is a costly approach.

In the conventional ray tracing approach, a group of tracing ray is designated by its solid angle $\Omega_{m,n}$. The spectral flux density is often obtained by a simple first-order angular

integration:

$$W_\nu(\vec{s}) = \int_0^\infty d\nu \int_0^{2\pi} d\varphi \int_0^{\pi/2} J_\nu(\vec{s},\Omega)\cos\theta\sin\theta d\theta = \tag{2.84}$$
$$= \int_0^\infty d\nu \sum_{m=1}^{M-1}(\varphi_{m+1}-\varphi_m)\sum_{n=1}^{N-1} J_\nu(\Omega_{m,n})[\sin\theta_{n+1}\cos\theta_{n+1} - \sin\theta_n\cos\theta_n](\theta_{n+1}-\theta_n)$$

A high-resolution integration over the solid angle in a uniformly angular displacement space can be obtained by the product sum with a weight function. In fact the three-point Simpsons rule or any other high order integration method can generate a more accurate result than the above first-order approximation and for three point Simpson's rule can be given as follows:

$$W_\nu(\vec{s}) = \int_{2\pi} J_\nu(\vec{s},\Omega)\Omega d\Omega =$$
$$\sum_{n=1}^{N-2}(\Omega_{n+2}-\Omega_n)\left[J_\nu(\vec{s},\Omega_n)\Omega_n + 4J_\nu(\vec{s},\Omega_{n+1})\Omega_{n+1} + J_v(\vec{s},\Omega_{n+2})\Omega_{n+2}\right]/6 \tag{2.85}$$

There are also known formulations for even higher order Simpsons rule (Carnahan et al., 1969), however one needs to break down the finite number of the discrete data into groups of three-point or more segments and perform an algebraic sum. This integrating rule also has restrictions for an even number of intervals or an odd number of base points over a constant incremental value $\Delta\Omega$.

As the radiating beam propagates through an inhomogeneous optical path, the spectral intensity needs to take into account the opaque effect along the beam path of the photon motion. In general, it is accomplished by means of Buger-Lamber-Bear law, reflected in the exponential term in Eq. (2.81). For radiation intesity, contributed by direction $\Omega_{m,n}$ the

Eq. (2.81) takes the following appearance (no incoming radiation is assumed):

$$J_\nu(\Omega_{m,n}) = \int_{r_0}^{r} J_{b,\nu}(\Omega_{m,n}, r)\kappa_\nu(r) \exp\left[-\int_0^s \kappa_\nu(s')ds'\right] dr \tag{2.86}$$

In the above equation, r_0 and r are the beginning and ending locations along the ray. Substituting Eq. (2.86) into (2.9) the final form of the radiative flux density can be obtained. In practice, the local radiation spectral intensity $J_{b,\nu}(r)$ and the absorption coefficient $\kappa_\nu(r)$ has been approximated by the averaged values between the start and the end points of a tracing ray. In the work by Surzhikov (2002) an additional simplification was recommended by integrating in the following way,

$$J_\nu(\Omega_{m,n}) = \sum_{k=1}^{k-1} J_{b,\nu,k+1/2}(\Omega_{m,n}, \tau)(\tau_{k+1} - \tau_k) \tag{2.87}$$

In the above equation, the radiation spectral intensity $J_{b,\nu,k+1/2}$ is obtained by averaging temperature along the tracing ray between the positions of τ_k and τ_{k+1}. This simple approximation is essentially the trapezoidal rule and is fully compatible with the mean-value theorem.

One of the crucial drawback of RTM is its inefficiency. The necessity of performing numerical integration as per Eq. (2.86) and angular integration, Eq. (2.9) is computationally prohibitive. Meanwhile for engineering design it is required to obtain integral over the spectrum heating rate. The typical spectral model contains several hundred sub-groups, and the calculation of Eq. (2.86) and (2.9) has to be repeated an appropriate number of times. This makes ray tracing method applicable only at a point, i.e. to calculate only the

flux density. Theoretically the RTM can be applied to obtain radiation energy, however no attempt has been made.

The cost of the RTM consists of three factors: an effort, required to approximate the properties of gas from the grid conformed to the surface of space vehicle on the grid of the tracing ray, solution of Eq. (2.86) and optical properties calculation. While the last factor is dependent on the optical model, the first two factors are dependent on the accuracy of integration in Eq. (2.86) and different grid topologies.

The idea of present effort is to increase the accuracy of integration in Eq. (2.86) by introducing Gauss-Lobatto quadratures. By means of quadrature integration it is possible to cluster points of integration at both ends of the tracing ray. Thus, the application of Gauss-Lobatto quadrature is two fold: reduction of the number of points required to accurately integrate Eq. (2.86) and clustering of points at the region of active quantum transitions.

The second opportunity to improve the efficiency of RTM is the optimization of the search algorithm to determine gas properties along the tracing ray. While a significant amount of search methods to define the nearest neighbor are proposed (Cover and Hart, 1967), present work deals with curvilinear structured grids as well as unstructured grids.

View-factor approach

The view-factor (VF) approach (in some literature it is called the *zonal method*) has been originally proposed by Hottel and Cohen (1958) for absorbing, emitting and nonscattering media with a constant absorption coefficient. The VF approach is used to evaluate the radiation energy exchange between surfaces and volumes in the enclosure. The key idea of VF approach is in the division of the radiating media into isothermal volume and surface

zones and establishing a geometric factor, the so called view factor, of the energy exchange between them. The meaning of the view factor is the fraction of energy emitted by the radiating element which reaches the receiving element accounting for the attenuation by participating media. The general expression for the view factor between emitting volume and receiving surface is given by Eq. (2.88), which is the backbone when one attempts to calculate the radiation flux density on the surface of space vehicles. When it is desired to account for the radiation energy exchange between elementary volumes, Eq. (2.89) is applicable:

$$S_i V_j = \int_{S_i} \int_{V_j} \tau_{ij} \frac{\kappa_j J_j \cos\theta_{ij}}{\pi r_{ij}^2} dV_j dS_i, \tag{2.88}$$

$$V_i V_j = \int_{V_i} \int_{V_j} \tau_{ij} \frac{\kappa_i \kappa_j J_j}{\pi r_{ij}^2} dV_j dV_i, \tag{2.89}$$

where S_i, V_i, V_j are the surface and volumes participating in radiation heat exchange, τ_{ij} is the attenuation factor, κ is the absorption coefficient, r_{ij} and θ_{ij} are the distance between elements and the angle between the normal vector to the surface element and the vector r_{ij}. In Eq. (2.88) and Eq. (2.88) it is assumed that the emitting and receiving elements have index j and i respectively.

The VF approach is an efficient tool for determination of the radiation fluxes as well as the resulting temperature. This method has been later generalized for non-gray and non-isothermal media (Sarofim and Hottel, 1966) as well as for media with scattering (Ma, 1995; Yuen and Takara, 1994). Formulations in Cartesian and cylindrical system of coordinates are also available (Einstein, 1963a,b). the VF approach is used in the engineering application where the spectral properties may be unimportant and VF approach is typically

used to find the temperature on the receiving surface. The advantage of this approach is in the opportunity of the analytical calculation of the view factor for some geometric configurations that greatly simplifies the numerical solution of equation of radiation energy balance (Modest, 2003). The comprehensive review of available exchange factors can be found in Siegel and Howell (2002). It is important to note, that the VF approach generates an asymptotically accurate solution of radiation transfer equation within the adopted optical and thermodynamic model. In other words, at the given optical properties and population of energy levels of atomic and molecular species the VF approach provides an exact value of the radiation flux density.

However, the application of the VF approach has received a little attention in aerothermodynamics where the spatial model of radiation transfer plays a vital role to obtain an accurate solution. One of these problems is the entry and re-entry of space vehicles in atmosphere. Utilization of the VF approach in case of weakly absorbing media between shock wave and the surface of space vehicle is performed in the works by Bose and Wright (2004) and Olejniczak et al. (2003). It is shown that the VF approach demonstrates better accuracy than the tangent slab approximation. The improvement of the accuracy is obtained by automatically capturing the effect of surface curvature and tangential gradients of radiation intensity, unavailable by the TS approximation. Radiation heating rates are obtained for Titan Aeroshell, the mission considered by NASA (Lockwood, 2003). It is shown that the TS approximation severely overestimates the radiation heating rate at the shoulder of the heat shield. The improvement of the accuracy by introducing the VF approach is contrasted by the significant increase of cost by a factor of almost two orders of magnitude.

Present work provides newly derived relations enabling efficient calculation of the spectral radiation transfer in two-dimensional axisymmetric geometry and allowing increase of the efficiency by several orders of magnitude. A semi-analytical solution of radiation flux density is obtained for two dimensional axisymmetric geometry. The performance of the method is investigated in case of significant absorption of radiation as well as three dimensional geometry. To demonstrate the efficiency of the developed methodology, a real flight experiment of space vehicle is considered (Grantham, 1970).

2.10 Conclusion

Governing equations of gasdynamics have been described for the hydrogen flame in low speed jets and the hypersonic flow at the re-entry of the spacecraft. Although considered problems involve the similar finite rate chemical transformations, a different physical background is involved. In this light an interdisciplinary multi-physical approach presents a challenge.

Meanwhile the radiation transfer in high temperature gas is the binding element among almost all components of the multi-physical approach. The coupling and interaction between components of the physical and chemical mechanics including efficient and accurate numerical models of radiation transfer are the area of interest for the present work.

3. COMBUSTION IN COUNTER-FLOWING JETS

3.1 Introduction

The counter-flowing hydrogen-air jet combustion is the classic approach for studying the diffusive flame (Bilger, 1976; Katta et al., 1994; Katta and Roquemore, 2008; Katta et al., 2009). As the velocities of the fuel and air jet increase, the flame becomes thinner and the temperature decreases. The flame also becomes unstable as the strain rate or the scalar dissipation rate approaches the flame-extinction conditions. Nevertheless, it has been shown that a stretched flame will retain a finite thickness before extinction (Katta and Roquemore, 2008; Katta et al., 2009). It is important to note that the flow of the counter-flowing combustion always associates with a stagnation point which occurs in a domain typically characterized by a Reynolds number of, based on the nozzle diameter, less than one thousand. At an ambient temperature T_{amb} equal to 300 K and a low counter-flowing jet speed of a few meters per second, the Mach number is lower than 8x10^{-3}. For this reason, most numerical simulations approximate the chemically non-equilibrium, counter-flowing hydrogen-air combustion as an incompressible flow.

The numerical approach, adopted in Chapter 2, is applied to model hydrogen combustion in counter-flowing jets. The governing system of equations of fluid mechanics is given by the conservation law of mass, Eq. (2.2), momentum Eq. (2.5) and translational-rotational energy Eq. (2.11) for the mean flow. These equations are solved for the conservative variables $(\rho, \rho\mathbf{u}, \rho E)^T$. The vibrational mode is assumed in the equilibrium with translational

and rotational modes.

Binary diffusion coefficient is calculated using Eq. (2.58). The mean diffusion coefficient for species i is calculated using Eq. (2.54). Correction velocity, Eq. (2.57) is applied to conserve the net diffusion mass flux. The individual thermal conductivity and viscosity of species i is calculated by Eq. (2.62) and (2.65). The mixture properties, Eq. (2.59) and (2.63), are applied.

3.2 Geometry and boundary conditions

The combustion in counter-flowing jets is considered as a two-dimensional axisymmetric problem. The computational domain in present calculations is half of the entire domain and restricted by the axis of symmetry as it can be seen from Fig. 3.1. The burner domain is formed by a space between two opposed coaxial tubes carrying molecular oxygen and hydrogen. The outer tube of larger diameter is carrying the flow of pure molecular nitrogen. The inner tube supplies diluted hydrogen from one side of the burner and diluted oxygen from the other side. The distance between the termination of the opposing tubes forms the combustion zone and is equal to 40 mm. The outflow boundary of the computational domain is places on the 40 mm distance from the axis of symmetry. The grid is adapted in the vicinity of the axis of symmetry and presented in Fig. 3.2. The grid contains 202x42 nodes.

The incoming flows of oxygen and fuel go through the boundaries AB and EF in Fig. 3.2. The pure nitrogen comes from boundaries BC and DE. Segment CD is an outflow boundary, boundary AF is an axis of symmetry.

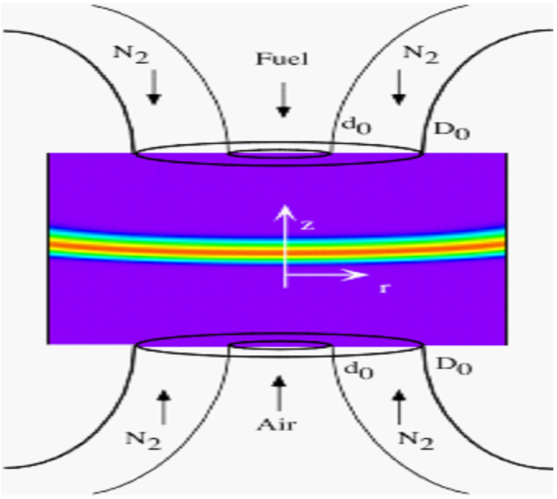

Fig. 3.1: Schematic of counter-flow combustion burner

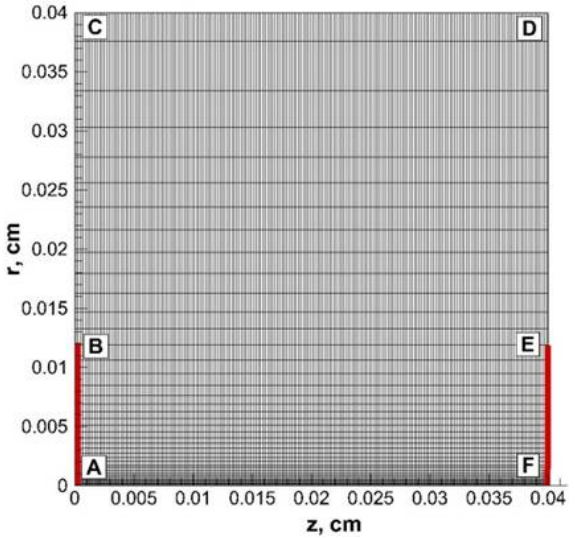

Fig. 3.2: Grid of combustion burner

The compressible N-S equations form an elliptic system of equations when flow is subsonic. Well posed boundary conditions should be specified on the outflow boundary of the closed domain. The well posed condition for pressure, Eq. (2.72) is used. The zero gradient BC for the velocity components, Eq. (2.69) as well as Riemann invariant BC. Eq. (2.70) is applied.

The incoming flow is assumed to be adiabatic. The total temperature and pressure, given by Eq. (2.66) and (2.67) are assumed to be constant when dynamic temperature and pressure are calculated at the inlet boundary. In present study the ambient temperature is T_{amb} = 295 K and the ambient pressure is p_{amb} = 100135 Pa. Radial component of the inlet velocity is set to zero. Boundaries BC and DE are subject to the next boundary conditions: $\nabla P \cdot \vec{n} = 0$, $T = T_{ini}$, $U = U_{wall}$ = 0.37 m/s. U_{wall} is constant for all computed cases. The axis of symmetry implies zero gradients for all primitive variables, except the radial component, which is set to zero.

Boundary conditions for species are formulated for the mass fractions of the species. Boundary AB imposes Y_{O_2} = 0.233 and $Y_{N_2} = 1 - Y_{O_2}$. Boundary EF contains $Y_{H_2} =$ 0.0262 and $Y_{N_2} = 1 - Y_{H_2}$. Mass fraction of the remaining species is set to zero on boundaries AB and EF. Boundaries BC and BD of the external tube contain pure molecular nitrogen: Y_{N_2} = 1. Axis of symmetry AF and outflow boundary CD assume zero gradient for all species.

Initial conditions for gasdynamic variables depend on the employed chemical mechanism. The global single-step reaction, given in Table A.1 and A.2 is an exothermic process, and generates the hydrogen flame without any external supply of heat. This reaction is active at any temperature and no artificial numerical ignition is required to obtain steady-state flame. However the global reaction does not describe the extinction and ignition phenomena and is only used to obtain initial conditions for other computational cases.

Detailed kinetic mechanisms, either by Evans and Schexnayder (1980) or GRI mechanism (Smith et al., 1999) contain intermediate species such as radical OH, H and O. These mechanisms are endothermic at temperatures below the ignition limit and require an external source of energy to initiate the combustion. For purposes of numerical investigation an artificial source of energy has to be chosen to initiate the chains of OH and H production. This term is included in the RHS of energy equation and has to be chosen with precautions due to the large stiffness of governing equations. However the more convenient way to obtain steady state flame assumes no artificial source of energy. Instead of this, once a flame has been obtained by means of the global single-step mechanism, the calculation with detailed mechanism is started with frozen gasdynamic variables, assuming initial conditions by global reaction. After a converged solution for all species has been obtained, the

evolution gasdynamic variables are released.

3.3 Numerical procedure for gasdynamic equations

The numerical procedure for the governing equations of gasdynamics based on the Navier-Stokes formulation is based on the flux vector splitting algorithm, described by Huang in Huang and Coakley (1992). The formulation include a line-by-line Gauss-Seidel algorithm using Roes approximate Riemann solver (Roe, 1981) and TVD properties (Harten, 1983). To simplify the development, the basics process of discretization will be given in Cartesian coordinates. However, the complete curvilinear coordinates derivation has been made (Huang and Coakley, 1992). The discretized approximation across the control volume can be given as:

$$\frac{Q^{n+1}-Q^n}{\Delta t}\Delta x\Delta y + F_{x,e}\Delta y - F_{x,w}\Delta y + F_{y,n}\Delta x - F_{y,s}\Delta x = \tag{3.1}$$
$$G_{x,e}\Delta y - G_{x,w}\Delta y + G_{y,n}\Delta x - G_{y,s}\Delta x + S\Delta x\Delta y,$$

where $F_{x,e}$,$F_{x,w}$,$F_{y,n}$,$F_{y,s}$ and $G_{x,e}$,$G_{x,w}$,$G_{y,n}$,$G_{y,s}$ are the components of the inviscid and viscous flux vector approximated at grid points $(i+1/2, j)$, $(i-1/2, j)$, $(i, j+1/2)$ and $(i, j-1/2)$. The interfacial inviscid flux $F_{i+1/2}$, staggered between nodal points i and i+1 is given by the Roe's approximation (Roe, 1981). The components of the inviscid flux are treated by the central differencing approximation:

$$F_{i+\frac{1}{2},j} = \frac{1}{2}[F_{i+1,j} + F_{i,j} + \hat{F}_{i+1,j} + \hat{F}_{i,j} - |A+\hat{A}|_{i+\frac{1}{2},j}(U^{n+1}_{i+1,j} - U^{n+1}_{i,j})] \tag{3.2}$$

The last three terms in Eq. (3.2) are included to satisfy the TVD properties (Harten, 1983). The Jacobean matrix, A, is defined as:

$$A = \frac{\partial F_i}{\partial U} = R^{-1}\Lambda R.$$

where R is the similarity matrix R of the inviscid flux vector, obtained by diagonalization. The Roe's approximation between the two adjacent cells gives:

$$F_{i+1} - F_i = A_{i+\frac{1}{2}} \left(U_{i+1}^{n+1} - U_i^{n+1} \right),$$

where $A_{i+1/2}$ is based on the Roe's average state. The TVD flux difference is defined as:

$$\hat{F}_{i+1} - \hat{F}_i = \hat{A}_{i+1/2} \left(U_{i+1}^{n+1} - U_i^{n+1} \right).$$

The diffusive flux G is divided into two parts, one involving the normal component and the other containing the rest. The former part is treated implicitly and the latter is evaluated explicitly. By substituting Roes approximation and TVD flux difference formulas into the discretized governing equations in the form of five-point scheme is obtained:

$$C_P U_P^{n+1} = C_P^0 U_P^{n+1} + C_E U_E^{n+1} + \tag{3.3}$$
$$C_W U_W^{n+1} + C_N U_N^{n+1} + C_S U_S^{n+1} + \left(G_e^{'} - G_w^{'} \right) \Delta y + \left(G_n^{'} - G_s^{'} \right) \Delta x + S^n \Delta x \Delta y$$

To be consistent with the classical approach used in gasdynamic program codes (An-

derson et al., 2012), Eq. (3.3) is transformed into the delta-form:

$$C_P \Delta U_P = C_E \Delta U_E + \Delta C_W U_W + \Delta C_N U_N + \Delta C_S U_S + RHS^n,$$

where RHS includes the TVD component of the inviscid flux, diffusive flux and source term. The detailed development of the numerical scheme can be found in Huang and Coakley (1992).

3.4 Species mass conservation

Equation (2.4) is solved in the curvilinear system of coordinates (ξ, η) given by transformation $\xi = \xi(x,y)$,$\eta = \eta(x,y)$ and Jacobean $J = |\partial(x,y)/\partial(\xi,\eta)|$. The complete derivation is omitted for brevity, however major points are emphasized. The convective terms in Eq. (2.4) are approximated by the first order upwind scheme. The diffusion terms are approximated by the second order central-difference scheme. The resulting five-point scheme has the appearance of:

$$C_{i,j} U_{i,j}^{n+1} = A_{i,j}^{+} U_{i+1,j}^{n+1} + A_{i,j}^{-} U_{i-1,j}^{n+1} + B_{i,j}^{+} U_{i,j+1}^{n+1} + B_{i,j}^{-} U_{i,j-1}^{n+1} + F_{i,j}^{n+1}, \qquad (3.4)$$

where:

$$A_{i,j}^{\pm} = A_{i,j}^{\pm,conv} + A_{i,j}^{\pm,diff} = \mp \frac{1}{2\Delta\xi_{ij}^{\pm}} \left(M_{i\pm\frac{1}{2},j}^{U} \mp \left| M_{i\pm\frac{1}{2},j}^{U} \right| \right) + \frac{1}{2\Delta\xi_{ij}^{\pm}\Delta\xi_{ij}} \left(E_{i\pm1,j} + E_{i,j} \right),$$

$$B_{i,j}^{\pm} = B_{i,j}^{\pm,conv} + B_{i,j}^{\pm,diff} = \mp \frac{1}{2\Delta\eta_{ij}^{\pm}} \left(M_{i\pm\frac{1}{2},j}^{V} \mp \left| M_{i\pm\frac{1}{2},j}^{V} \right| \right) + \frac{1}{2\Delta\eta_{ij}^{\pm}\Delta\eta_{ij}} \left(F_{i\pm1,j} + F_{i,j} \right),$$

$$C_{i,j} = A^{+}_{i,j} + A^{-}_{i,j} + B^{+}_{i,j} + B^{-}_{i,j} + \frac{\rho_{i,j}}{\Delta t J_{i,j}},$$

$$F_{i,j} = F^{cross}_{i,j} + \frac{\rho_{i,j} D_{i,j}}{J_{i,j}\Delta t}\left(\xi^{y}_{i,j}\frac{U^{n}_{ij+1} - U^{n}_{ij-1}}{\xi_{ij+1} - \xi_{ij-1}} + \eta^{y}_{i,j}\frac{U^{n}_{i+1j} - U^{n}_{i-1j}}{\eta_{i+1j} - \eta_{i-1j}}\right) + \frac{\rho_{i,j}U^{n}_{i,j}}{J_{i,j}\Delta t} + \frac{\dot{\omega}_{i,j}}{J_{i,j}} + F^{cons}_{i,j},$$

$F^{cross}_{i,j}$ and $F^{cons}_{i,j}$ are the components in the RHS due to the presence of the cross derivatives of the curvilinear coordinates and correcting diffusion velocity $\mathbf{v}_{corr}$,

$E_{i,j} = \rho_{i,j} D_{i,j}\left(\left(\xi^{x}_{i,j}\right)^2 + \left(\xi^{y}_{i,j}\right)^2\right)/J_{i,j}$, $F_{i,j} = \rho_{i,j} D_{i,j}\left(\left(\eta^{x}_{i,j}\right)^2 + \left(\eta^{y}_{i,j}\right)^2\right)/J_{i,j}$, $\Delta\xi^{-}_{ij} = \xi_{i,j} - \xi_{i-1,j}$, $\Delta\xi^{+}_{ij} = \xi_{i+1,j} - \xi_{i,j}$, $\Delta\xi_{ij} = \left(\xi_{i+1,j} - \xi_{i-1,j}\right)/2$, $\Delta\eta_{ij} = \left(\eta_{ij+1} - \eta_{i,j-1}\right)/2$, $M^{U}_{i,j} = \frac{\rho_{i,j}}{J_{i,j}}\left(U_{i,j}\xi^{x}_{i,j} + V_{i,j}\xi^{y}_{i,j}\right)$, $M^{V}_{i,j} = \frac{\rho_{i,j}}{J_{i,j}}\left(U_{i,j}\eta^{x}_{i,j} + V_{i,j}\eta^{y}_{i,j}\right)$, Δt is a time step. Superscripts n and n+1 correspond to the current and next time level. Equation (3.4) is solved by Gauss-Seidel algorithm.

The particular chemical mechanism brings the stiffness to Eq. (3.4). Typically, the maximal allowed CFL number for gasdynamic time step with the loosely coupled species mass conservation equation is approximately equal to 5. The allowed CFL number used to solve Eq. (2.21) is lower. It is found that for global single-step mechanism CFL number can be as high as 0.1, for kinetic mechanism with the detailed chemistry the maximal allowed CFL number is of the order of 5x10^{-3} - 10^{-2}.

3.5 Chemical and Thermodynamical model

Three kinetic models have been chosen to validate the finite rate combustion mechanism. The first model is a global single-reaction mechanism of combustion which includes only species of fuel and oxidant and the resultant species of combustion, that is, water. The reaction with appropriate Arrhenius coefficients is presented in A.1 and A.2 in Appendix

A.

The second model is taken from Evans and Schexnayder (1980) and has been simplified. The present model contains 8 species (H, O, H_2, O_2, OH, H_2O, HO_2 and N_2) and 16 reactions. This model contains Arrhenius forward and backward coefficients for reaction rates, which are summarized in Appendix A.3 and A.4.

The third model is taken from the database of Gas Research Institute (Smith et al., 1999)) and contains 9 species (H, O, H_2, O_2, OH, H_2O, HO_2, H_2O_2, N_2) and 59 reactions. Only forward reaction rates are specified in the original model. The backward reaction rates are calculated from the constant of equilibrium:

$$K_k = \left(\frac{P/10^5 Pa}{RT}\right)^{\sum_{i=1}^{N_c} v_{ki}} \exp\left(\frac{\Delta S_k^0}{R} - \frac{\Delta H_k^0}{RT}\right).$$

The change of entropy ΔS_k^0 and enthalpy ΔH_k^0 in chemical reaction k is calculated as:

$$\frac{\Delta S_k^0}{R} = \sum_{i=1}^{N_c} v_{ki} \frac{S_i^0}{R}$$

and

$$\frac{\Delta H_k^0}{R} = \sum_{i=1}^{N_c} v_{ki} \frac{H_i^0}{RT},$$

where S_i^0 and H_i^0 are the standard entropy and enthalpy of species i, calculated using curve fit data provided by GRI. Thermodynamic properties of species are approximated as a polynomial of temperature:

$$\frac{S_k^0}{R} = a_{1k} \ln T + a_{2k} T + \frac{a_{3k}}{2} T^2 + \frac{a_{4k}}{3} T^3 + \frac{a_{5k}}{4} T^4 + a_{7k},$$

$$\frac{H_k^0}{RT} = a_{1k} + \frac{a_{2k}}{2}T + \frac{a_{3k}}{3}T^2 + \frac{a_{4k}}{4}T^3 + \frac{a_{5k}}{5}T^4 + \frac{a_{6k}}{T}.$$

Coefficients a_{jk}, j=1...7 are given in Smith et al. (1999) and are not provided here.

3.6 Results

Seven cases C1 - C7 of the hydrogen combustion in counter-flowing jets have been investigated. Mach number of the inlet flow and global strain rate are given in Table 3.1. The characteristic Reynolds number is based on the radius of the inner coaxial tube, and the characteristic length scale of the flowfield is based on the distance between inlet boundaries of the counter-flowing jets. The simulated strain rate covers the range from the essentially diffusive laminar to the nearly turbulent flame in the extinction state. Although the Reynolds number reaches a value of 1.6x10^4, the turbulent model is not introduced to simplify the analysis of the flame characteristics. The geometry, mesh, and boundary conditions except at the inlet boundary are identical for all sets of computations.

#	Mach number	Reynolds number	Strain rate, s^{-1}
C1	7.50x10^{-3}	1038	129.8
C2	1.29x10^{-2}	2305	215.3
C3	1.72x10^{-2}	3270	277.8
C4	2.58x10^{-2}	5472	410.9
C5	4.30x10^{-2}	9900	674.5
C6	5.16x10^{-2}	11926	808.6
C7	6.88x10^{-2}	16169	1088.0

Table 3.1: Parameters of the inlet flow

3.6.1 Validation against reference solution

The comparison of flow field and flame structure for the case C1 between solutions obtained by the artificial compressibility method and compressible N-S equations is given. The chemical kinetic mechanism of the comparing calculation contains 13 species (H_2, O_2, H, O, H_2O, OH, HO_2, H_2O_2, N_2, NO, N_2O, NO_2, N) and uses GRI thermodynamic database (Smith et al., 1999). The flame peak temperature, thickness, location and maximal concentration of H_2O and OH are the parameters for comparison. On the axis of symmetry, the flame thickness is measured by the distance between the grid points with the temperature greater than 1.1xT_{amb}. The flame location is assigned to the grid point on the axis of symmetry by the maximal temperature of the flame front. All reported concentrations of species are referred to at their location on the axis of symmetry.

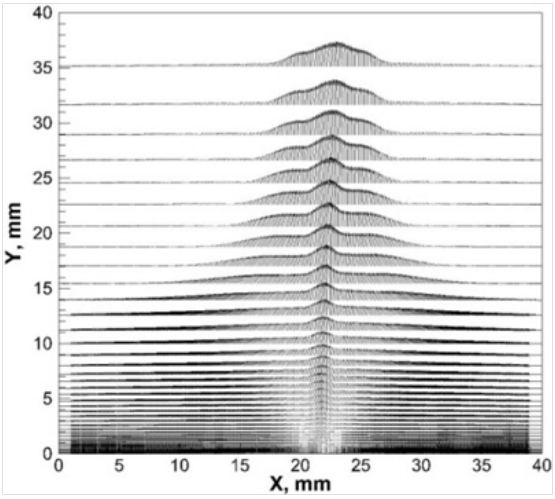

Fig. 3.3: Vector field of velocity, case C1, reference solution

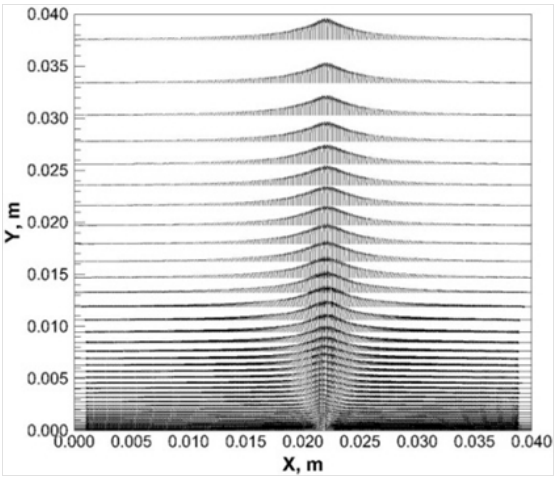

Fig. 3.4: Vector field of velocity, case C1, present work

The velocity vector field is given in Fig. 3.3 and 3.4. The coordinates x and y correspond to the axial and radial direction, respectively. Temperature contours for analogous

calculations are depicted in Fig. 3.5 and 3.6. The peak temperature reasonably matches to the result by the artificial compressibility method and the present study with a difference of 7%. The difference in peak temperature increases toward downstream up to a magnitude of 10%. Both solutions predict a slight increasing of temperature and the mass fraction of H_2O toward downstream, which means that combustion is sustained all the way to the exit boundary. In fact, the distribution of H_2O is essentially replicated by the shape of the flame front. The present result reveals a more diffusive flame: at the exit boundary the difference in the flame thickness between the comparing solution and the present study indicates a value of 2.3 mm.

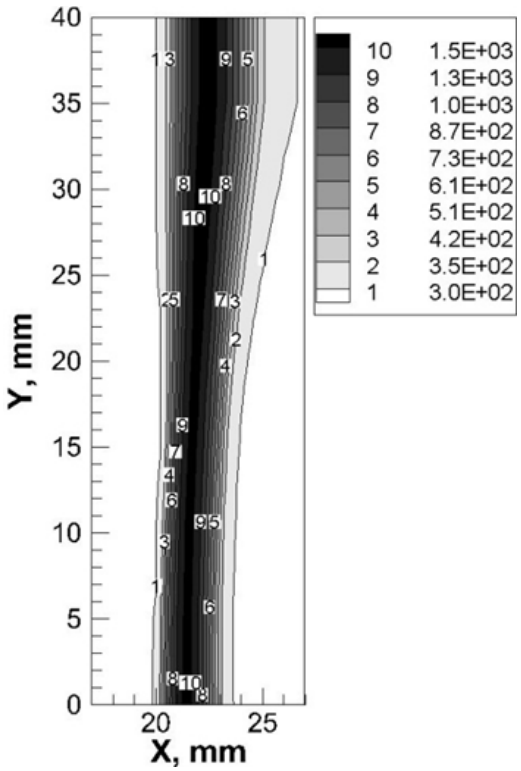

Fig. 3.5: Temperature, K, reference solution

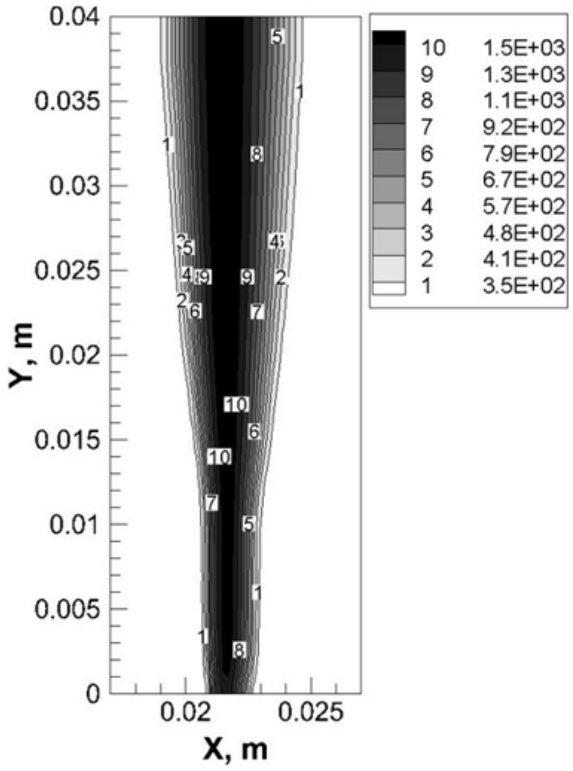

Fig. 3.6: Temperature, K, case C1, present work

The peak concentrations of water and OH are summarized in Table 3.2. The solution

by artificial compressibility method predicts the highest peak mass fraction of H_2O equal to 0.128, while the results by N-S equations is 10-30% lower. The greatest difference from reference data is by global chemical mechanism, indicating that a single reaction is not applicable for accurate description of the hydrogen flame. The mass fraction of radical OH is found to be more sensitive to the chemical mechanism. The maximal mass fraction for reference solution is 0.00238, and the difference for GRI and Evans models is 26% and 18 %, respectively. The difference in species concentration is due to the lower temperature of the flame generated in present work. Axial distribution of all species is given in Fig. 3.7 and 3.8. The reference solution is shown in Fig. 3.9. One can see that the distribution of atomic hydrogen and oxygen duplicates the behavior of water mass fraction and spans over a greater distance in the reference solution than in the solution generated in the present work. However the peak values of all major and trace species are in good agreement with the depicted data. The hydrogen peroxide has the lowest concentration in the flame front, predicted by both present work and the reference solution as low as 10^{-5} per unit mass. The diminishing behavior of H_2O_2 depletion is duplicated by HO_2 from the side of O_2 supply. The concentration of H_2O diminishes much slower toward the cold region beyond the flame front in the reference solution. This is confirmed by the difference in the flame thickness observed in Fig. 3.10.

The location of the stagnation point in Fig. 3.11 is predicted by both approaches with a difference of 0.9 mm. The artificial compressibility method predicts the maximal flame temperature at 1556 K in Fig. 3.10. The compressible N-S equations with GRI, Evans et al. and global chemical mechanisms predict the maximum temperatures 1365, 1454 and 1336 K, respectively. All results generated by these three mechanisms indicate the flame location

with a difference of 0.08 mm between each other, and the difference with the reference data is 0.9 mm. The thickness of flame produced by compressible N-S equations is within the dimensions between 2.4 and 2.5 mm, while the flame thickness of the reference flame is 3.4 mm on the axis of symmetry.

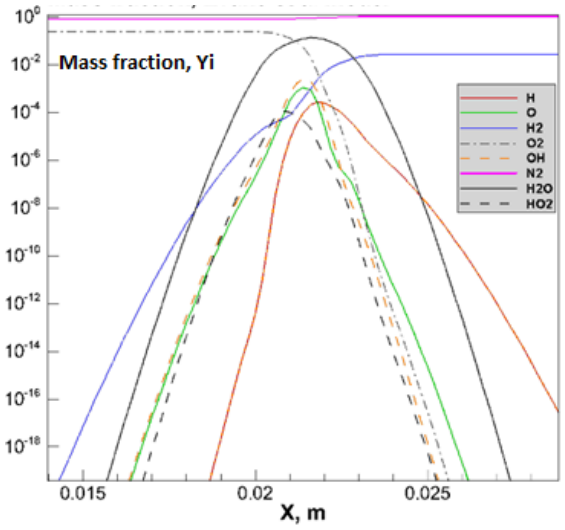

Fig. 3.7: Mass fraction, Evans mechanism

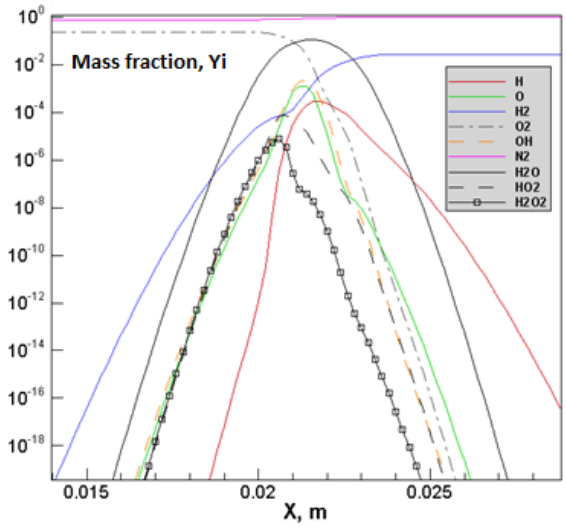

Fig. 3.8: Mass fraction, GRI mechanism

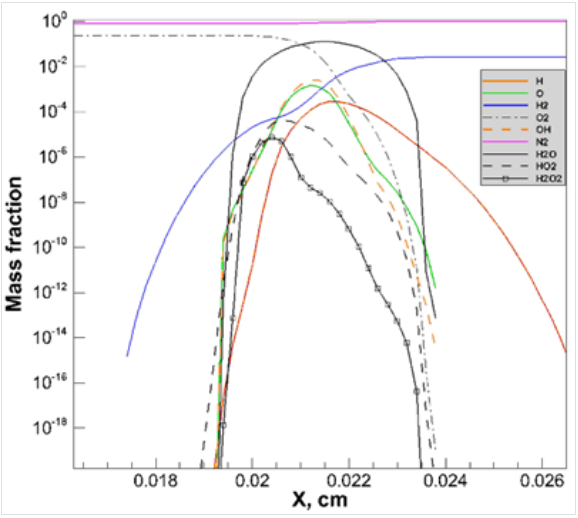

Fig. 3.9: Mass fraction, reference data

	Katta (2011)	GRI	Evans	Global
Flame temperature, K	1556	1365	1454	1336
Flame thickness, mm	3.4	2.4	2.5	2.5
maximum Y_i, OH	$2.38x10^{-3}$	$1.75x10^{-3}$	$1.95x10^{-3}$	-
maximum Y_i, H_2O	$1.28x10^{-1}$	$1.16x10^{-1}$	$1.19x10^{-1}$	$8.8x10^{-2}$

Table 3.2: Flame characteristics, case C1

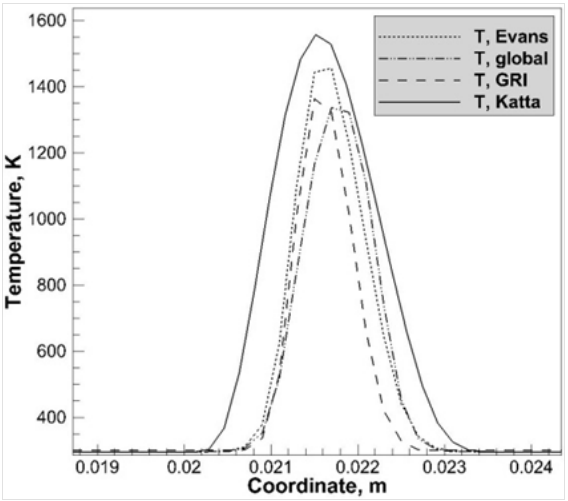

Fig. 3.10: Temperature distribution, axis of symmetry

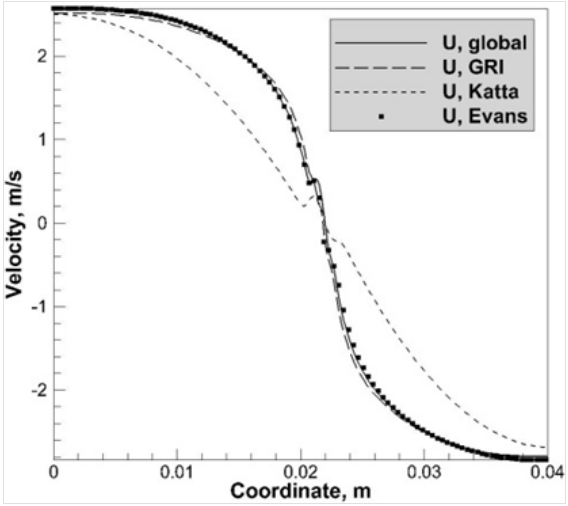

Fig. 3.11: Axial component of velocity, axis of symmetry

The comparison of the axial component of velocity is depicted in Fig. 3.11. The minor bump located at the flame front is captured accurately. Present approach shows a detectable difference from the velocity provided by artificial compressibility method. The profile generated by compressible N-S equations indicates that counter-flowing jets gradually decelerate on the way to the stagnation point faster than in the incompressible counterpart solution. The discrepancy in the slope of the axial velocity may explain the difference in the flame thickness between present and reference data. The difference in the velocity vector is theoretically affected by the following factors:

- Chemical kinetic models
- Transport properties
- Boundary conditions
- Numerical approach
- Dilatation of the normal stress tensor.

The following discussion provides information on each of these factors. The difference introduced by the transport properties is studied first for the comparison with the flame simulation utilizing the artificial compressibility method. For this purpose, the kinetic theory formula is applied to the set of chemical species and the thermodynamic state obtained from the comparing simulation. The comparison is conducted for the mixture diffusion coefficient D_i of water, mean flow viscosity μ and thermal conductivity λ.

3.6.2 Transport properties

The comparison of the diffusion coefficient of water is given in Fig. 3.12. The comparison of the molecular viscosity and thermal conductivity of the gas mixture is presented in Fig. 3.13. The maximum difference is 2.2%, 0.53% and 15% for the diffusion coefficient, viscosity and thermal conductivity, respectively. In theory, the large difference in the thermal conductivity is caused by omitting the contribution from the vibrational mode of molecular species, which is equal to the rotation contribution in thermal conductivity, according to the Eucken relation. Satisfactory agreement between the transport properties confirms the fact that the adopted approximation derived from the kinetic theory generates a reasonable flame profile in the counter-flowing jets in the given temperature range.

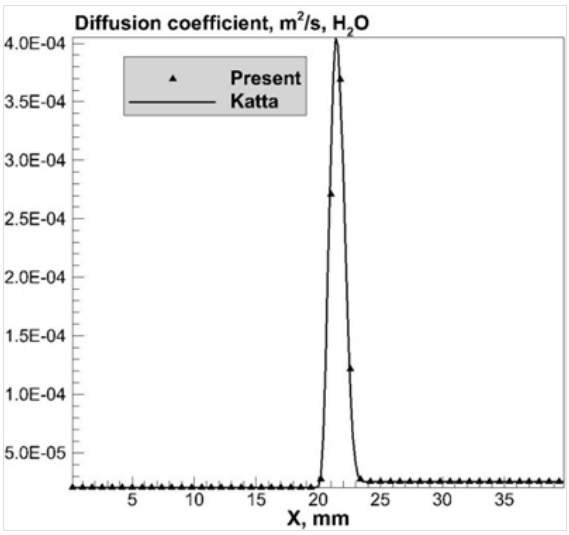

Fig. 3.12: Diffusion coefficient of H_2O, solid line is the reference solution, symbols is the present work

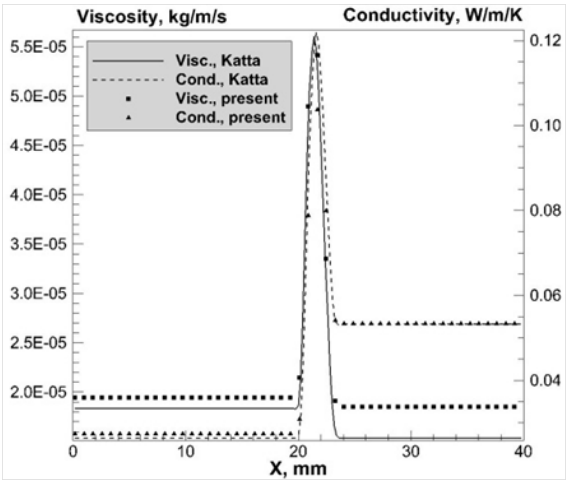

Fig. 3.13: Gas viscosity and conductivity, solid and dashed lines is the reference solution, symbols is the present work

3.6.3 Boundary conditions

Axial component of velocity for case C1 is presented in Fig. 3.14 for two types of boundary conditions. At a given inlet flow velocity U_{ini} = 2.5 m/s, the velocity distributions generated by two different BC indicate a slight difference in the vicinity of inlet boundary. The rest of the flow field exhibits essentially the same axial component of velocity profile, indicating the identical slope of axial component of velocity. One can conclude from this observation that the implementation of different BC does not significantly affect the flow.

3.6.4 Influence of numerical scheme

The behavior of the adopted numerical approach is studied by simulation of counter flowing jets without introducing combustion phenomena. Only mean flow is considered. Transport and thermodynamic properties are taken as air properties at room temperature. The range

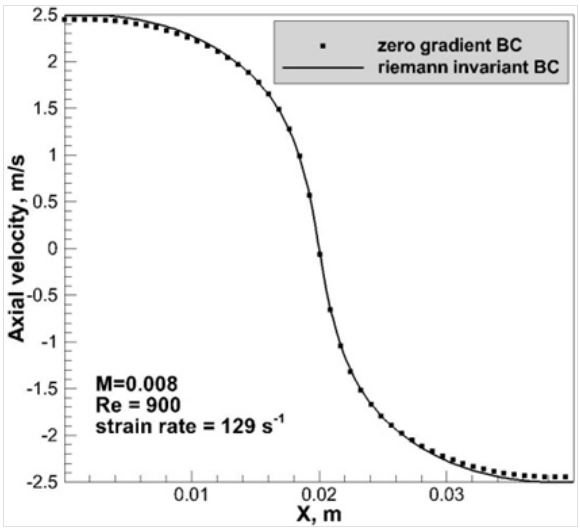

Fig. 3.14: Axial component of velocity, solid line is BC based on Riemann invariant, symbols is no-change BC

of Mach number is from 7.5x10^{-3} to 2x10^{-1} as it is reflected in Table 3.1. The distribution of velocity along axis of symmetry for cases C1-C7 is shown in Fig. 3.15. The axial component of velocity is normalized by the velocity at the inlet boundary. The slope of axial component of velocity decreases as the Mach number goes up. Starting at M = 7.5x10^{-3}, both jets decelerate rapidly, in contrast with calculations by the artificial compressibility method, which exhibits a nearly linear change in axial component of velocity with coordinate. The axial velocity profiles given by present approach in Fig. 3.11 and 3.14 with or without combustion initiated, is similar to each other, except for the bump at the flame front. In other words, the combustion does not significantly alter the deceleration rate of jets near the stagnation point. At the increasing Mach number, the axial component of velocity generated by present approach becomes nearly linear.

3.6.5 Dilatation term in shear stress

It is therefore logic to focus on the difference in normal stress component between the compressible and incompressible flow. For the latter, the dilatation in the stress tensor is absent by virtue of the degenerated conservation equation in which $\nabla \cdot \mathbf{u} = 0$. The component of the stress tensor for the incompressible equation becomes

$$\sigma_{ii} = \mu \left[\frac{\partial u^i}{\partial x^j} + \frac{\partial u^j}{\partial x^i} \right],$$

that is different from the compressible counterpart. The axial velocity profile generated by the incompressible formulation is contrasted against compressible solution, and is presented in Fig. 3.16. Although no claim is made that the present numerical approach will generate more accurate results, the numerical results substantiate the negligible contribution by the dilation term.

By the insignificant difference in transport properties between kinetic theory and perfect gas approximation, as well as, the consistent pattern of velocity profiles with different types of boundary conditions, an important conclusion about the influence of governing equations on the flame and jet profiles may be drawn. First, the compressible flow solutions exhibit a distinct difference in the axial velocity distribution from the incompressible result. Namely, compressible flow solution shows steeper decelerating slope than the incompressible formulation near the stagnation point for flows with or without combustion. The difference in the slope of the axial velocity leads to a thinner flame front in comparison with the incompressible flow. As the flame propagates further toward the outer computa-

tional domain, it becomes more diffusive in contrast to the solution by the incompressible equation. By examining further the two types of boundary conditions and the different transport properties, it brings no significant difference to light. Therefore it is logic to attribute the difference in the flame predictions to the compressibility of the flow formulation. Especially the counter-flowing jet phenomenon is driven by the axial compression.

3.6.6 Simulation at different strain rate

The combustion is studied for the strain rate in the range from 129 to 1088 s^{-1} which corresponds to the laminar diffusion flame to the state where flame became unstable and extinguish, as it can be seen in Fig. 3.15. However, the investigation of flame behavior is still not complete, because the present computations do not include a turbulence model beyond the critical Reynolds numbers. Nevertheless the basic characteristics of a diffusive flame can still be analyzed using the present approach. It is expected that before the complete extinction of a flame, the computational simulation will demonstrate a gradually decreased flame thickness at an increasing strain rate. The instability of the flame front is mainly caused by convective and diffusive heat loss exceeding the heat generated due to chemical reactions through combustion. The presented results show that flame front becomes thinner, but the transient instability of the flame front has not been captured. The physical instability is obstructed by a diagonal dominance numerical procedure, biased to yield a steady state asymptote.

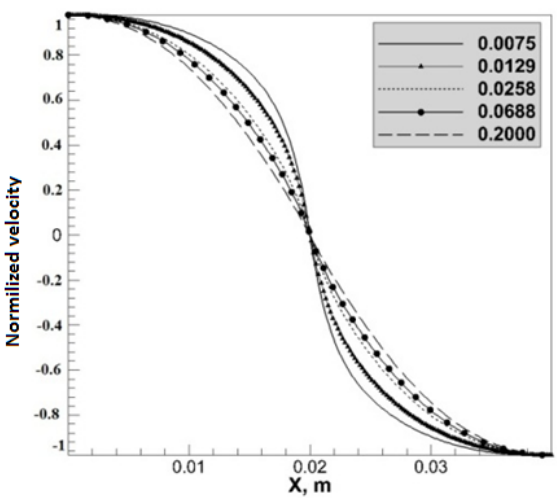

Fig. 3.15: Axial component of velocity, different strain rate and inlet Mach number

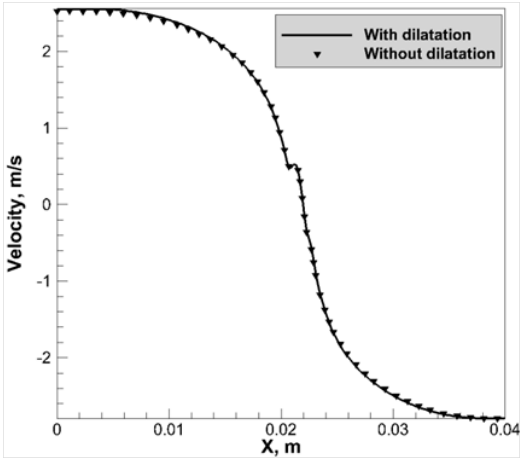

Fig. 3.16: Axial component of velocity, solid line - full form of shear stress, symbols - dilatation term is omitted

3.6.7 Important flame characteristics

According to the classic theory of diffusion flames, the flame thickness is a function of mean free path and the number of collisions in the flame front. In Zeldovich et al. (1985) it was showed that the flame thickness is inversely proportional to the square root value of the applied strain rate a . The fact comes from that the characteristic thickness of the mixing layer can be defined through the balance of convective-diffusive mass transfer and proportional to $\sqrt{D/a}$, where D is the characteristic diffusion coefficient. As the peak flame temperature decreases and the flame is stretched when the counter-flowing jets are brought together at a higher speed, as shown in Fig. 3.17. The concentration of the radical OH as well as H_2O goes down when strain rates goes up, causing the flame temperature to decrease. The flame thickness plotted against $1/\sqrt{a}$ in Fig. 3.18. As anticipated, the flame thickness at low strain rate is inversely proportional to $\sqrt{a}$. The flame thickness l is fitted as a linear function of a and displays in Fig. 3.18 with the dashed line. At the strain rate

greater than 400 s^{-1}, the flame thickness departs,as expected, from the linear dependence. This deviation is due to the increasing heat loss in the flame to free stream at a higher strain rate and a progressively diminishing flame temperature.

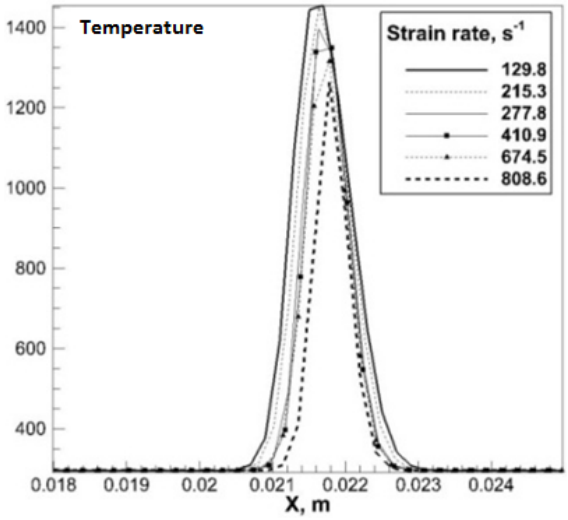

Fig. 3.17: Axial distribution of temperature, K, at different global strain rates

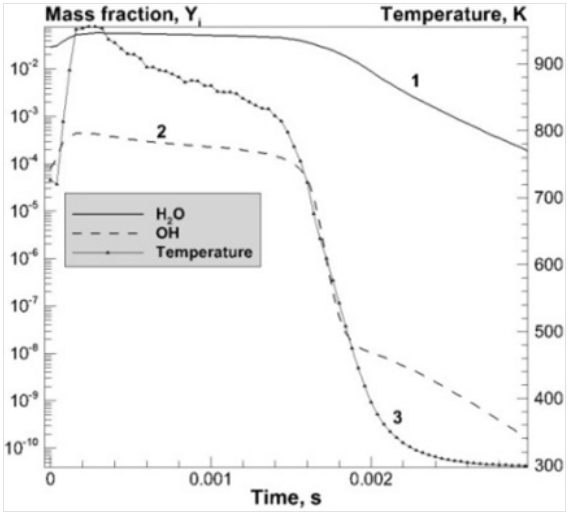

Fig. 3.18: Temperature and mass fraction of OH and water at strain rate a = 1088 s^{-1}

At the strain rate of 1088 s^{-1} the flame extinction is observed. The global chemistry mechanism does not reproduce the phenomena of flame extinction at a higher strain rate, because the combustion mechanism is exothermic at any temperature. The evolution of OH and H_2O mass fraction and temperature given by the kinetic model of Evans et al is shown in Fig. 3.19 at fixed location x = 2 cm in the flame front. Mass fraction of water gradually vanishes; this behavior is duplicated by OH radical. The flame extinction, recognized by the decrease of Y_{i,H_2O} is not a linear function of time but has a steep drop at a temperature near 790 K. The rapid diminishing of the flame at this temperature can be characterized as an explosion limit of H_2/O_2 mixture. Diagram of the pressure-temperature explosion in a stoichiometric H_2/O_2 mixture is presented in Fig. 3.20. According to this

data, the explosion limit is nearly 823 K at the pressure of 1 atm. The difference between observed explosion temperatures and conventional results in Fig. 3.20 can be explained by the different stoichiometric ration of fuel and oxidizer, which is 1.79 for the present simulation.

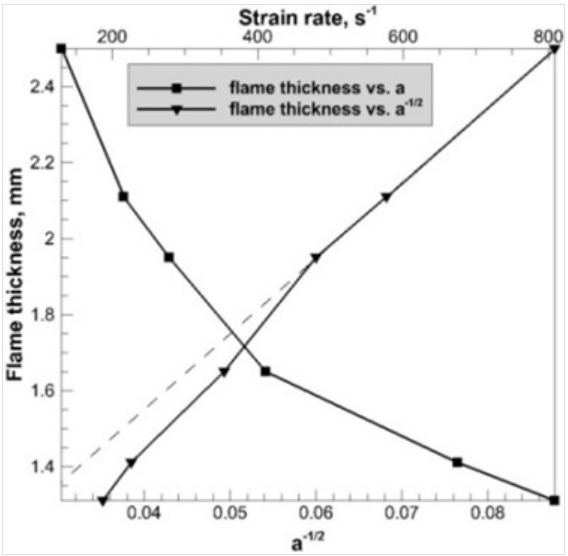

Fig. 3.19: Flame thickness, mm vs. the global strain rate, s^{-1} and $1/\sqrt{a}$

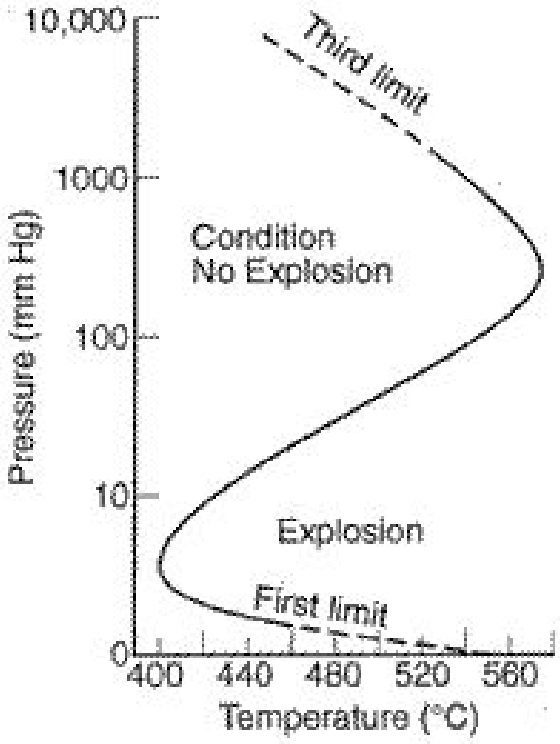

Fig. 3.20: Explosion limit of the stoichiometric hydrogen-air mixture

3.7 Conclusion

The finite rate chemistry model is loosely coupled with the compressible N-S equations for describing the combustion in counter-flowing hydrogen and oxygen jets. Present simulation is verified by a comparison with a reference solution obtained by the artificial compressibility method. Reasonable agreement is reached for the flame thickness, maximum of the

flame temperature and concentration of major species. Three kinetic mechanisms with a different number of species and reactions are implemented to explore the physical behavior of the laminar non-premixed adiabatic flame. Seven different strain rates covering the range from 129 to 1088 s^{-1} are investigated for flame thickness, species concentrations and temperature in the flame front.

The flame becomes stretched as strain rate increases. It has been confirmed that the flame thickness is inversely proportional to the square root value of the global strain rate at a low Mach number. At higher strain rates the flame thickness is diminishing faster than the established relationship. This fact indicates that the convective mass transfer dominates over the diffusion mechanism. The extinction of the flame is recognized by the rapid diminishing of the OH and H_2O mass fraction. At a global strain rate a = 1088 s^{-1} a flame extinction is observed. An analysis of species in the flame reveals that the OH concentration vanishes in a similar manner as a peak temperature. The time evolution of the flame temperature is nonlinear with a steep drop at 790 K. The flame extinction at this temperature recognized as the explosion limit is in a good agreement with the available theoretical data.

The solution generated by compressible Navier-Stokes equations experiences a steep deceleration of the axial component of velocity in comparison to the reference solution by the conventional method. This difference leads to a thinner flame at the stagnation point. A comprehensive study of the boundary conditions, transport properties, chemical mechanism and dilatation term in the shear stress did not reveal the reason of the different flame thickness. However, present approach is able to describe the physical behavior of hydrogen flame and generally is competitive with the conventional method of artificial

compressibility.

4. HYPERSONIC FLOW

4.1 Introduction

The population of energy levels in gas can significantly depart from the Boltzmann distribution downstream the strong shock waves or in the rarefied hypersonic flows at the spacecraft re-entry. Although the thermodynamic equilibrium eventually occurs downstream the flow in the relaxation zone of the shock layer, the internal modes of energy immediately behind the shock front may not be in the equilibrium state.

In the absence of thermodynamic equilibrium the conventional definition of temperature, defined by the population of all energy levels of all internal modes cannot be used to describe the thermodynamical state of the ensemble of particles under the non-equilibrium conditions. In order to access the population of specific energy levels the state-to-state approach should be applied to resolve all excitation and deactivation processes taking place on every energy level. Some limitations exist at the present time before this approach can be fully applied. The cross section database of collisional and radiative processes is limited and does not cover all possible transitions and conditions. Besides, the state-to-state approach is computationally prohibitive and typically applied only to solve one-dimensional stagnation line problems.

Another approach to model the non-equilibrium flow is to assume that each internal mode (rotational, vibrational and electron-electronic mode) has an individual temperature and the energy exchange between modes occurs through the relaxation processes. This

approach is usually referred to as the multi-temperature model. It allows an efficient modeling of the non-equilibrium phenomena in hypersonic flows. However the accuracy of this approach is not acceptable when gas media is rarefied or the shock waves are very strong. For example, the orbital re-entry of a spacecraft can be successfully considered by the multi-temperature approach (Candler and MacCormack, 1991) and no attempt has been made to apply existing collisional-radiative models for this type of problem. However, if the re-entry velocity is high (i.e. superorbital re-entry), the application of multi-temperature model may be not accurate (Panesi et al., 2009).

During the re-entry in the low altitudes of atmosphere and/or moderate entry velocities the rotational mode is typically assumed to be in equilibrium with translational mode, since only a few collisions are required to reach translational-rotational equilibrium. However this is not true for vibrational and electron-electronic modes. Strictly speaking, the vibrational mode of each kind of molecules has to be considered separately. To compute non-equilibrium flow field at re-entry of space vehicles typically three vibrational modes of NO, N_2 and O_2 molecules as well as conservation of electron-electronic energy are required.

Present work considers the flight experiment of RAM-C II probe conducted nearly four decades ago. The data collected during the re-entry of the conical probe with spherical bluntness serves as a classical tool for the hypersonic code validation and comparison of the adopted thermodynamic and chemical models against the electron number density measured at four different locations on the probe surface during the re-entry. For the past two decades a significant number of theoretical investigations (Boyd, 2007; Candler and MacCormack, 1991; Farbar et al., 2013; Josyula and Bailey, 2003; Scalabrin and Boyd, 2006)

have been published to validate the models of finite rate chemistry and non-equilibrium model of dissociation in the re-entry environment.

Most of the works are limited to finite rate, 7 or 11 species air chemistry and two- or three-temperature models for thermodynamical non-equilibrium in a post-shock region. The comparison of the critical electron number density is typically provided along the normal direction to the surface with the data collected by reflectometers at four points along the space vehicle. The assessment of the data recorded by the Langmuir probe at the end of the probe is provided less often (Boyd, 2007; Farbar et al., 2013; Vlasov et al., 1997).

The analysis of conductive heating rates is performed only in a few number of papers (Tchuen and Zeitoun, 2009). The radiation heating rates, presented in Chapter 5 were not previously published. Meanwhile, since the composition of air plasma in the vicinity of the probe is fairly well known and validated, it may be useful to compare the heat flux to the surface since it strongly depends on the chemical and thermodynamical models. Although the experiment data on the heat flux is not available it is considered that the additional verification of existing models of hypersonic flow maybe useful.

This chapter is structured as follows. First of all, an attempt is made to bring an up-to-date chemistry model, thermodynamic model and transport properties together to access the species composition and heating rates. The multi-temperature model is employed for the non-equilibrium effects in air plasma. Although the state-to-state approach is more accurate for calculations when a deviation from Boltzmann equilibrium is observed, owing to the higher cost and restricted knowledge of the cross-section data, the state-to-state approach is discarded to access species composition over the entire length of RAM-C II probe. Instead

of this a three-temperature model is developed by assigning individual vibrational temperatures to molecular species N_2, O_2 and NO and individual electron-electronic balance of energy. The three-temperature model was proposed only briefly before at a near-equilibrium point of trajectory (Josyula and Bailey, 2003).

Second, the spatial distribution of the electron number density measured by the Langmuir probe got a little of attention in literature. Only a limited number of works reported comparison with the rake data (Boyd, 2007; Farbar et al., 2013). However the model developed in this work allows reasonable prediction of the rake data for the non-equilibrium stage of trajectory.

Finally, the conductive heating rates are reported. Results of numerical simulation agree with previously reported data by (Tchuen and Zeitoun, 2009) and a discussion on the sensitivity to the chemical model is presented. The radiation heating rates are obtained by the ray tracing method for the entire trajectory of RAM-C II probe and a spectral multi-group flux density is presented in Chapter 5.

4.2 Governing equations

For the high enthalpy hypersonic environment the flow structure is best captured by shock-fitted structured grids. On each discrete grid point, the kinematic, thermodynamic properties, and the composition of the flow medium are generated by solving the interdisciplinary governing equations consisting of the conservation of mass of the mean flow, compressible Navier-Stokes equation, total energy equation, law of mass action and the internal energy conservation equations for vibrational and electron-electronic degrees of freedom.

It is worthwhile to note that the set of governing equations intended to describe the structure of the hypersonic flow is different from the governing equations of the combustion phenomena. For low speed combustion problem the accurate treatment of transport properties of the flow (i.e. diffusion mechanism of species mass transport) is required, since the main features of hypersonic flow are governed by the convective terms in Navier-Stokes equations and chemical and thermodynamical models of the flow field.

The governing equations used in present work have been summarized previously in (Feldick et al., 2009; Liu et al., 2010; Olynick et al., 1999; Park et al., 2001; Shang and Surzhikov, 2012, 2011), details and solution methodologies are discussed in Chapter 2. To access the properties of the flowfield generated by the entry of RAM-C II the governing equations of the mean flow are solved in the form of Eq. (2.2), (2.4), (2.5) and (2.11). The thermodynamic model is described by Eq. (2.12) and (2.16).

The kinetic model used in present study adopts the law of mass action in the form of Eq. (2.22). Forward and backward reaction rates are computed from the Arrhenius equations (2.23) and (2.24). Two chemical models by Park (Park, 1993) and by Dunn and Kang (Dunn and Kang, 1973) are employed. To study the phenomenon of non-equilibrium dissociation a number of models are applied, including the empirical model by Park, (Park, 1988), preferential models of dissociation by Treanor and Marrone (Marrone and Treanor, 1963; Treanor and Marrone, 1962) as well as β-model by Losev (Losev et al., 1995) and model of Macheret-Fridmann (Macheret and Fridman, 1994). The vibrational-translational and vibrational-electron relaxation are employed in the Landau-Teller's form, Eq. (2.27).

4.3 Review of previous work

The flight experiment RAM-C II serves as a classical benchmark for hypersonic computer code validation and comparison of the adopted thermodynamic and chemical models against the electron number density number measured during the re-entry. For the past two decades a significant number of theoretical investigations (Boyd, 2007; Candler and MacCormack, 1991; Farbar et al., 2013; Josyula and Bailey, 2003; Scalabrin and Boyd, 2006) have been published to validate the model of finite rate chemistry and non-equilibrium model of dissociation in the re-entry environment.

One of the first works attempted to numerically reproduce the data provided by reflectometers is by Candler and MacCormack (Candler and MacCormack, 1991). The seven species chemical model has been used and rates for forward reaction and constants of equilibrium were taken from Park (1985) except the associative ionization, taken from Wray (1961). The empirical model by Park (1989) was employed to model non-equilibrium dissociation. Multi-temperature model was incorporated to account for the non-Boltzmann population of energy levels. The overall agreement with data by reflectometers was achieved for the wide range of trajectory stage of 61 - 81 km.

The cross section of the collisional process between electrons and heavy particles and the probability of vv' relaxation are chosen empirically. Namely, the cross section σ_{eT} was chosen to be equal to 10^{-20} m^2, and the probability to transfer the *entire* amount of the vibrational energy stored in the exited species through the collision was chosen to be a constant and equal to 10^{-2}. The boundary conditions for species concentrations were fully non-catalytic although for charged particles the super-catalytic condition would be more

appropriate (Park, 1989).

A comprehensive study of RAM-C II and RAM-C III flights was conducted in (Vlasov et al., 1997). The concentration of the free electron gas at the base of the vehicle was studied. Three different temperatures for N_2, O_2 and NO were considered. Electron temperature T_e was assumed to be equal to the vibrational temperature of N_2. Rates of vv' and vT energy exchange were taken from the experimental data and extrapolated to the high temperatures using SSH theory (Losev et al., 1994). Vibrational-dissociation coupling is modeled by Marrone-Treanor model (Marrone and Treanor, 1963) with the empirical parameter of preferential dissociation $U = D/3R$. The rate of molecular oxygen dissociation were taken from (Losev et al., 1994). Forward rate of the exchange reaction N_2 + O = NO + N was taken from the experimental work by (Monat et al., 1979) in the modified form by Bose and Candler (1997) for the case of vibrational non-equilibrium:

$$k\left(T\right) = 2 \cdot 10^{12} T^{1/2} exp(-38000/T).$$

The rate of reactions involving N_2^+, O_2^+ and NO^+ was taken from (Park, 1989). Boundary conditions for species and vibrational temperature have received a special treatment. The boundary condition for vibrational energy was obtained by assuming the finite probability of molecule deactivation during the interaction with the wall (Scott, 1975). The appropriate energy equation for the deactivation probability γ can be written as follows:

$$\gamma_m \rho_m \sqrt{\frac{RT_g}{2\pi M_m}} \left(e_v\left(T_g\right) - e_v\left(T_w\right)\right) = \lambda_v \frac{\partial T_v}{\partial x} + J_m \left(e^\star - e_v\left(T_g\right)\right), \tag{4.1}$$

where the index m denotes the type of molecule, T_g is the translational temperature of the gas near the wall, M is the mass of molecule, J_m is the mass flux of molecule, $e^\star$ denotes the vibrational energy of molecule that retains after recombination with the wall, and is to be determined. It is worthwhile to note that the time-dependent energy equation was solved to determine the temperature of the surface, allowing direct implementation of Eq. (4.1).

The wall boundary condition for the concentration of charged particles was formulated considering Bohm's effect rather than apply the super-catalytic BC (Raizer et al., 1991). More accurate formulation of the boundary condition for the ion concentration inevitably involves the concept of Knudsen layer, which implies that the velocity distribution of particles near the solid surface is non-Maxwellian because the collisions with the surface are more often than between particles. By means of this concept, the ion flux to the surface appears to be the function of electron temperature and ion concentration beyond the Knudsen layer:

$$J_{ion} = \frac{1}{2} n_{i,Kn} \sqrt{\frac{2kT_e}{M_i}} \left(1 + \frac{T_{i,Kn}}{T_e}\right), \tag{4.2}$$

where the subscript Kn refers to the quantities evaluated immediately outside of the Knudsen layer.

The study of RAM-C II experiment has been performed not only by adopting the continuous gasdynamic approach but also by means of Monte Carlo principles (Bird, 1989; Boyd, 2007). In Bird (1989) the critical electron number density and heating rate have been reported at an altitude of 81 km. The chemical mechanism by Bortner (1966) has been used. A general underestimation of experimental data has been observed, which may be explained by the limited computational resources at that time. The heating rate at stagnation

point has been reported as high as 100 W/cm^2.

A better agreement of numerical data with the experiment was presented by (Boyd, 2007). Two models were employed to model chemical reactions in the hypersonic flow: total collision energy model (Bird, 1994) and vibrationally favored dissociation (Haas and Boyd, 1993). Experimental results on the critical density of electron gas fall in the range of the numerical simulation, produced by different chemical models. The spatial distribution of the electron concentration near the location of Langmuir probe is also in good agreement with the experiment.

The heating rates are reported only in a few papers. In (Tchuen and Zeitoun, 2009) a large discrepancy of results is observed by employing different sets of chemical reactions (Dunn and Kang, 1973; Gardiner, 2000; Park, 1985; Wray, 1961). For example, at the altitude of 71 km stagnation heating rate is in the range between 58 and 263 W/cm^2. The great discrepancy of results make the additional investigation of computational models a required study.

4.4 Present numerical results

Three re-entry trajectory points of RAM-C II probe are simulated at the altitudes of 81, 71 and 61 km (Jones and Cross, 1972). The ambient temperatures increase from 198.64, 219.58, to 254.80 K as the probe is descending, and the corresponding Mach numbers decrease from 28.4, 25.9, to 23.9 accordingly. The Reynolds numbers based on the nose radius of 15.24 cm span from 1,590, 6,280, to 19,500. The entire investigated domain is treated as a laminar flow. The basic configuration of the RAM-C II probe is a hemispheric-

nosed cone with a semi-cone angle of nine degrees and an overall length of 1.2954 m. The grid refinement study is carried out by comparing results on two axisymmetric body-conformal meshes with clustered grid spacing by the dimensions of (187 x 93, coarse mesh) and (327 x 187, fine mesh) nodes.

The employed flux splitting scheme possesses the carbuncle studied previously in Ismail et al. (2009); MacCormack (2011); Yee (1987). In order to avoid convergence difficulties and computational artifacts in present calculations, the limiting procedure of eigenvalues is introduced and applied to the the staggered inviscid flux:

$$\vec{F}_{i+\frac{1}{2}} = \frac{1}{2}\left[\vec{F}_i + \vec{F}_{i+1} - \left|\hat{A}\right|_{i+\frac{1}{2}} (U_{i+1} - U_i)\right] \tag{4.3}$$

where $\left|\hat{A}\right|_{i+\frac{1}{2}}$ has eigenvalues $\left|\lambda^l_{i+\frac{1}{2}}\right|$, l = 1 ... 4 in two dimensional geometry. The entropy fix is applied as:

$$\left|\lambda^l_{i+\frac{1}{2}}\right| = \begin{cases} \left|\lambda^l_{i+\frac{1}{2}}\right|, \left|\lambda^l_{i+\frac{1}{2}}\right| \geq \varepsilon \\ \left(\left|\lambda^l_{i+\frac{1}{2}}\right|^2 + \varepsilon^2\right)/2\varepsilon, \left|\lambda^l_{i+\frac{1}{2}}\right| < \varepsilon \end{cases}$$

An adjustable parameter ϵ can be a chosen constant but according to the report (Yee, 1987) the most reasonable choice of ϵ is given as

$$\varepsilon = \varepsilon_0 f\left(U_{i+\frac{1}{2}} + V_{i+\frac{1}{2}} + C_{i+\frac{1}{2}}\right),$$

where ϵ_0 is constant (in this work taken as 4x10^{-3}) and f goes from 0 to 1, vanishing near the surface of a blunt body. After applying the entropy fix the carbuncle is vanished. The sonic line which serves as an indicator of carbuncle effect (MacCormack, 2011) demon-

strates no defect as shown in Fig. 4.1.

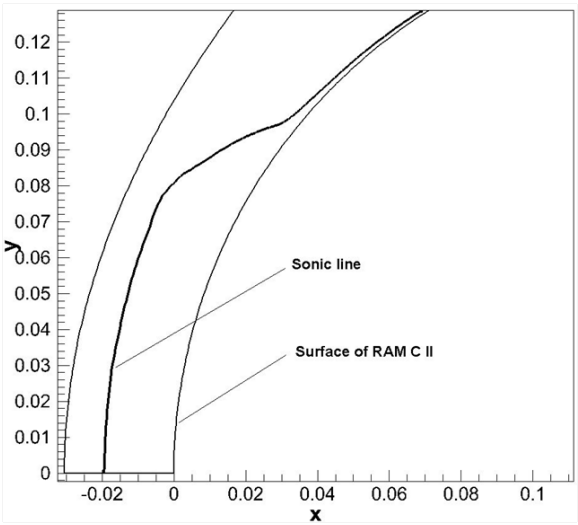

Fig. 4.1: Sonic line in the RAM-C II flow, altitude of 61 km

4.4.1 Macroscopic parameters and grid study

The study of temperature and pressure distribution is provided first. At each altitude three sets of calculations are preformed, considering the flow as a perfect gas with no chemistry, with finite rate chemistry and in thermal equilibrium and assuming finite-rate chemistry and non-equilibrium model for preferential dissociation. The non-equilibrium model is adopted from the work by Marrone and Treanor (1963) with the empirical parameter $U = D/6R$. The calculations of finite rate chemistry are performed with Park's model (Park, 1989).

It is important to obtain optimal grid refinement to achieve convergent results, especially in the region of high gradients, e.g. the shock front and near the surface. Typically for the problem of RAM-C II entry grids 50 - 80 nodes along axial direction are used. The implicit procedure of numerical solution of Navier-Stokes equations and chemistry module permits fine grid calculations, since it was previously demonstrated that the high value of

$Damköhler$ number requires a very fine grid to resolve flow properties near the surface (Shang and Surzhikov, 2010).

The set of computations corresponding to the coarse and fine grid is presented in Fig. (4.4). Black solid and dashed lines correspond to the temperature distribution obtained from the fine and coarse meshes, red solid and dashed lines correspond to the pressure distribution from fine and coarse grids. The fine grid computation shows that mesh spacing is critical to capture the shock wave as well as maximum temperature in shock layer. The given results show that the difference in 150 K is observed between two sets of calculations. It can be seen from Fig. 4.6 and 4.7 that the electron number density in the shock layer varies with grid resolution resulting in a nearly 10 % difference. Other species do not experience this strong dependence from grid resolution. Electrons are generated in the shock layer primarily by the associative ionization mechanism which has very strong temperature dependence.

The dependent variables within the relaxation zone are strongly affected by dissociation of nitrogen and oxygen as well as non-equilibrium effects. The greatest impact is observed at lower altitudes and is shown in Fig. 4.2 when the dissociation is most significant. The difference between the thermodynamically equilibrium and non-equilibrium calculations increases at the higher altitudes when the non-equilibrium effects are stronger, as it can be seen in Fig. 4.3. All sets of calculations are shown in Fig. 4.2, 4.4 and 4.3 demonstrates that pressure is not effected by non-equilibrium phenomena since it not defined by internal degrees of freedom.

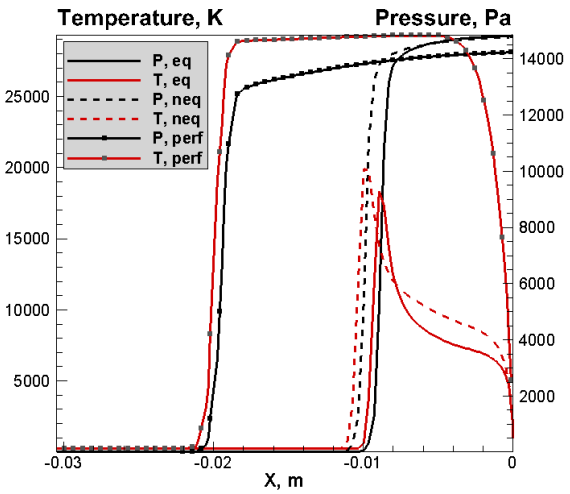

Fig. 4.2: translational temperature and pressure at stagnation streamline, perfect gas, equilibrium and non-equilibrium calculations, 61 km

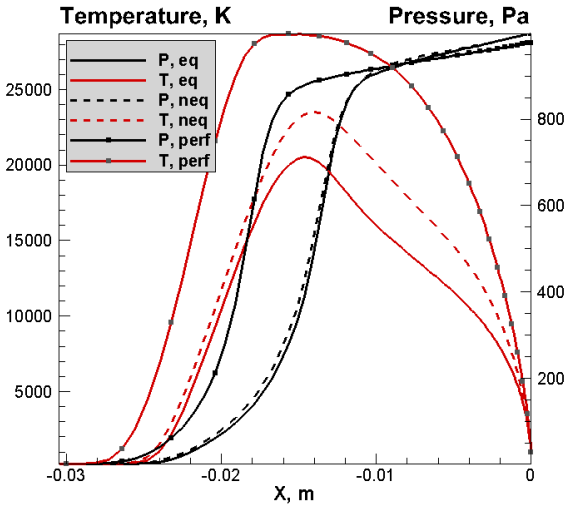

Fig. 4.3: translational temperature and pressure at stagnation streamline, perfect gas, equilibrium and non-equilibrium calculations, 81 km

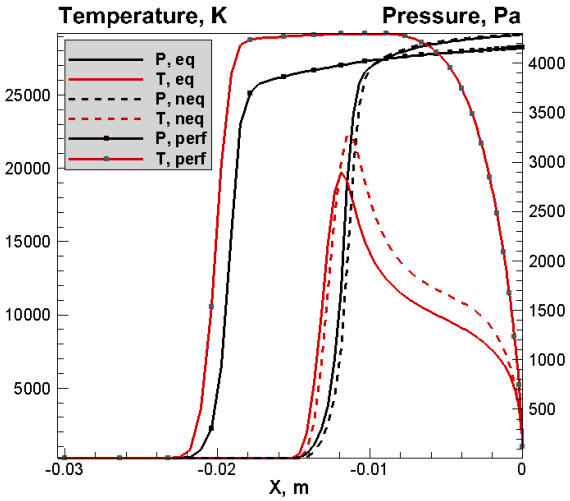

Fig. 4.4: T, P, stagnation streamline, perfect gas, equilibrium and non-equilibrium calculations, 71 km

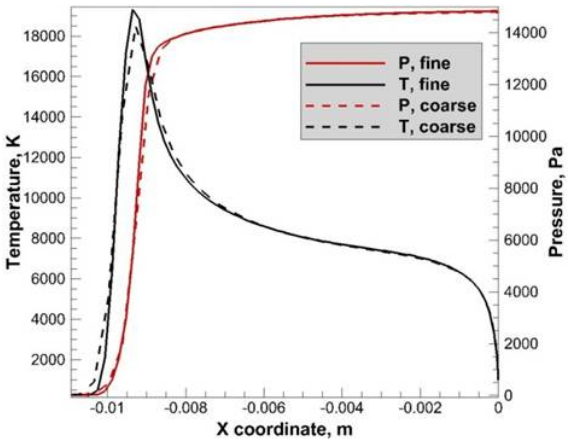

Fig. 4.5: T, P, stagnation streamline, perfect gas, equilibrium and non-equilibrium calculations, 61 km

4.4.2 Chemical composition

The shock front is usually smeared at high altitudes since the mean free path is large and the distance, required to convert the kinetic energy of the flow to thermal energy by collisional

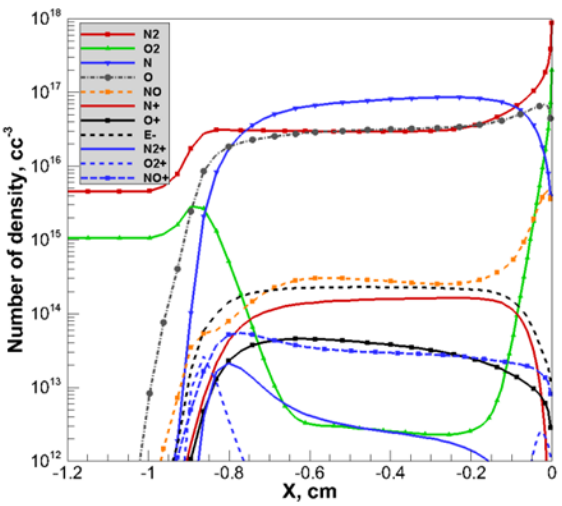

Fig. 4.6: Species number density, coarse mesh, 61 km

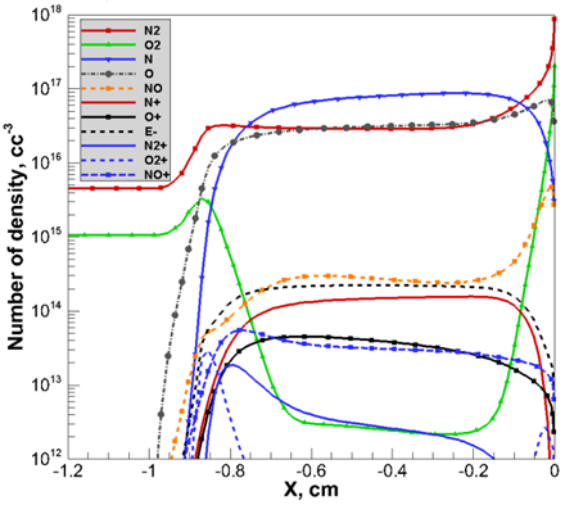

Fig. 4.7: Species number density, fine mesh, 61 km

processes is comparable to the characteristic size of the vehicle, as it can be seen in Fig. 4.3. At the same time the fraction of dissociated molecules is less at high altitudes despite the fact that the peak temperature in the shock front is higher compared to the situation occurring at lower altitudes. This is due to the fact that the Mach number at high altitudes is higher for the same velocity of flight. The deceleration of space vehicle is insignificant due to rarefied atmosphere thus the absolute velocity of capsule is nearly the same throughout altitudes 61 - 81 km for RAM-C II probe. For the same reason the speed of sound is lower at higher altitudes, resulting to a higher Mach number at this altitude of trajectory.

The lower degree of dissociation is primarily due to the lower number of collisions between particles at high altitudes. Calculations performed in the present work indicate the incomplete dissociation of molecular oxygen at the altitudes between 71-81 km as shown in Fig. 4.8, 4.9, 4.10 and 4.11, reflecting the chemical composition for different model of non-equilibrium dissociation. The present calculations correspond to the Park chemical

mechanism (Park, 1993) with either Park or Treanor-Marrone model of dissociation. The

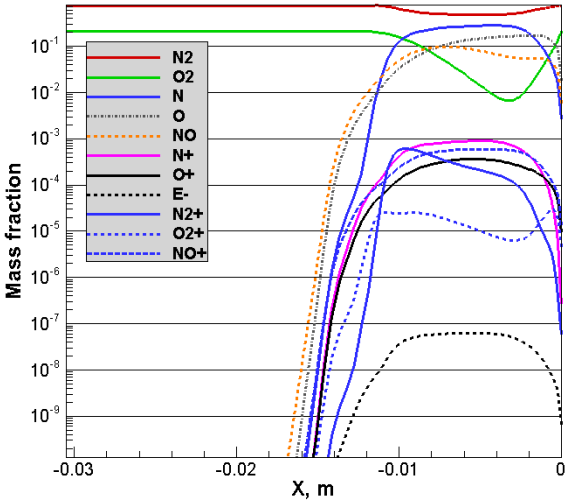

Fig. 4.8: Species mass fraction, Treanor-Marrone model, 71 km

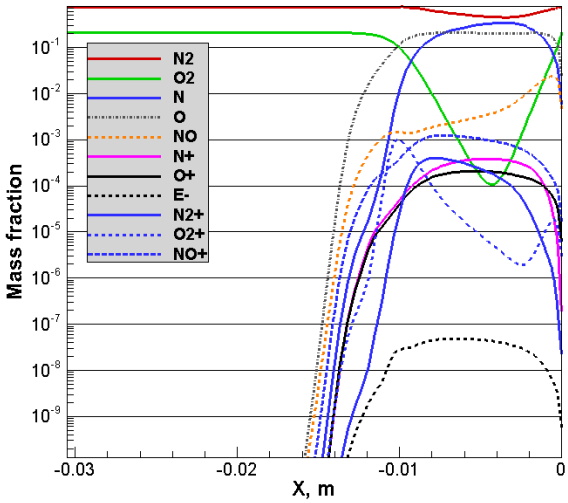

Fig. 4.9: Species mass fraction, Park model, 71 km

dissociation degree of molecular nitrogen is relatively small compared to the oxygen in computed cases. At the altitude of 71 km the minimal mass fraction of N_2 is 0.46 and 0.50 for the model of non-preferential and preferential dissociation respectively. However, a significant difference in mass fraction of dissociated oxygen is found for these two models. In case of non-preferential dissociation it is 10^{-4} and for preferential dissociation it is 6.7x10^{-3}. The same conclusion can be made for calculation at the trajectory point 81 km at stronger non-equilibrium conditions. For nitrogen the minimal mass fraction is 0.673 and 0.678 and for oxygen it is 0.0447 and 0.136 by the non-preferential and preferential models of dissociation, respectively.

The difference in the dissociation rate of molecular oxygen under the conditions of non-equilibrium excitation of internal DOF between Park's and Treanor-Marrone's models is greater at the case of 71 km, where the incident flow is less rarefied and carries signifi-

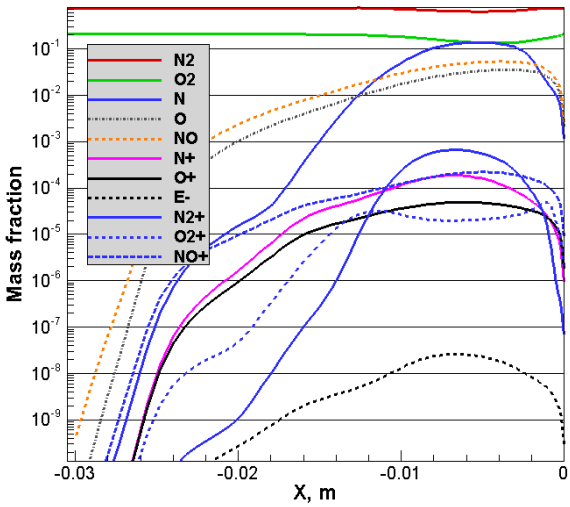

Fig. 4.10: Species mass fraction, Treanor-Marrone model, 81 km

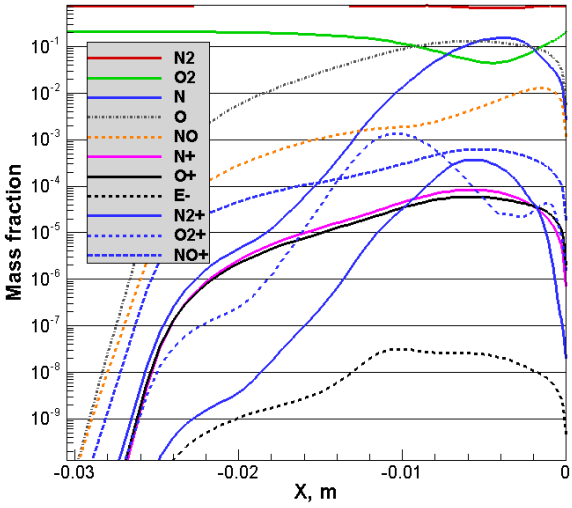

Fig. 4.11: Species mass fraction, Park model, 81 km

cantly more of kinetic energy. At the same time, it was known (see, for example, (Gnoffo et al., 1989)) that in case of strong shock waves the non-preferential model may be a more appropriate model than the preferential dissociation model that uses the concept of "ladder climbing". In other words, when the flow is highly energetic, the excitation and dissociation of vibrational degree of freedom from lower states may happen by a single collision with particle rather than the gradual increasing of vibrational quantum number via multiple collisions. This point of view is also confirmed by present calculations.

The influence of the non-equilibrium dissociation model and chemical mechanism on translation temperature is provided in Fig. 4.12 at the altitude of 81 km. Solid line corresponds to the calculation with the Park's chemical mechanism under the assumption of thermodynamically equilibrium flow, long dashed line is the Park's kinetic mechanism with the first preferential dissociation model (Treanor and Marrone, 1962), U = ∞, circle symbols are the Park's kinetic mechanism with the non-preferential model of dissociation,

square symbols are the Park's mechanism with the second preferential dissociation model (Marrone and Treanor, 1963), $U = D/6R$, short dashed line is Dunn and Kang's kinetic model with the second preferential model of dissociation (Marrone and Treanor, 1963).

The employment of any model of non-equilibrium dissociation is increasing the translation temperature for the entire shock layer. This fact is expected since the dissociation is slower at non-equilibrium conditions and more energy is remained in the translational mode of the flow. However the temperature between different non-equilibrium models significantly differs. Comparison of the temperature curves generated by Dunn and Kang's and Park's kinetic mechanisms shows the similar behavior of temperature profile only above the region where chemical transformations become significant, at x = -0.013 m, as it can be seen in Fig. 4.11. In the relaxation zone the difference between these two chemical mechanisms can be as great as 2500 K.

It is important to analyze the influence of the empirical factor in the model of preferential dissociation. First of all, one can see, that the first model of preferential dissociation with the empirical parameter $U = \infty$, which imposes the equal probability of dissociation from any vibrational level ν, gives a different profile of temperature from non-preferential model and the model with finite U at the very moment when vibrational modes becomes active, i.e. starting at x = -0.022. This is due to the strong non-equilibrium conditions at altitude 81 km. However, the preferential model of dissociation with $U = D/6R$ demonstrates surprisingly good agreement with empirical model by Park except in the region immediately behind the peak translational temperature, at x = -0.012 m.

The distribution of vibrational temperature of molecular oxygen for different models

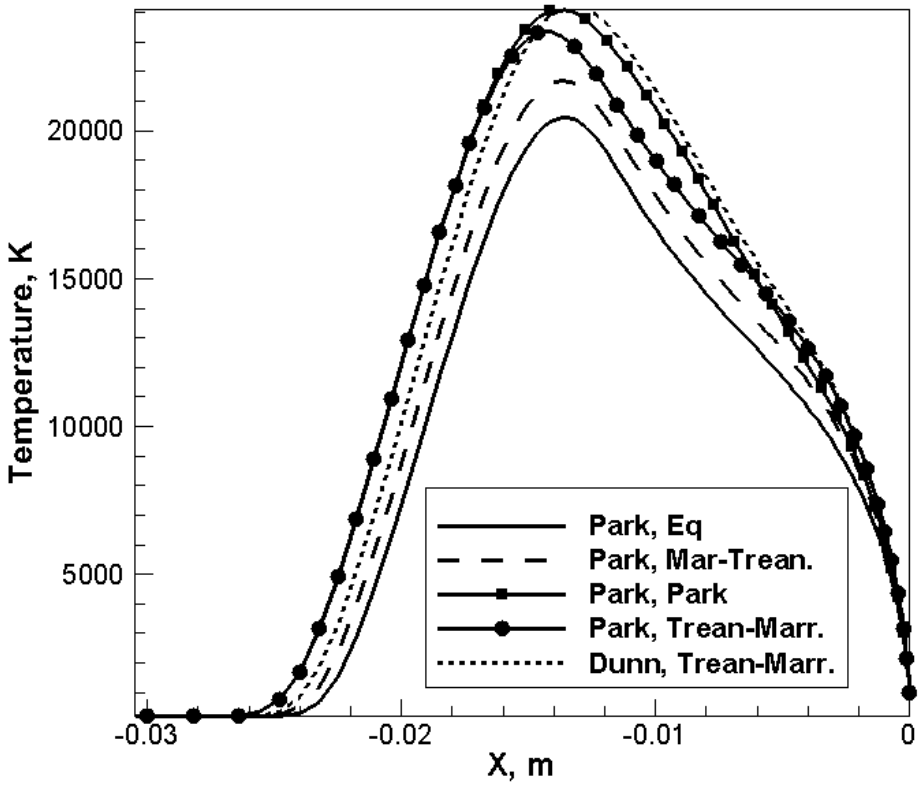

Fig. 4.12: Translational temperature, K, altitude of 81 km

of non-equilibrium dissociation is shown in Fig. 4.13 at the altitude of 81 km. All calculations are performed for Park kinetic mechanism. The slowest rate of vibrational excitation is demonstrated by the model of Treanor and Marrone with equal probability of dissociation for all vibrational levels, as shown by the long dashed line in Fig. 4.13. The good matching between the profile of translational temperature for preferential and non-preferential models is also confirmed by the behavior of vibrational temperature. Furthermore, one should note the good agreement of Dunn and Kang's and Park's chemical mechanisms using the same model of dissociation.

The vibrational temperature is governed by the conservation equation formulated for the vibrational energy of molecular gas species. Within the framework of the two - temper-

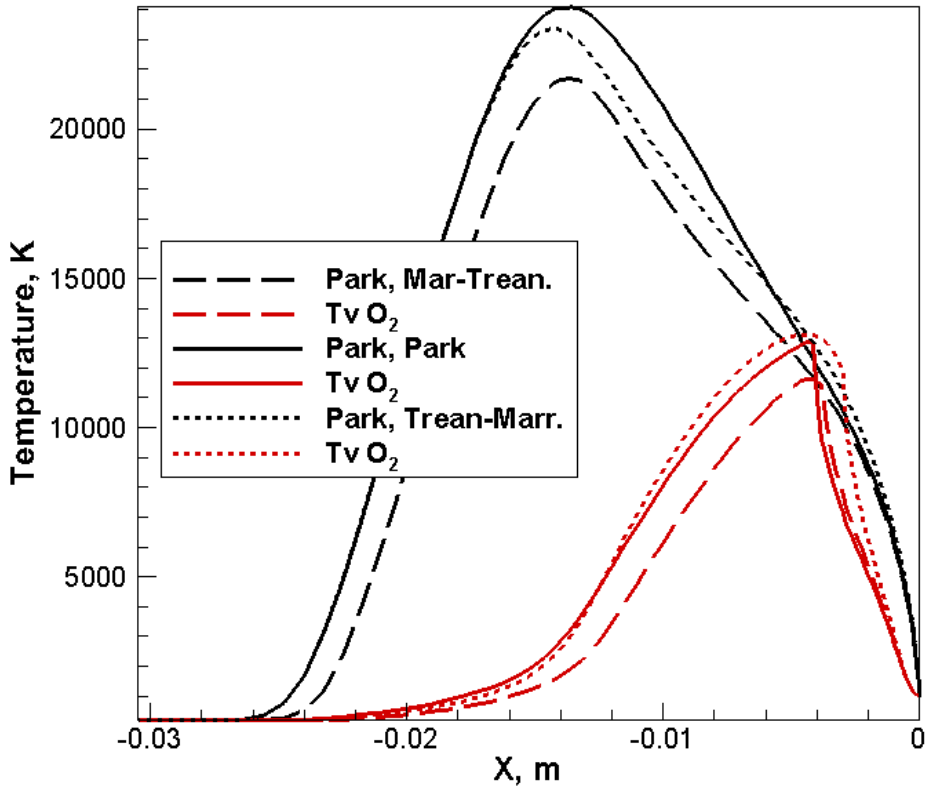

Fig. 4.13: Vibrational temperature of oxygen, K, altitude of 81 km

ature model the vibrational relaxation phenomenon is governed by the particular chemical mechanism, responsible for the reactive source term, model of vibrational - vibrational relaxation, model of vibrational - translational relaxation, reflected in Q_{vT} and the model of the source and sink of vibrational energy due to the recombination and depletion. The vibrational-vibrational relaxation is considered to be negligible in present work. The last term in Eq. (2.12) is given by Eq. (2.15), if not stated explicitly. The contribution of these terms is given in Fig. 4.14 for Dunn and Kang's model and in Fig. 4.15 for Park's model. The loss of thermal energy due to the chemical reactions in shock layer is shown by solid black curve. Present kinetic mechanisms demonstrate a factor of two difference in the absolute value of energy taken from the flow to partially dissociate and ionize the gas flow. In the vicinity of the surface due to recombination of atoms and ions (super-catalytic boundary

conditions is imposed) the chemical energy loss changes sign because of recombination.

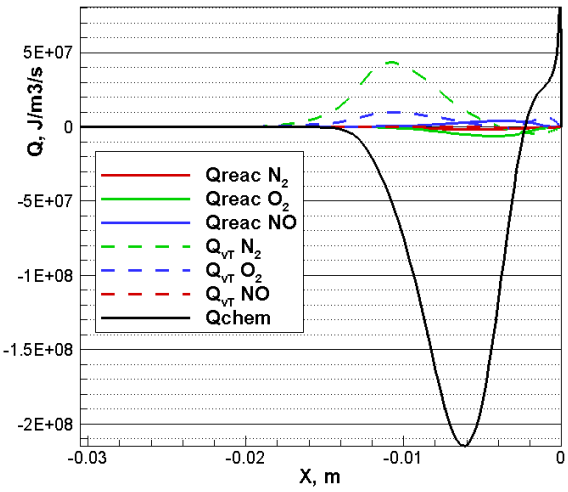

Fig. 4.14: Vibrational energy terms, Dunn and Kang model, 81 km

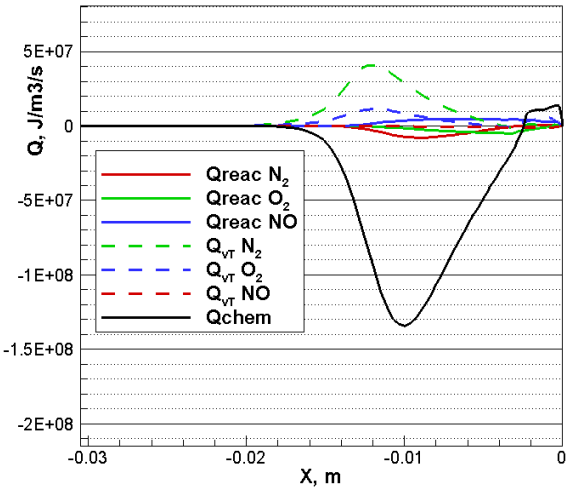

Fig. 4.15: Vibrational energy terms, Park model, 81 km

The source term describing the relaxation with the translational degree of freedom seems imperceptibly influenced by the particular chemical mechanism. As it is expected, the largest contribution is by nitrogen molecule since it has the greatest concentration among all molecular species throughout the entire shock layer. The contribution of reactive source term due to depletion and generation of molecules is dependent on the kinetic mechanism in a stronger way. However, the contribution of term Eq. (2.15) has the secondary importance compared to the term of the vibrational-translational relaxation mechanism.

To study the advantages of the three-temperature model T_{tr}-T_v-T_e over the two-temperature model T_{tr}-T_v a calculation by the assumption of chemical and thermodynamical nonequilibrium has been performed. The most obvious non-equilibrium point of trajectory at altitude 81 km is modeled. The electron-electronic temperature, vibrational temperature of N_2 and translational temperature are computed and compared with the analogous quantities of

the two-temperature model in Fig. 4.17.

Both calculations use the preferential dissociation model with $U = D/6R$ and Park's kinetic mechanism. As one can see, the individual equation for the electron energy has no visible influence on the translational temperature profile, which is governed primarily by specified rates of chemical reactions and, to a lesser extend, by the balance of the vibrational energy. This is confirmed by identical behavior of translational temperature shown by the solid black curve and circular symbols in Fig. 4.17. The maximal contribution of relaxation mechanism between free electrons and heavy particles, shown by the red curve in Fig. 4.16 is well below heat loss due to the chemical reaction in Fig. 4.15 which is of an order of 10^8 J/m^3/s.

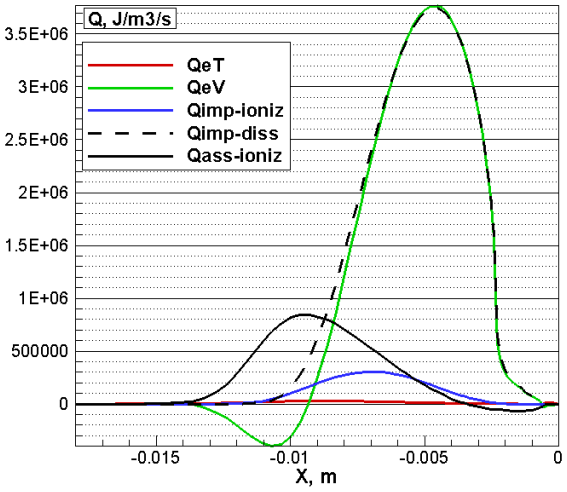

Fig. 4.16: Contribution of RHS terms in equation of free electron energy, altitude of 81 km

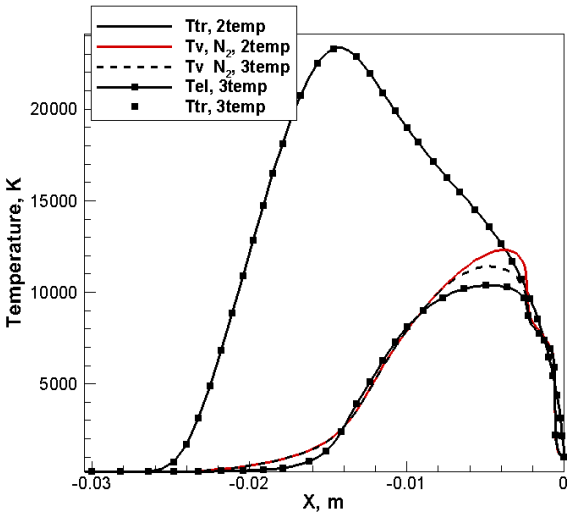

Fig. 4.17: T, T$_v$ of N$_2$ and T_e, altitude of 81 km

However, the electron temperature is different from the vibrational temperature of N$_2$. The difference is nearly 1500 - 2000 K in the region where electron-vibrational relaxation reaches the peak. Individual balance of electron energy leads to the cooling of vibrational

temperature of N_2 nearly by 1000 K and delays the excitation of vibrational mode immediately behind the shock front. The electron temperature generally follows Tv N_2 because of the important mechanism of eV relaxation. The accurate balance of electron energy can improve the accuracy for further calculations of radiation properties because the photon emission in electronic transitions in atoms and molecules is mostly governed by the electron-electronic temperature. It is worthwhile to note, that the correct balance of electron energy slightly changes the species composition and the free electron concentration toward a better agreement with the experimental data, as it is shown later.

The conditions at the altitude of 71 km possess a significant thermal non-equilibrium in the molecules excitation as well as at a higher density of the flow in comparison with the altitude of 81 km. Translational temperature for this point is presented in Fig. 4.18 and the change in the calculated electron temperature by two- and three-temperature models is shown in Fig. 4.19. The Dunn and Kang chemical model gives the smallest standoff distance as it was also observed in (Surzhikov, 2008). The difference between T_v N_2 and T_e has a small effect on translational temperature, given by Park chemical mechanism and is shown by the blue solid curve and symbols in Fig. 4.18, respectively. However the vibrational temperature of nitrogen is significantly affected by N_2-e^- energy exchange as it can be seen in Fig. 4.19. This type of energy exchange leads to the cooling of vibrational temperature by 2000-3000 K in the relaxation zone. The change of nitrogen vibrational temperature is more significant at the altitude of 71 km than at the altitude of 81 km, as it can be seen in Fig. 4.17, which can be explained by the higher degree of ionization at the altitude of 71 km, and, as it follows, the higher electron number density.

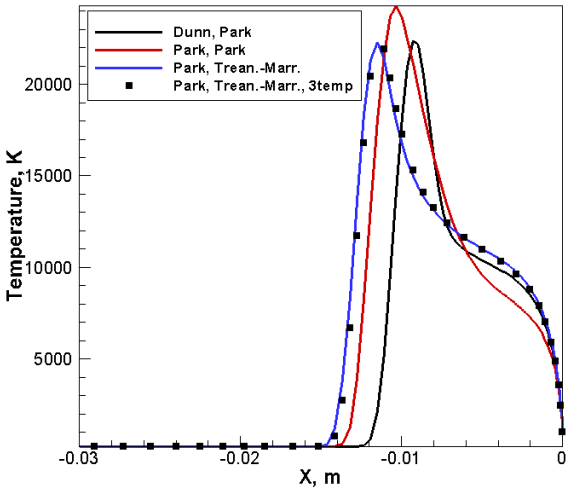

Fig. 4.18: Translational temperature, K, 71 km

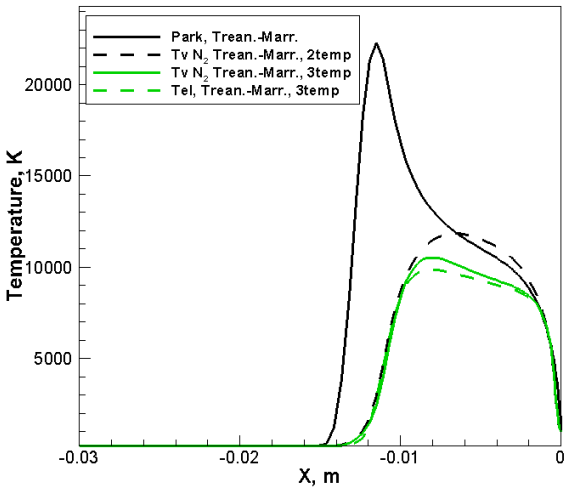

Fig. 4.19: T, T_v of N_2 and T_e , K, 71 km

Calculations by the three-temperature model are also performed in case of the highly energetic flow field at altitude of 61 km. Temperature profiles are shown in Fig. 4.21. The black and solid lines correspond to the cases of two- and three-temperature models, respectively. In both cases Park's kinetic mechanism and model of preferential dissociation with $U = D/6R$ are adopted.

The implementation of the equation for the electron energy reduces the vibrational temperature of nitrogen via the eV relaxation mechanism by 1500 - 2000 K in the relaxation zone. Since the flow at altitude of 61 km is closer to equilibrium from thermodynamic point of view rather than the flow at altitude of 81 km, the deviation of electron temperature from vibrational temperature N_2 is less, as it can be seen in Fig. 4.16. Indeed, the contribution of Q_{ev} relaxation for 61 km altitude is nearly 5x10^8 J/m^3/s, as it follows from Fig. 4.20, while for 81 km Q_{ev} is just 3.5x10^6 J/m^3/s.

Another interesting phenomenon is that the non-equilibrium excitation of free electrons eliminates the overshoot of nitrogen vibrational temperature over the translational

temperature. As it is shown in Fig. 4.20 the initial excitation of vibrational degree of freedom is immediately behind the shock front and entirely governed by translational-vibrational exchange mechanism, shown by the green dashed curve. However, as soon as vT-relaxation is completed, the ev-relaxation becomes dominant for vibrational energy distribution.

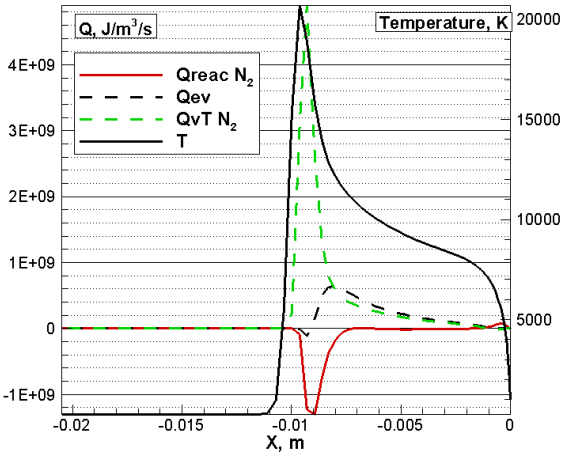

Fig. 4.20: Balance of vibrational energy, altitude 61 km

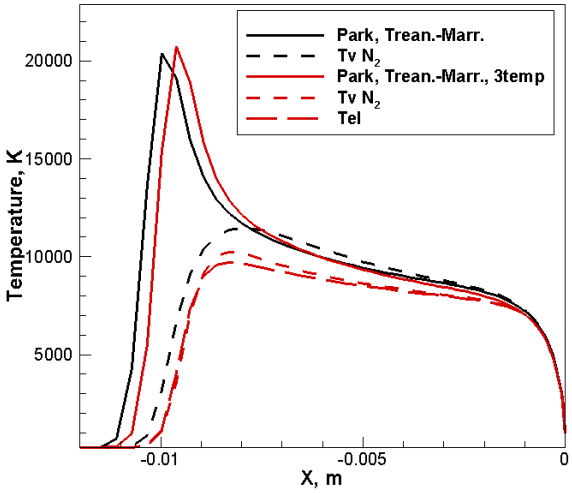

Fig. 4.21: Translational and internal temperature for two- and three-temperature models, altitude 61 km

At last, the contribution of the reactive term, responsible for depletion and generation of molecules of N_2 seems unimportant throughout the entire shock layer and relaxation zone except the region in the vicinity of the solid boundary. The gain of energy due to the recombination of nitrogen atoms near the wall is as high as 10^8 J/m^3/s (Fig. 4.20), while the impact of the rest of the mechanisms of relaxation is small.

The study of the translational and vibrational temperature profiles using other models of non-equilibrium dissociation has been proposed in literature (Losev et al., 1995; Macheret and Fridman, 1994). It is necessary to understand the uncertainty by the non-

equilibrium dissociation of molecular species when the comparison with experimental data is adopted as the validation of the entire approach.

Translational and vibrational temperature and electron number density computed by four different models of non-equilibrium dissociation are shown in Fig. 4.22 and 4.23, respectively. Calculations are performed for the altitude of 81 km, and non-catalytic boundary condition using the two-temperature T-T$_v$ model of energy distribution between internal modes. The β-model by Losev (Losev et al., 1995), Macheret-Fridman (Macheret and Fridman, 1994) model of impulsive collisions and preferential dissociation model by Treanor and Marrone (Marrone and Treanor, 1963) with $U = \infty$ and $U = D/6R$ are used. For the latter an additional limitation on partition function is imposed for cases where T$_v$ > T.

The vibrational partition function of harmonic oscillator is computed as

$$Q_v\left(T\right) = \frac{1 - exp\left(-D_{v,diss}/T\right)}{1 - exp\left(-\theta_v/T\right)}.$$

In case of the overshoot of vibrational temperature, the partition function Q_v for specific temperature T$_f$ and U, as denoted in the work by Marrone and Treanor (1963) equals to $D_{v,diss}/\theta_v$, as it is implied in the work by Surzhikov and Shang (2011).

The difference in translational temperature between two investigated models by Treanor and Marrone ($U = \infty$ and $U = D/6R$) is relatively insignificant as it can be seen from comparison of red and blue solid curves in Fig. 4.22. The model by Losev leads to a significant cooling at shock front and relaxation zone up to a maximum value of 3000 K. The impact on vibrational temperature generated by the model of non-equilibrium dissociation

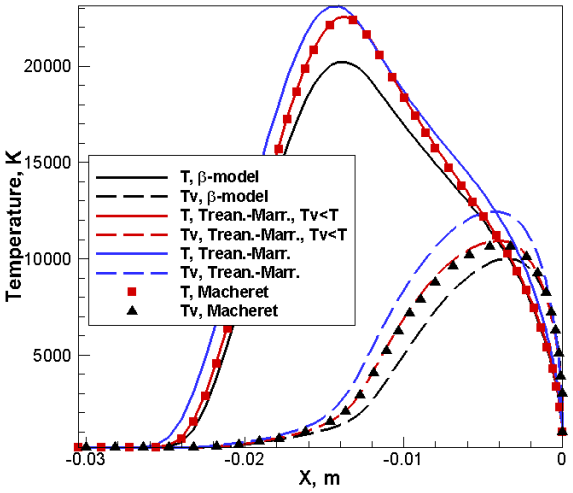

Fig. 4.22: T and T_v O_2, altitude of 81 km

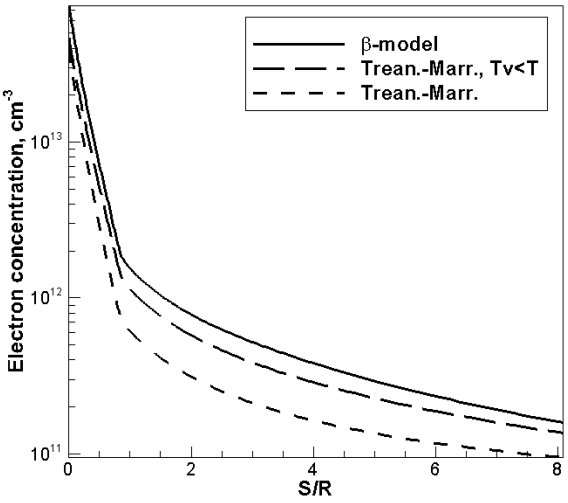

Fig. 4.23: Critical electron number density, altitude of 81 km

is more significant. The Losev model predicts the lowest temperature for all molecular species. The vibrational temperature for oxygen is shown in Fig. 4.22.

Macheret-Fridman's model can be presented as Treanor-Marrone model with the empirical parameter dependent on translational and vibrational temperatures as well as the mass of colliding particles. In other words, it is shown in (Fridman, 2008) that the empirical parameter U is dependent on effective temperature T_{eff}:

$$T_{eff} = \alpha T + (1 - \alpha)\, T_v,$$

where the parameter α is defined as $\alpha = (m/(m + M))^2$, m is the mass of atom in the dissociating molecule, M is the mass of the colliding particle. The empirical parameter U is given by:

$$U = \frac{T T_{eff}}{(T - T_v)\,(1 - \alpha)\,.} \tag{4.4}$$

Taking into account Eq. (4.4), one may conclude that at equilibrium conditions, when $T = T_v$, empirical parameter $U \rightarrow \infty$, yielding to the equal probability of dissociation from all vibrational levels. When $T \gg T_v$, i.e. under strong non-equilibrium conditions immediately behind the shock front, $U \approx \alpha T / (1 - \alpha)$.

It was stated in (Fridman, 2008) that empirical parameter U may significantly vary under non-equilibrium conditions. Indeed, in present work the range of change starts from approximately 1/5 of T and spans to infinity. However, the dramatic change just slightly affected the vibrational temperature of oxygen, as shown in Fig. 4.22 and the translational temperature is essentially the same as for the entire shock. In other words, it is shown that the second model by Treanor-Marrone with finite value of U demonstrates the behavior of vibrational temperature past the shock that can be reproduced by the Macheret-Fridman's model.

The electron number density demonstrates a high sensitivity to the choice of non-equilibrium model, as one can see, in Fig. 4.23. The highest number density of free electrons is given by the model of Losev. At stagnation region the difference is nearly two folds with respect to Treanor-Marrone model and it is nearly constant along the entire flow path. The large discrepancy indicates that the actual effects of non-equilibrium dissociation significantly impact the thermo-chemical composition. The generated results should be exercised with caution while attempting to validate a particular computational model.

4.4.3 Heating rates

Conductive heating rates on the surface of RAM-C II vehicle is studied for chemical mechanism by Park and Dunn and Kang. The heating rates at the altitude of 81 km are presented in Fig. 4.24. Two boundary conditions, representing full recombination of atoms and ions as well as non-catalytic surface demonstrate nearly a 10 W/cm^2 difference at the stagnation point point. As it is expected, the non-catalytic boundary condition leads to the lower value of flux.

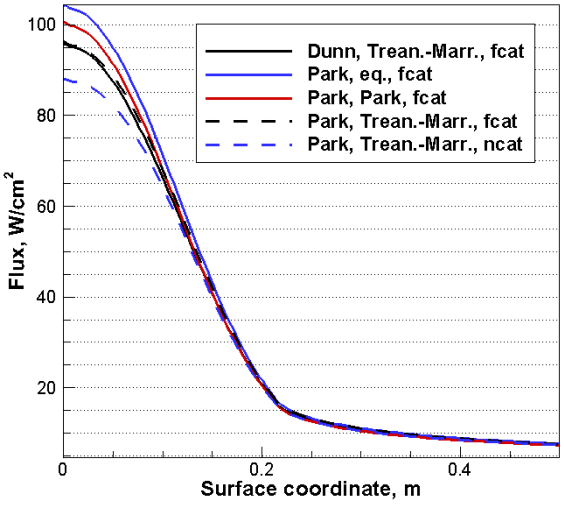

Fig. 4.24: Heating rates, altitude of 81 km

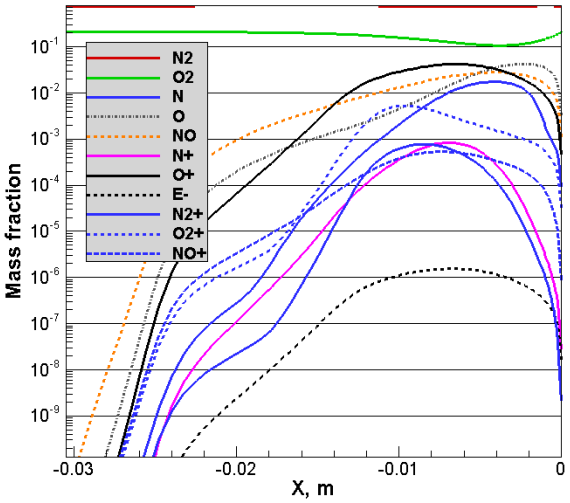

Fig. 4.25: Species mass fraction, Dunn and Kang model, altitude of 81 km

Another result derived from Fig. 4.24 is a good agreement in heating rate for the entire surface between two different kinetic mechanisms. Both Dunn and Kang and Park kinetic mechanisms with the model of preferential dissociation indicate the flux as high as 95 W/cm^2 at the stagnation point with less than two percent difference. At the same time, the difference in mechanisms of dissociation at the same kinetic model gives 10

% difference in peak value. There are a number of papers (see, for example, (Gnoffo, 1986; Surzhikov, 2008)) that demonstrates significant difference in species composition generated by different mechanisms used in present work. Indeed, when the species profile by Dunn and Kang mechanism in Fig. 4.25 is compared to the results by Park model in Fig. 4.11, one can observe that the difference is also persistent.

The most intense heating point on the trajectory occurs at the altitude of 61 km. The distributions of heating rate for all computed cases are presented in Fig. 4.26. As in the case of 81 km, the calculation with finite rate chemistry and equilibrium thermodynamic model, depicted with dashed black line, gives the highest heating rate of 310 W/cm^2. Dunn and Kang's as well as Park's chemical mechanism with preferential model of dissociation are in less agreement than they are in the case of 81 km, showing a difference of 30 W/cm^2. The model accounting for the individual conservation equation of electron energy reduces the stagnation heating rate by 20 W/cm^2. The overall scatter of stagnation heating rates is within 20 % of the highest computed value, which is considered as an acceptable difference.

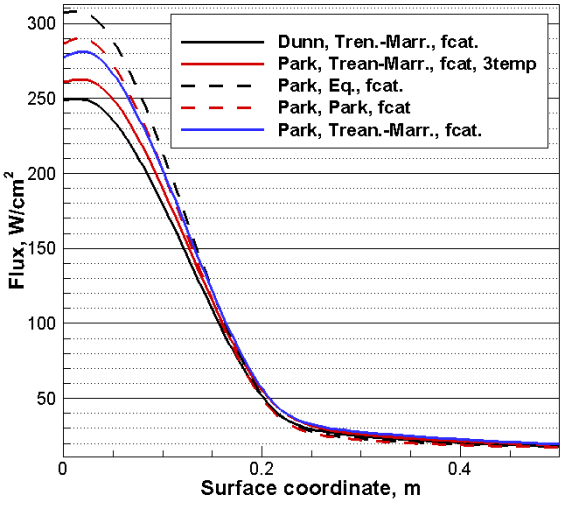

Fig. 4.26: Heating rate, altitude of 61 km

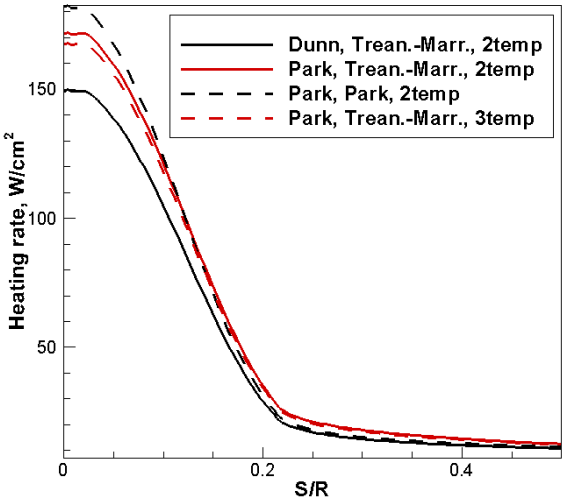

Fig. 4.27: Heating rate, altitude of 71 km

Heating rates along all trajectory points studied in present work are summarized in Table 4.1. This data reflects the fact that at higher altitudes of trajectory the space vehicle experiences less heating in comparison to the flight in dense and highly energetic flow. The difference between chemical models is larger at low altitudes of the trajectory. First of all it can be explained by the impact that the chemical model introduces in the flow. At higher altitudes dissociation of molecules is less intensive and chemical mechanism perturbs the initial composition in a less degree compared to the flow field in the dense layers of atmosphere. Second, the degree of ionization in rarefied flows, generated by re-entry spacecraft, is much smaller, as it can be seen in Fig. 4.28, 4.30 and 4.31.

Altitude/Model	Park	Dunn and Kang
61 km	278	249
71 km	172	149
81 km	96	95

Table 4.1: Stagnation heat flux, W/cm^2, preferential model of dissociation, two-temperature thermodynamic model, super-catalytic boundary conditions

The comparison of stagnation heat flux at the altitude of 71 km with the other theoretical data is presented in Table 4.2. The dispersion of reported data is primarily due to the imposed boundary condition for species on the wall and kinetic mechanisms. The work Tchuen and Zeitoun (2009) indicates that Dunn and Kang's mechanism gives lower heating rate than Park's mechanism. This result is confirmed by present work at altitudes of 61 and 71 km in Table 4.1.

The work Walpot (2002) demonstrates a good agreement between Park and Dunn and

Reference	Chemical model	Heat flux, W/cm^2	Note
Tchuen and Zeitoun (2009)	Dunn and Kang	58	11 species non-catalytic BC, Park model
Tchuen and Zeitoun (2009)	Park	102	same as previous
Walpot (2002)	Park	218	11 sp., catalytic BC
Walpot (2002)	Park	85	11 sp., non-catalytic BC
Walpot (2002)	Dunn and Kang	220	11 sp., catalytic BC
Walpot (2002)	Dunn and Kang	95	11 sp., non-catalytic BC
Soubrié et al. (2006)	Park	96	11 sp.
Candler and MacCormack (1991)	Park and Wray	250	7 sp., estimated from St number
Present work	Dunn and Kang	149	11 sp., catalytic BC
Present work	Park	172	same as previous

Table 4.2: Stagnation heat flux, altitude of 71 km

Kang chemical mechanisms. The estimation by Candler and MacCormack (1991), is obtained for a reduced kinetic mechanism using the Stanton number. In overall, results of present work fall in range of generally accepted results and follow the conclusions made by other authors regarding influence of kinetic mechanism and boundary conditions. Unfortunately, heating rates corresponding to other altitudes are rarely reported in literature to perform additional comparison.

4.4.4 Validation against experiment

This section consists of two parts. The data obtained by microwave reflectometers and Langmuir probe is used. Computational results obtained in present work are brought together to understand the influence of model of non-equilibrium dissociation, chemical mechanism and T_{tr}-T_v-T_e and T_{tr}-T_v models. Theoretical and experimental results are given in particles/cm^3 against normalized axial coordinate x/R, where R = 0.1524 m and x

is measured in meters.

First, the data collected from reflectometers measurements is analyzed. Since the data is available for the entire path of flow field the study of critical electron number density may serve as a classical tool of validation for the chemical mechanism and thermodynamic model. However the influence of boundary effect is not available by this approach. It was reported previously (Surzhikov, 2014; Walpot, 2002) that the imposed boundary condition for species has a little effect on the critical electron number density, located within the relaxation zone. The second part of the section is devoted to the comparison of spatial concentration of free electrons at the afterbody of the vehicle with the Langmuir probe data.

Reflectometer data

Four reflectometers that are able to measure the number density of free electrons in a partially ionized gas were installed along the surface of experiment RAM-C II (Grantham, 1970). The location of reflectometers is given in Grantham (1970) as the ratio of axial coordinate to the radius of hemisphere. Electron number density obtained from the present simulation at the altitude of 81 km is given in Fig. 4.28. Experimental data is presented by square symbols. All curves correspond to the chemical model of Park and super-catalytic boundary condition if not stated specifically. Solid curve is the finite rate chemistry calculations, no model of non-equilibrium dissociation is implemented. Short dashed line is the Park's model of non-preferential dissociation, two temperature model. The long dashed and solid lines with circular symbols correspond to the preferential dissociation model, $U = D/6R$, two and three temperature models, respectively. Solid line with triangular

symbols depicts the preferential dissociation model with non-catalytic boundary condition.

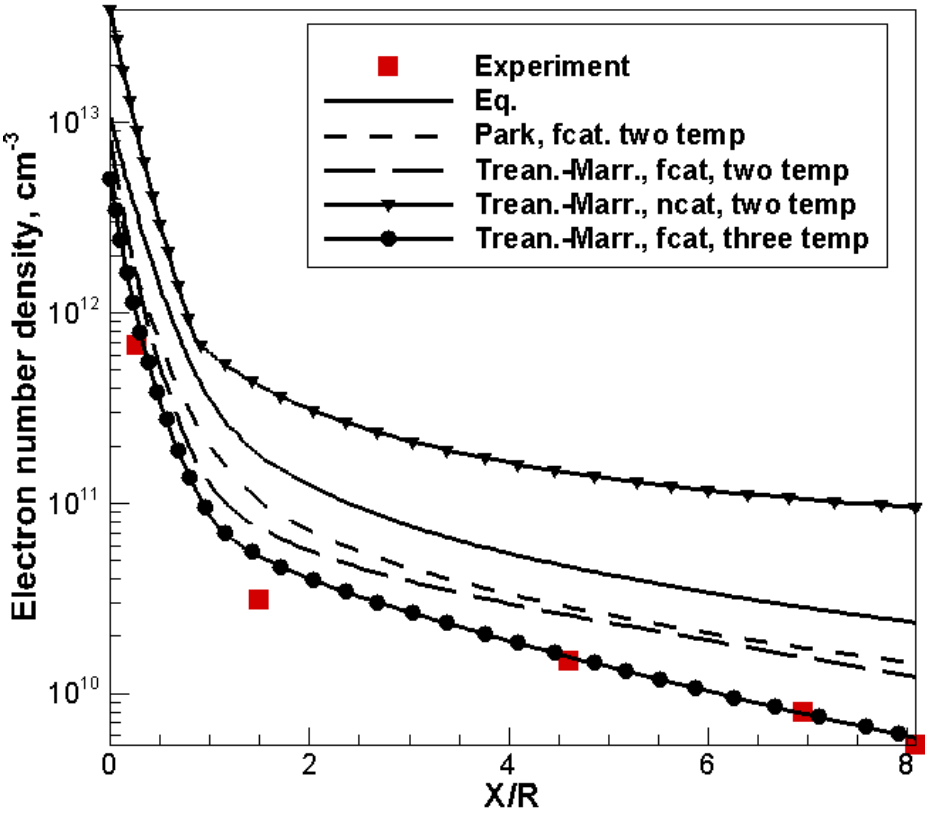

Fig. 4.28: Electron number density, altitude of 81 km

One can see that non-catalytic boundary condition overestimates the electron concentration by order of one magnitude, as it was previously stated in Shang et al. (2013). The calculation by the assumption of thermodynamically equilibrium gas also overestimates the electron number density. The subsequent refinement for non-equilibrium dissociation from the empirical Park's model to the model of equal probability dissociation and preferential dissociation with $U = D/6R$ brings the computed concentration of electron gas in good agreement with the experimental data. One can conclude that at low-energetic and strong non-equilibrium flow the physical model of preferential dissociation is more accurate than a single governing temperature.

The implementation of an individual equation for conservation of the electron energy changes the electron number density by 20 % at the nose of vehicle. Also changes are observed for the entire flow path along the surface. In all, the matching with experiment for three-temperature model is good, however one should use this result with caution. Although the matching with experiment for Langmuir probe along the afterbody of vehicle is nearly perfect, it should be kept in mind that there are large uncertainties of data obtained by probe measurements (see, for example, Fig. 4.34, (Vlasov et al., 1997) and (Boyd, 2007)).

Comparison of the multi-temperature approach with other theoretical effort is presented in Fig. 4.29. Due to the high degree of non-equilibrium conditions there were only few calculations carried out previously for these points of trajectory. One of the earliest work that applied multi-temperature model is by Candler and MacCormack (1991), the result is shown by black dashed curve in Fig. 4.29. More recent results by Vlasov et al. (1997) demonstrate the reasonable prediction with the Langmuir probe data, however the validation against reflectometers was not reported. The work Surzhikov (2014) also demonstrates good agreement with reflectometers data, however comparison is not included here.

It seems that the earliest work attempted to reproduce data is by Bird (1989) and it is based on Monte-Carlo principles. The underestimation of experimental data is found most probably to be due to the insufficient computational capabilities at that time. A more recent work by Boyd (2007) applies both models of total collisional energy and vibrationally favored dissociation (black and red solid curves in Fig. 4.29). It was demonstrated that the experimental data falls in the region formed by the adopted chemical model for the DSMC approach.

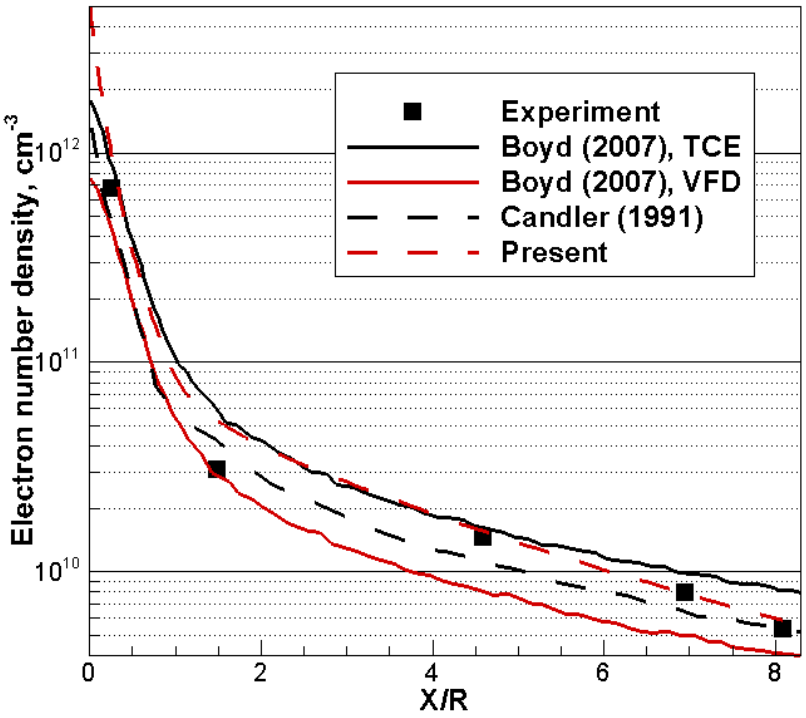

Fig. 4.29: Electron number density in comparison with Boyd, 2007 and Candler and MacCormack, 1991

The general conclusion that follows from Fig. 4.29 is that both DSMC and multi-temperature models are capable of describing the chemical composition behind the shock wave at the altitude of 81 km. In the case of Monte-Carlo simulation the dispersion of results is an important factor for the overall accuracy, while the accuracy of the approach based on Navier-Stoke equations is more likely to depend on the combination and uncertainty of various incorporated models.

The critical electron number density, computed at the altitude of 71 km is shown in Fig. 4.30. As in the case of 61 km, the Park's non-equilibrium model gives the greatest deviation of electron number density compared to the experimental data and models of Treanor-Marrone. Both calculations that are using preferential model of dissociation demonstrate a very good agreement with experiment. The more complicated three-temperature model

brings results closer to experiment than the two-temperature model, which indicates the general validity of the individual electron energy equation adopted in the present work.

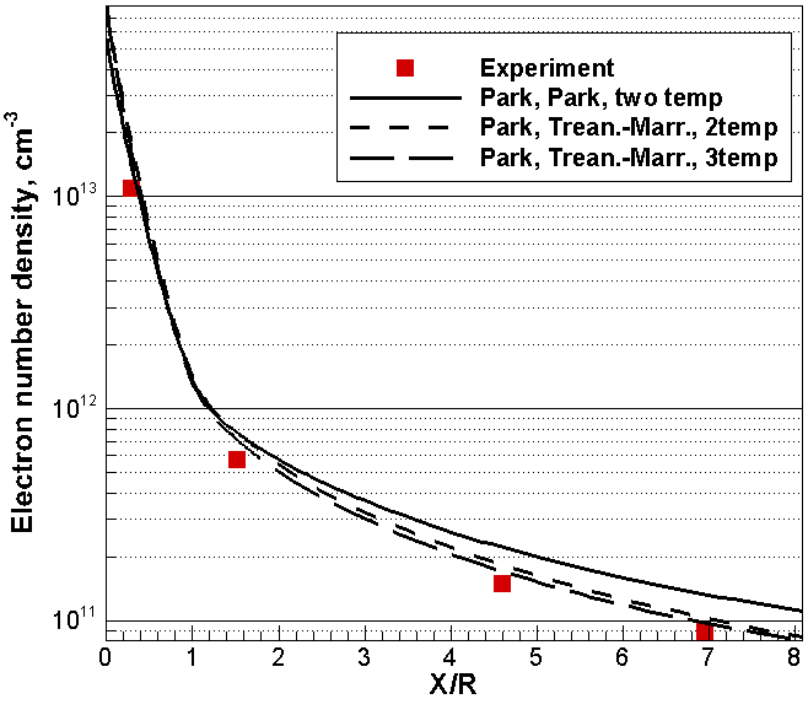

Fig. 4.30: Electron number density, altitude of 71 km

Similar observations can be made for results obtained for the altitude of 61 km shown in Fig. 4.31. The matching with the experimental results is less successful here, however the agreement between results is still satisfactory. Calculations assuming thermodynamically equilibrium distribution between internal DOF give an overestimated number density. However, the difference between equilibrium and non-equilibrium calculations is less than what it is for the altitude of 81 km, as shown in Fig. 4.28. The difference between Treanor-Marrone's and Park's model of dissociation at this altitude is much less pronounced, compared to the same curves in Fig. 4.30 and 4.28. One of the possible explanations is that for high-energetic conditions the "ladder climbing" process is not dominant for the dissociation

to occur.

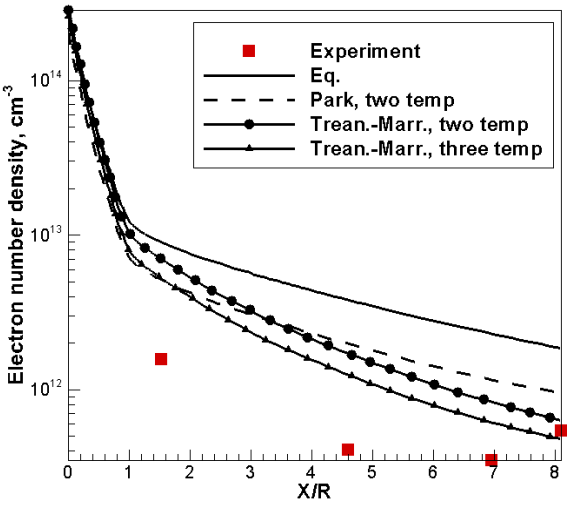

Fig. 4.31: Electron number density, present work, altitude of 61 km

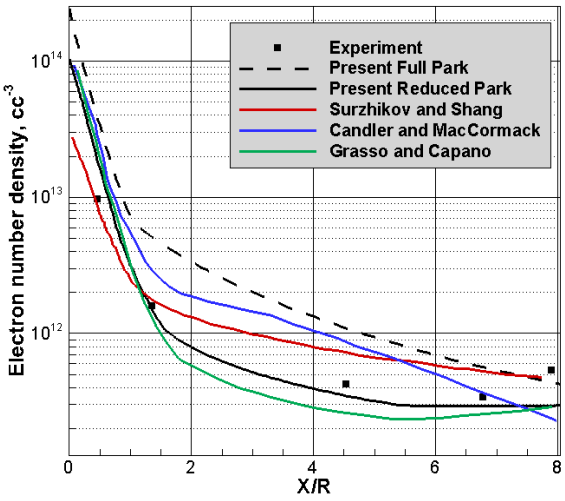

Fig. 4.32: Electron number density, comparison with available data, altitude of 61 km

Comparison of present results with theoretical data available from other resources is shown in Fig. 4.32. Additional calculation have been performed using a reduced chemical model with 7 species N_2, O_2, N, O, NO, NO^+,e^- and 18 reactions. Only reactions of dissociation involving major species, exchange reactions involving NO and single associative ionization reaction between N and O are retained. Both green solid and dashed black curves corresponding to the 7- and 11-species sets of reactions in Fig. 4.32 agree with other theoretical results. It is worthwhile to note that the 7-species mechanism demonstrates a significant lower electron number density and a better agreement with experimental data. It is important to note, that data by Candler and MacCormack (1991); Grasso and Capano (1995); Shang et al. (2012) is obtained by the 7-species mechanism. In this sense, the agreement of present results with data by other authors is good.

The significant difference in the electron number density also indicates that in the low-

altitude flow regime the associative ionization between N and O is not the only source of electrons behind the shock front. The importance of other types of associative ionization can be explained by the high degree of dissociation for the altitude of 61 km and, thus, high forward reaction rates for pairs $N + N$ and $O + O$.

Langmuir probe data

It is interesting to compare the spatial distribution of the electron number density measured by Langmuir probe with the theoretical prediction. Very few works have previously provided spatial distribution of electron number density at the location of Langmuir probe. The theoretical prediction at the altitude of 71 km was given by Farbar et al. (2011); Vlasov et al. (1997). A similar prediction for the altitude of 81 km was presented only by Boyd (2007) using DSMC and Vlasov et al. (1997). In present work the spatial distribution of electron number density is reported for both altitudes of 71 and 81 km that are most interesting from the non-equilibrium thermodynamics point of view. The present data is compared with experimental data as well as with the other theoretical works for two models of non-equilibrium dissociation by Park and Treanor-Marrone. The comparison is presented in Fig. 4.33 and 4.34.

The results, obtained in Farbar et al. (2011) correspond to the model of Park with ions fully recombined on the surface and are shown by solid line in Fig. 4.33. Present results are shown with short and long dashed curves for Park and Treanor-Marrone models in Fig. 4.33. The results by Vlasov were obtained by Eq. (4.2) and are shown with the solid curve with symbols.

One can see that results by Farbar et al. are in between present results which demon-

strate the high sensitivity to the model of non-equilibrium dissociation at the altitude of 71 km. In the vicinity of surface the electron number density varies from 2x10^{10} cm^{-3} to 3x10^{10} cm^{-3} which is smaller than the uncertainty, introduced by the model of non-equilibrium dissociation.

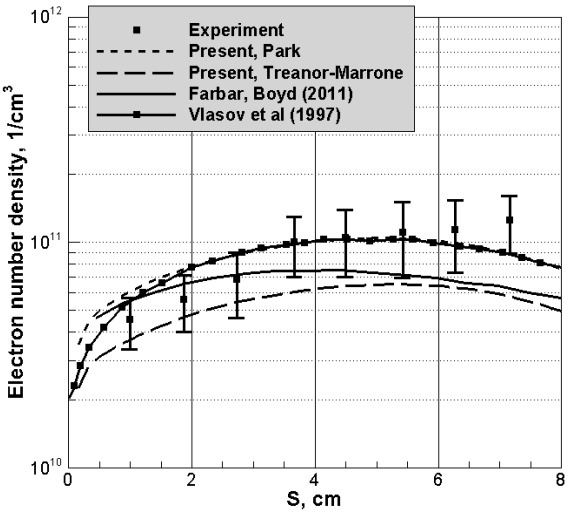

Fig. 4.33: Electron number density, cm^{-3}, Langmuir probe, altitude of 71 km

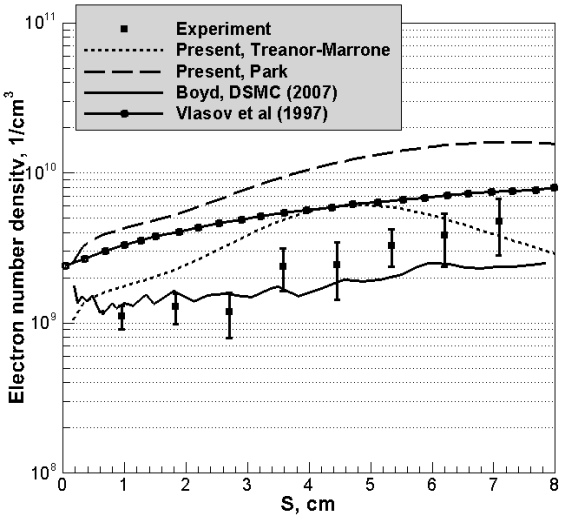

Fig. 4.34: Electron number density, cm^{-3}, Langmuir probe, altitude of 81 km

In general, the results by Treanor-Marrone model are in good agreement with the experiment in the vicinity of the surface, as it can be observed from Fig. 4.33. This is also confirmed by comparison with the reflectometer data. At the distance from the surface the Park model describes experimental data better. However, it can be seen, that the accurate treatment of boundary conditions for charged particles by Vlasov et al. (1997) allows a reasonable agreement with experiment near the surface as well as in the wake flow.

The Park model overestimates data by Langmuir probe for the altitude of 81 km. This result is observed not only for spatial distribution shown in Fig. 4.34 but also for reflectometer data on Fig. 4.28. The model by Treanor-Marrone shows better agreement for the

entire length of Langmuir probe. The application of more accurate boundary conditions based on finite size of Knudsen length by Vlasov et al. (1997) is in the range of the uncertainty due to the model of non-equilibrium dissociation. The DSMC approach seems to be more viable and accurate, since the application of Navier-Stokes equations might be marginal in rarefied flows.

4.5 Conclusion

Three points of RAM-C II space vehicle trajectory are investigated on the sensitivity to the chemical reaction data set, non-equilibrium dissociation model and thermodynamic model of energy distribution between internal degrees of freedom.

It is found that for the studied flight conditions at altitudes of 61, 71 and 81 km the three-temperature model demonstrates a better agreement with experimental data than the two-temperature model. The decrease of nitrogen vibrational temperature has been found to be due to the electron-vibrational relaxation mechanism and the delay of vibrational mode excitation when the electron-electronic balance of energy is accounted separately from the conservation equation for the vibration energy.

The phenomenon of the non-equilibrium dissociation has a significant impact on the vibrational temperature and chemical composition and, to a lesser extend, on the translational temperature behind the shock wave. Among all studied models of the non-equilibrium dissociation the preferential dissociation model by Treanor and Marrone with the empirical parameter $U = D/6R$ reproduces the best agreement with the experimental data. The comparison of Treanor-Marrone model with Park model of non-preferential dissociation re-

veals a significant difference in the dissociation degree of molecular oxygen, especially for conditions corresponding to the flight at high altitudes. The implementation of Macheret-Fridman model insignificantly affects the distribution of energy between internal modes in comparison with the model of Marrone-Treanor.

The spatial distribution of electron concentration is studied by means of the multi-temperature approach. It is found that the uncertainty due to the model of non-equilibrium dissociation and chemical reaction data set is greater that due to the boundary condition applied for species concentration. The experimental data is reproduced the best when the fully catalytic boundary condition is specified on surface of the RAM-C II probe. An uncertainty due to the finite size of Knudsen layer has less effect on spatial distribution of electron gas than the model of non-equilibrium dissociation.

The electron number density calculated by the Park's chemical reaction set, model of the preferential dissociation and the three-temperature thermodynamic model demonstrates a reasonable agreement with the experimental data produced by reflectometers and with other theoretical works. The spatial distribution of electron number density at the location of Langmuir probe is found to be in good agreement with the experimental results. As a matter of fact, the Treanor-Marrone model is found to provide better agreement with the experiment at the altitude of 81 km, while both models by Park and Treanor-Marrone show a satisfactory agreement with the experiment at the altitude of 71 km.

Heating rates are investigated for the range of the altitude of 61 - 81 km. It has been found that the difference between Park and Dunn and Kang chemical mechanism is increasing toward the lower altitudes of trajectory. Namely, for the altitude of 81 km the heating rates provided by two different chemical mechanisms are in good agreement. At the alti-

tude of 61 km the difference is nearly 20 %. The heating rates are higher at lower altitudes, reaching a value nearly three times more at the altitude of 61 km than at the altitude of 81 km.

5. RAY TRACING METHOD FOR RADIATION TRANSFER

5.1 Introduction

The ray tracing method (RTM), proposed for the aerospace applications in the work Surzhikov (2004a), is applied to calculate radiation flux density in weakly ionized plasma generated by the RAM-C II re-entry (Grantham, 1970). The application of RTM is attractive because of its asymptotic accuracy when sufficient number of tracing rays is used and solution of RTE along each ray is accurate. The basic principle of RTM naturally describes the propagation of radiation quantum by emitting a number of rays to discretize the media with active radiation transitions.

The disadvantages of RTM is also well known. The ray tracing method provides the solution only at a point of the space. In other words, the integration of radiation intensity over the entire solid angle is required to obtain the characteristics of radiation field at every given location. This is applicable to radiation flux density as well as volume density of radiation energy. Although, in theory, RTM is applicable to determine the volumetric characteristic of radiation field, it is usually applied only to calculate flux density on the surface. The cost of RTM is due to the numerical solution of Eq. (2.81) along each tracing ray and by the projection of optical properties from the gasdynamic grid on the tracing ray.

In the present work the problem of the efficiency is approached in two ways. The integration by means of a quadrature formula is applied to improve accuracy of the solution

along tracing rays. Particularly, the Gauss-Lobatto (GL) quadrature is investigated. The distinct advantage of GL quadrature is the clustering integration points to the edges of the segment on a tracing ray. The difference between Gauss-Lobatto and Gauss quadratures consists of the fixed contribution of endpoints of the tracing ray into solution of Eq. (2.81). This fact reduces the accuracy of integration by two compared to Gauss quadrature. However, since the active radiation transitions occur at the ends of integration interval, corresponding to the shock location and the surface, this clustering pattern by GL quadrature is substantial.

In theory, GL quadrature generates a 2N-3–order accurate solution at a number of integration points equal to N, while the conventional trapezoid rule, previously applied in RTM (Surzhikov, 2004b) to calculate RTE solution, Eq. (2.81), is only second order accurate. The reduction of the necessary number of points on the tracing ray will possibly make the RTM less expensive by maintaining the same accuracy. The challenge of the present research is to understand whether this holds when RTM is applied to the flow with shock and when the database of thermodynamic and optical properties is available only at a discrete number of grid points, given by the preceding solution of Navier-Stokes equations.

5.2 Nearest Neighbor Search

In order to determine optical properties on the tracing ray, the thermodynamic state and gas composition must be obtained from the solution of governing equations describing thermodynamically non-equilibrium flow field on the body-oriented system of coordinates. In present work the RTM is applied to the flow field generated by governing equations

(2.2), (2.5), (2.11), (2.12), (2.16) and (2.4). At the same time, the conventional approach of RTM consists of the emission of rays based on the surface-oriented coordinate system. The interpretation between two different systems of coordinates is tightly connected to the nearest neighbor search (NNS) procedure, where for each location on the tracing ray the nearest neighbor from the body-conformal grid is assigned. It is an optimization problem to locate the closest grid point in the metric space. This effort opens new research possibilities and brings a new level of computational performance to the multi-disciplinary modeling and radiation transfer models.

The numerical resolution and improvement of computational efficiency are built on a knowledge of grid structure and shock location. The NNS algorithm is considered for both structured and unstructured shock adapted grids. In case of structured grid the node indices that are forming the proximity containing the nearest neighbor for the current tracing ray are analyzed. This technique is referred to as a space partition search (Shang et al., 2014). Alternatively, the information on the nearest neighbor, somehow determined for the previous point on the tracing ray can be also used. This search method is referred to as the consecutive search. In case of unstructured grid the analysis of the previous nearest neighbor seems to be a more viable option since no ordered coordinate indices can be extracted from unstructured grid and application of partition search is therefore hindered.

5.2.1 Space partition search

The space partition search algorithm is developed in present work for a two-dimensional coordinate system, however the algorithm can be generalized into three-dimensional geom-

etry by implementing an additional index. Let the tracing ray **r** be emitted from the surface with the normal unity vector **n**. In order to determine the intersection of shock front with **n** and tracing ray **r** with **n** the geometric shape of the shock front must be known. Since the analytical expression is generally not available, the search of intersection is based on the information contained by the grid. The shape of the shock, captured by structured grid, can be given as a one-dimensional array that gives the relation between grid indices i and j_i. Here i is the index of grid line emanated from the surface, j is the index of grid cells along the ray i. Location of the shock is now described by the pair (i, j_i). The intersection of the ray **r** with the shock is now given as the intersection of ray **r** with the segment (i, j_i) and $(i+1, j_{i+1})$. Note, that the knowledge about the exact coordinates of intersection is unnecessary to form the radius of search.

Assume that the normal vector intersects with the shock at (i_1, j_1) and with **r** at (i_2, j_2). Then for any point on **r** the nearest neighbor is located in the area formed by the next indices: $i_{max} = max\,(i_1, i_2) + 1$, $i_{min} = min\,(i_1, i_2) - 1$, $j_{max} = max\,(j_1, j_2)$, $j_{min} = 1$. It is assumed that j index is numerated from the surface.

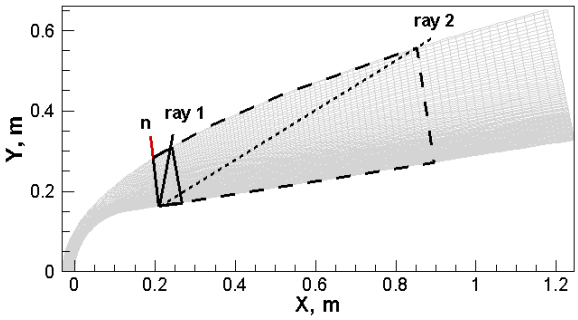

Fig. 5.1: Concept of space partition search

The efficiency of partition search algorithm is dependent on the angle between **n** and **r**. For a ray emitted close to the normal vector of the surface the search domain will be smaller than for a ray emitted in the tangential direction to the surface. This situation is reflected in Fig. 5.1. For the ray 1 the search partition is restricted by solid line. The

domain corresponding to ray 2 and bounded by dashed line is larger than the domain of ray 1 because of the different orientation of rays 1 and 2.

5.2.2 Consecutive search for structured grid

When the nearest neighbor is known for the point located in the vicinity of the point of current interest, the area of search can be built on the analysis of the location of the previous nearest neighbor. One of the special cases is the search of an approximate nearest neighbor (Arya et al., 1998). Although the radiation flux is extremely sensitive to the data used to determine gas properties, and an approximate nearest neighbor is not acceptable for the radiation transfer problem in shock layer, the key idea of the proximity based on previously obtained information is viable. As in the previous section, the two-dimensional geometry is considered. The three-dimensional generalization is straightforward by implementing an additional index.

Since the search of nearest neighbor can be performed only in a consecutive manner, i.e. only when neighbor is determined for previous point on the tracing ray, this approach is further referred to as the consecutive search. The most efficient realization of this approach is when the spacing between points on the tracing ray is equal to or less than the grid spacing in the vicinity of nearest neighbor candidate. In this case the radius of search is the index of the grid equal to unity. However even when the spacing between points on the ray is large, this approach is still assumed to give an overwhelming advantage in the performance over the brute search since the search is performed only over a number of nodes which is multiple orders of magnitude less than the overall grid dimension.

The nearest neighbor for the point (x_0, y_0) (Point 2 in Fig. 5.2) on the tracing ray Ω is searched in the vicinity of nearest neighbor (i_g, j_g) of point (x_g, y_g) (Point 1 in Fig. 5.2) along the same tracing ray. In case of a uniform grid with the step h and the distance between points on the ray d, the radius of search is $I_r = [d/h] + 1$, where brackets stand for the nearest whole number, not exceeding the argument in brackets. Then the radius of search has the boundaries of $(i_g \pm I_r, j_g \pm I_r)$.

When the grid is refined for the flow structure along one or more coordinate directions, the radius of search is adjusted for each point on the tracing ray: $I_{r,i} = [d_i/h_i] + 1$, where d_i is the distance between current and previous point on the ray, h_i is the grid step in the vicinity of (i_g, j_g). When the aspect ratio of grid cells differs from unity the radius of search can be implemented for each direction separately: $I_{r,i} = [d_{i,x}/h_{i,x}] + 1, I_{r,j} = [d_{j,y}/h_{j,y}] + 1$, where $h_{i,x}$ and $h_{i,y}$ are the size of the grid spacing along index i and j, the notations $d_{i,x}$ and $d_{i,y}$ are the projected distance of the segment (x_0, y_0) and (x_1, y_1) along the coordinate lines. The boundaries of the search radius is now given as $(i_g \pm I_r, j_g \pm I_r)$.

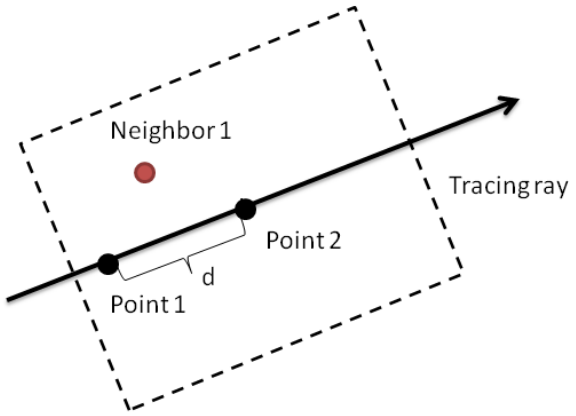

Fig. 5.2: Concept of consecutive search

5.2.3 Consecutive search for unstructured grid

The consecutive search algorithm for the unstructured domain is less straightforward than for the structured grid. The main challenge is to define the radius of search in the vicinity of the point on the tracing ray. Since the unstructured grid may have assigned gasdynamic parameters either to nodes or to cells (node-centered and cell-centered situation), the radius of search may be defined by the number of either nodes or cells. Without limiting the entire derivation of this method only the node-centered situation is considered.

Since the direct access to adjacent cells by the simple increment of index is unavailable, the candidates for the nearest neighbor are to be defined prior to the application of the ray tracing method. This information is constructed in a table form of nodes and stored once for each grid. The nearest neighbor for each node is then determined by a search over the all elements in the table.

The radius of search over the adjacent nodes determines the size of the table. The distance between points on the tracing ray should correspond to the grid points available on the path of the ray. Since the typical grid has clustered points as well as points on the tracing ray, the analysis of distance ratio is implemented as in the case of structured grid.

In order to make the application of GL quadrature on unstructured grid meaningful, the tracing ray must be terminated at the location of the shock. The shape of the shock must be determined as the array of nodes or elements located at shock front. To avoid computationally expensive calculation of temperature gradient, corresponding to the shock location, a simple trick has been used. The cell is considered at the shock front if one and only one node of the cell has ambient temperature.

Following the described procedure, an array of elements from the shock front is formed for the flow field of RAM-C II experiment at altitudes of 61, 71 and 81 km, as it has been discussed in details in Chapter 4. The marked elements are shown in Fig. 5.3 for the temperature field in Fig. 5.4 at the altitude of 61 km. Once the location of the shock front is determined, the intersection of ray with shock is defined by a loop over each interface of element on the intersection with the emitted ray.

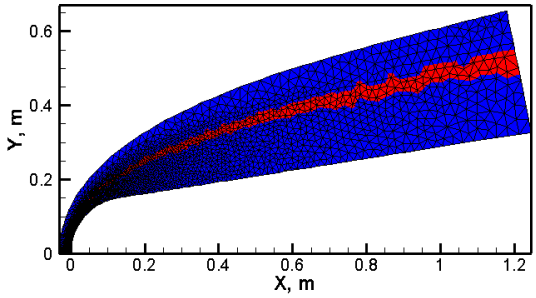

Fig. 5.3: Unstructured grid and nodes at the shock front

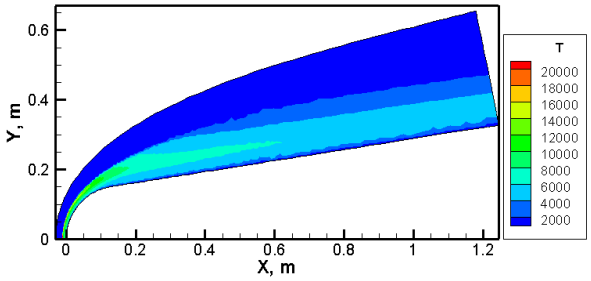

Fig. 5.4: Approximated temperature distribution

5.3 Gauss-Lobatto Quadrature

The Gauss-Lobatto quadrature serves two purposes for the present non-equilibrium radiation computation. First it generates a clustered distribution near the integral limits, and second it achieves a high order accuracy solution of RTE. The first feature is specially valued, because the quantum transitions within the high-enthalpy non-equilibrium flow are the most active at either the immediate post-shock region or the gas-solid interface. The variables of integration can be approximated by any other orthogonal polynomials, but the Legendre polynomial is the most widely used because of the accumulative knowledge of

its base function (Carnahan et al., 1969; Gautschi, 2004):

$$\int_a^b F(r)dr = \int_a^b P_n(r)dr + \int_a^b R_n(r)dr, \tag{5.1}$$

where $P_n(r)$ denotes the Legendre polynomial and $R_n(r)$ is the error of the n-th degree of the interpolating polynomial. A unique feature of this formulation is that the approximated function over the unequal increment within the integral interval is approximated by the Lagrangian form or the divided difference interpolation formula. In order to take advantage of this intrinsic property of an orthogonal polynomial, the interval of integration over the arbitrary limits of r_b and r_s must be transformed to $(-1; +1)$ by the following independent variable transformation $\xi = [2r - (r_b + r_s)]/(r_s - r_b);\ -1 \leq \xi \leq 1$. The GL quadrature over any arbitrary interval becomes:

$$F(\xi) = P_n(\xi) + R_n(\xi) = \sum_{i=0}^{n} L_i(\xi)F(\xi_i) + \left[\prod_{i=0}^{n}(\xi - \xi_i)\right]\frac{F^{n+1}(\xi)}{(n+1)!}; 1 \leq \xi \leq 1, \tag{5.2}$$

where L_i is known as the Cardinal function:

$$L_i(\xi) = \prod_{\substack{i=0 \\ j\neq i}}^{n}\left(\frac{\xi - \xi_i}{\xi_j - \xi_i}\right).$$

It is important to note that the $F(\xi_i)$'s are the specified functional values at the i^{th} root of the Legendre polynomial. In the RTM the $F(\xi_i)$ is simply the spectral volume emissive power $J_\nu^{em}(\mathbf{r}) = J_{b,\nu}(\mathbf{r})\kappa_\nu(\mathbf{r})$ at the root points along an emitting ray, under the LTE conditions.

By integrating the function $F(\xi)$ over the interval form -1 to +1, one gets

$$\int_{-1}^{1} F(\xi)d\xi = \int_{-1}^{1} \sum_{i=0}^{n} L_i(\xi)F(\xi_i)d\xi + \int_{-1}^{1} [\prod_{i=0}^{n}(\xi - \xi_i)]\frac{f^{n+1}(\xi)}{(n+1)!}d\xi = \sum_{-1}^{1} wt_i F(\xi_i). \quad (5.3)$$

In the above equation, wt_i is the so-called weight function and is defined as

$$wt_i = \int_{-1}^{1} L_i(\xi)d\xi = \int_{-1}^{1} \prod_{\substack{i=0 \\ j\neq i}}^{n} (\frac{\xi - \xi_i}{\xi_j - \xi_i})d\xi. \quad (5.4)$$

For the Gaussian quadrature formulation based on Legendre polynomial, the weight function can be evaluated by the following analytic formula (Carnahan et al., 1969),

$$wt_i = \frac{1}{n(n-1)\left[P_{n-1}(\xi_i)\right]^2};\ \xi \neq \pm 1. \quad (5.5)$$

The integration by GL quadrature in Eq. (2.81) can be simply represented by the sum of the products of the weight function and the spectral radiation intensity of the black body at roots ξ_i. The error of the integrand is easily determined by the analytic expression given by Eq. (5.3). The spectral radiation intensity by GL quadrature along the tracing ray is given as:

$$J_\nu(\mathbf{r}_b) = \frac{2}{n(n-1)}\left(J_{b,\nu}(\tau_s) + J_{b,\nu}(\tau_b)\right) + \sum_{i=2}^{i=N-1} wt_i J_{b,\nu}(\tau_i), \quad (5.6)$$

where $\tau_b = 0$ corresponds to the location at the surface of space vehicle: r_b = 0, $\tau_s = \int_{r=r_b}^{r=r_s} \kappa(\mathbf{r})dr$. The numerical procedures to calculate the roots of the Legendre polynomial and the weight functions of the Gaussian quadrature are straight forward and are processed and stored a priori for the RTM computations. The radiation flux density at location $\mathbf{r} = \mathbf{r}_b$

on the surface of space vehicle is calculated by Eq. (2.9).

5.4 Results

Three problems are explored to understand the applicability and advantages of GL quadrature together with the idea of the proximity nearest neighbor search. At first, the simulation of radiation transfer has been performed in the environment of the laser-induced plasma generation (the laser-supported combustion, LSC). This problem was explored previously from the experimental (Klosterman and Byron, 1974) and computational (Krier and Glumb, 1984; Raizer et al., 1991) points of view. The heat propagation in LSC waves is mainly due to the radiation transfer rather than the thermal conduction for large diameters of a laser beam (Raizer et al., 1991). The effect of radiative cooling is also very important for this type of problem. At the same time, the process of plasma generation can be described in a simple axisymmetric geometry and spherically-shaped temperature distribution (Surzhikov, 2004b). The typical peak temperature in the center of plasma region and the absorption coefficient are also available (Surzhikov, 2009).

An attempt to calculate the radiation flux density to the surface of the cylindrical chamber containing gas plasma and at the center of plasma region is a viable option to test the accuracy of Gauss-Lobatto quadrature prior to a given distribution of temperature and absorption coefficient. The analysis of accuracy is provided for cases when the analytical distribution of temperature is known as well as the approximation of available data from the grid to the ray is performed.

Thereafter the radiation transfer from the shock wave to the surface of space vehicle is

analyzed. The problem is studies using structured and unstructured grids. The application of GL quadrature is challenging since the database of gas properties is limited and shock front is captured by only few grid points.

5.4.1 Radiation transfer in geometry modeling laser-induced plasma

The geometry and grid used for laser-induced plasma generation problem are shown in Fig. 5.5. Temperature distribution is given analytically, according to recommendation in Surzhikov (2004b) by the following expression:

$$T = T_{min} + (T_{max} - T_{min})\, exp\,(-R/R_0)\,, \tag{5.7}$$

where T_{min} = 300 K, T_{max} = 18000 K, $R = \sqrt{x^2 + y^2 + z^2}$ and measured in cm, R_0 = 1 cm. The absorption coefficient is given by the exponential distribution and directly depends on temperature:

$$\kappa = \kappa_{min} + (\kappa_{max} - \kappa_{min})\, exp\left(-10\left(\frac{T_{max} - T}{T_{max} - T_{min}}\right)^2\right), \tag{5.8}$$

where κ_{min} = 10^{-5} cm^{-1}, κ_{max} = 1 cm^{-1}. This range of temperature and optical properties corresponds to the actual experimental data and computational results on laser-induced combustion waves (Klosterman and Byron, 1974; Krier and Glumb, 1984; Surzhikov et al., 2008). In the focus of the laser beam absorption is strong, reaching the Rosseland limit of optical thickness. A rapid drop of temperature and optical properties in the cold region corresponds to the nearly transparent propagation of radiation. The drastic change of

properties allows exploring the advantages of GL quadrature in the least favorable computational conditions.

The example of axial one-side normalized flux distribution is presented in Fig. 5.6 at x ≤ 0. Trapezoid rule with uniform spacing of points and GL quadrature are used with a fixed number of points along the ray: N = 10 and N = 20. One can see that the GL quadrature indeed gives more accurate results by the same number of points on the tracing ray. The increase of accuracy is observed not only in the region of active plasma but also in the cold region, where the temperature gradient vanishes.

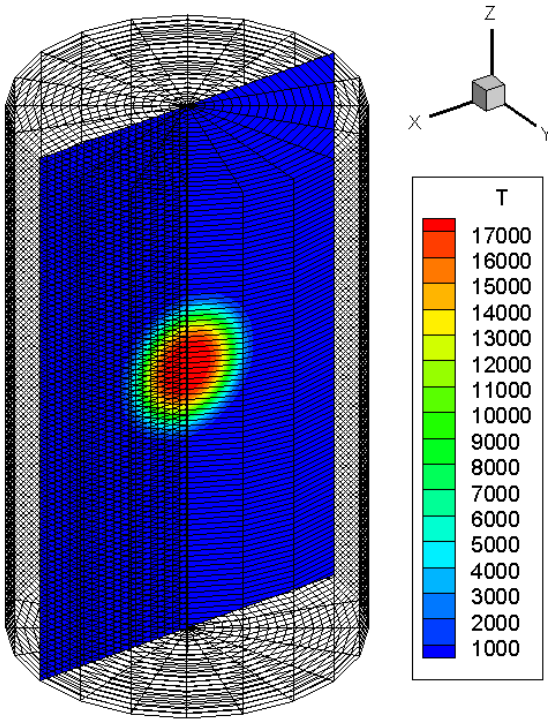

Fig. 5.5: Geometry and temperature distribution

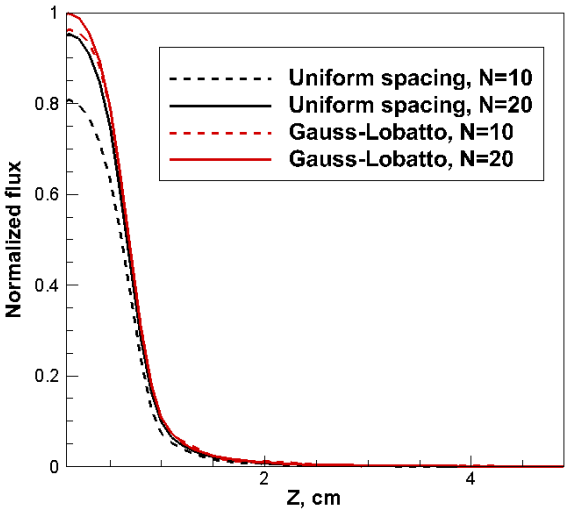

Fig. 5.6: Normalized flux density, axial component

The data on the normalized flux density at the surface of cylindrical enclosure (R = 3 cm) and at the center of plasma region (R = 0 cm) are given in Fig. 5.7 and 5.8 respectively.

The convergence of results is better for GL quadrature than the conventional trapezoid rule integration for location R = 0 cm. However the application of GL quadrature at the surface, R= 3 cm does not benefit the accuracy of integration. The active plasma region in the center of cylindrical enclosure is simply resolved by a lower number of points when GL quadrature assess the flux density at the surface. Comparison of Fig. 5.5 and 5.8 demonstrates the importance of clustering point along tracing ray in the region with high gradients.

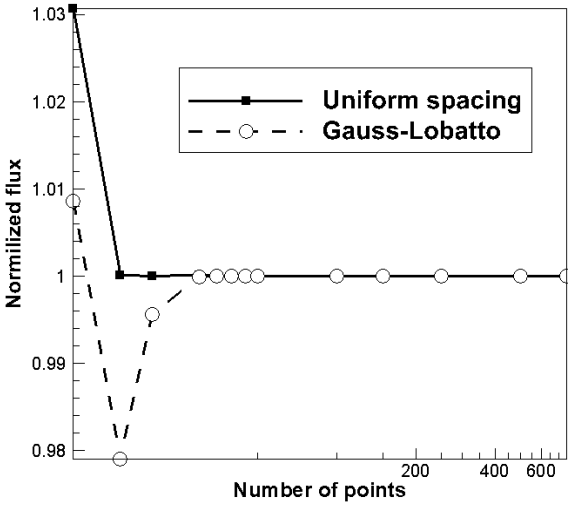

Fig. 5.7: Normalized surface flux density, constant absorption coefficient 0.1 cm^{-1}.

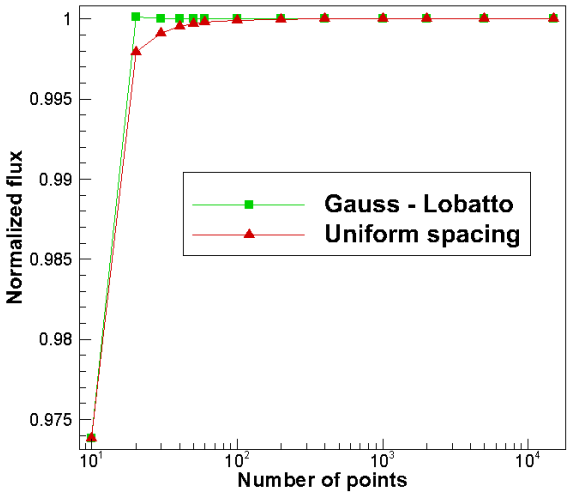

Fig. 5.8: Normalized flux density, constant absorption coefficient 0.1 cm^{-1}

The one-side flux density at the point x=y=z=0 cm is given in Fig. 5.9. Calculations are performed using two databases on temperature distribution: the analytical temperature field and the approximated temperature field based on the nearest neighbor search are used. This is done due to the fact that analytical distribution of properties is usually not available. A solution obtained by approximated temperature field allows to understand the inaccuracy due to the approximation of the properties.

The flux, obtained by trapezoid formula and integration over the uniformly spaced

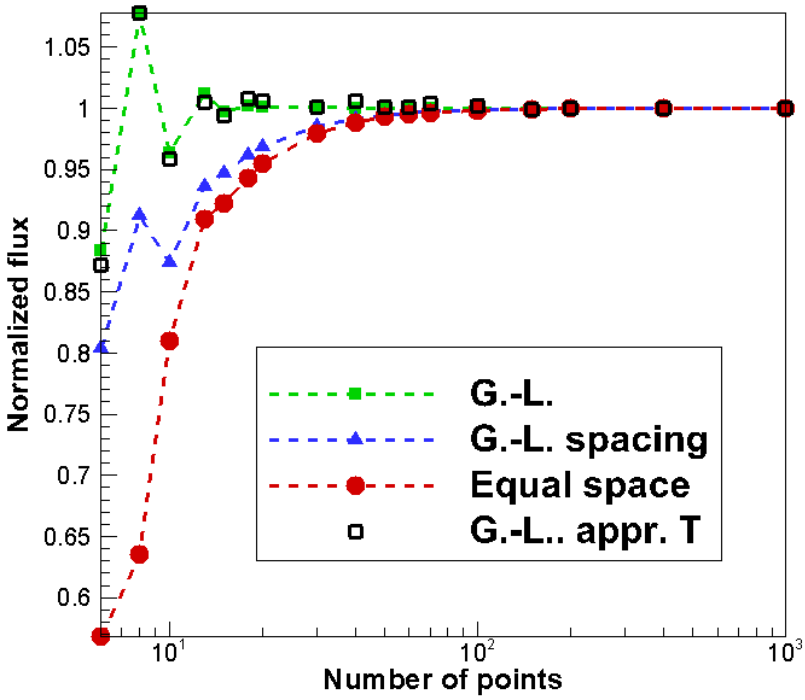

Fig. 5.9: Normalized flux density

segments is given by the curve with circular symbols. The curve with triangular symbols presents an integration using the same trapezoid rule but the length of segments is now given by the location of roots of Legendre polynomials, i.e. the similar spacing used by GL quadrature. The curve with solid symbols corresponds to the Gauss-Lobatto integration. All three curves use an analytical formula for temperature and absorption coefficient. The curve with empty symbols corresponds to the GL quadrature but the temperature and absorption coefficient are now approximated. A grid with dimensions 21x21x101 in x, y, z dimensions is used. For angular integration $N_\theta = N_\varphi = 41$ is assumed.

Gauss-Lobatto quadrature allows to significantly reduce the number of points along tracing rays required to obtain a converged solution. Both integration techniques using GL approach together with analytically calculated and approximated properties require nearly

20 points on the ray to obtain 1 % of accuracy. The approximation of properties brings noticeable inaccuracy in results, however they are relatively small compared to the error of low-order accurate integration method.

Clustering points in the region of active quantum transition benefits the accuracy of solution. One may compare curves with circular and triangular symbols in Fig. 5.9. However the GL approach using the same number of grid points produces a much more accurate solution. To obtain 1 % accuracy, an order of magnitude less number of points is required in integration by GL approach than by conventional approach.

5.4.2 Ray tracing method on structured grid

The radiation flux at the stagnation point of RAM-C II vehicle has been computed for all three altitudes (61, 71 and 81 km) studied in Chapter 4. In this section the GL quadrature is applied to resolve the spectral radiation flux to the surface of space vehicle by ray tracing method in a multi-group approach. In addition, the purpose is to compare the accuracy of integration by GL quadrature with Newton-Cotes integration when the flow field contains shock. The solution along single ray corresponding to the normal vector to the surface of space vehicle at stagnation point is analyzed. This is done to eliminate the inaccuracy brought about by integration over the entire solid angle.

Flux density at the stagnation point is normalized with respect to converged value and presented in Fig. 5.10 and 5.11. No approximation of properties (T, P, Y_i) is made and the properties at the point along the tracing ray are simply assigned as the properties of the nearest neighbor contained by the body-conformal grid. On contrary, flux density obtained

by the linear approximation of properties is given in Fig. 5.11. The approximation is based on the information contained by first two nearest neighbors to the point on the tracing ray.

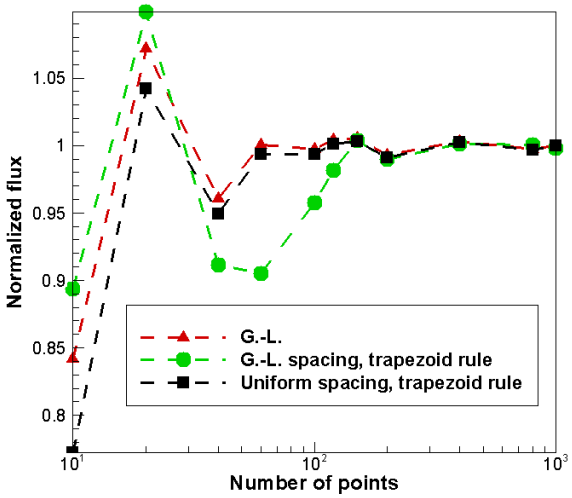

Fig. 5.10: Normalized flux density, zero order approximation, altitude of 61 km

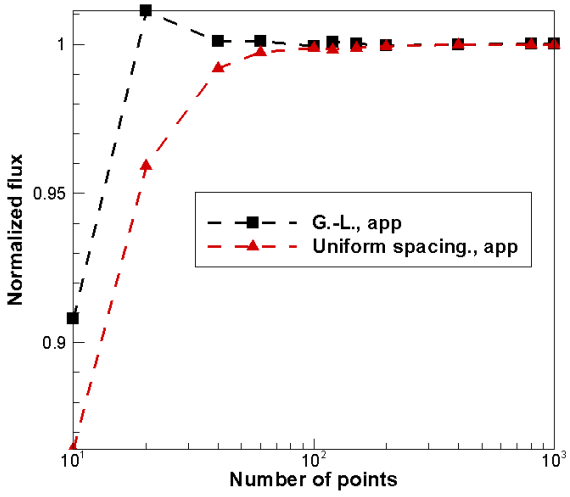

Fig. 5.11: Normalized flux density, first order approximation, altitude of 61 km

The flux density is calculated at a various number of points along the tracing ray. The minimal number of points N is 10 and the maximal is 10^3. The integration using GL quadrature and trapezoid rule with the uniform spacing is presented by red and black dashed curves in Fig. 5.10 and 5.11. The trapezoid rule is also applied for the spacing of points, provided by the roots of Legendre polynomials and shown by green curve in Fig. 5.10.

It follows from Fig. 5.10 that the clustering of points along the tracing ray in the region of active quantum transitions brings a small advantage in accuracy, compared to the conventional trapezoid rule if zero order approximation of properties is applied. This result contradicts the conclusion, made for the data presented in Fig. 5.9 for the problem of laser-induced plasma generation. The explanation of this different behavior of GL quadrature is contained in the fact that the properties along the ray for case in Fig. 5.10 contain discon-

tinuity due to the the shock wave at the altitude of 61 km, as it is shown in Fig. 4.2, while properties of media for the LSC wave problem are shock-free.

The linear interpolation of properties brings a faster convergent state for results by GL quadrature than those of the trapezoid rule. Basically, the 1 % accuracy is reached for N=20 points when Gauss-Lobatto quadrature is utilized and N=60 points are needed for uniform spaced segments and trapezoid rule. It is interesting to note that the number of points between the shock front and surface is of the order of 60, which corresponds to the accuracy of integration by trapezoid rule.

The accuracy of integration is also explored for flow field at altitudes of 71 and 81 km. The corresponding data on computed normalized flux density is shown in Fig. 5.12 and 5.13, respectively. The results by GL quadrature has are less scattered than those by trapezoid rule at the altitude of 71 km, however, the general behavior is similar to that observed at altitude 61 km in Fig. 5.10. The accuracy can be improved by introducing an appropriate approximation procedure for optical properties in order to receive the benefit by GL quadrature.

The situation at the altitude of 81 km is entirely different. The integration by GL quadrature for radiation transfer equation seems to provide an accurate solution starting from N = 10 points along the tracing ray, even though the distance between shock and surface is described by nearly 80 points of body-conformal grid. Both uniform spacing and spacing based on roots of Legendre polynomials together with using trapezoid rule for integration reach the same accuracy only at N = 40 points along a ray. In this case the application of Gauss-Lobatto quadrature allows to reduce necessary number of points by

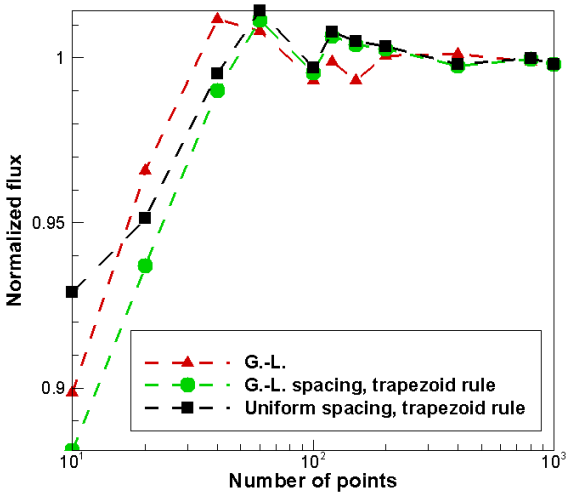

Fig. 5.12: Normalized flux density, zero order approximation, altitude of 71 km

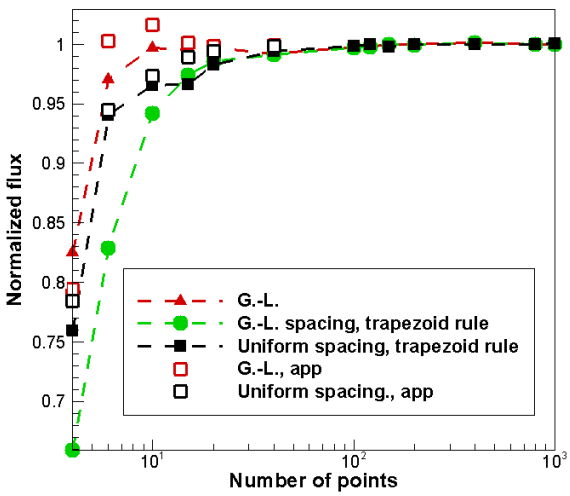

Fig. 5.13: Normalized flux density, zero order approximation, altitude of 81 km

a factor of 4. The general improvement of the accuracy for all types of integration can be explained by the significantly smeared temperature profile at the altitude of 81 km, as shown in Fig. 4.12. This situation is typical for the flow with the mean free path comparable to the characteristic dimensions of the flow.

The normalized flux density, obtained by using the first order approximation of properties at the altitude of 81 km is shown in Fig. 5.13 by the red and the black empty symbols for GL quadrature and trapezoid rule with uniform spacing. The linear interpolation of properties improves accuracy of both integration techniques. For GL quadrature the 1 % accuracy is reached by only 6 points along the ray.

Efficiency of nearest neighbor search

An overall efficiency of RTM with GL quadrature to solve Eq. (2.81) together with either space partition or consecutive search algorithms is studied for the flow field at the altitude of 81 km of RAM-C II probe trajectory. The computing time is presented in Table 5.1. The

number of points used by GL quadrature is four times less than for trapezoid rule, as it was found suitable for the solution of the RTE at the altitude of 81 km in the previous section. Proximity search algorithms allow to significantly reduce the required time for both GL and Newton-Cotes methods of integration. The consecutive search algorithm demonstrates the additional advantage of the reduced search domain compared to the partition search algorithm. The ratio of computing time between brute and partition search algorithms and brute and consecutive search algorithms is 5.52 - 6.07 and 8.9 - 9.05 for coarse grid computations, regardless of the integration technique.

Method	Number of points	Search algorithm	Time, s, coarse grid	Time, s, fine grid
GL	10	Partition search	20.25	29.36
GL	10	Brute search	122.92	379.82
GL	10	Consecutive search	13.81	14.09
Trapezoid rule	40	Partition search	84.54	117.21
Trapezoid rule	40	Brute search	467.37	1516.02
Trapezoid rule	40	Consecutive search	51.64	55.8

Table 5.1: Performance of ray tracing method, stagnation point, altitude of 81 km

Implementation of GL quadrature allows additional reduction of the number of points along the tracing ray by a factor of four with linear increase of the efficiency of the ray tracing method. It follows from Table 2.81 that GL quadrature and trapezoid rule have nearly the same operation count per point of the tracing ray. Brute search algorithm requires nearly three times more operations when grid dimension is doubled in each direction. The partition search and consecutive search algorithms increase the computational time by factors

of 1.45 and 1.02 respectively. This means that proximity search algorithms are relatively insensitive to the dimensions of the grid. The overall improvement in efficiency is nearly a factor of 30 for coarse grid and a factor of 100 for fine grid, compared to the conventional method of integration.

Radiation flux density

Integral radiation flux density is reported for altitudes 61, 71 and 81 km. The comparison of different mechanisms of heating is presented in Fig. 5.14, 5.15 and 5.16. The peak heating rates are summarized in Table 5.2. The flow field is computed by using Park chemical model (Park, 1993), Treanor-Marrone model of dissociation with $U = D/6R$ (Marrone and Treanor, 1963) and three-temperature thermodynamic model. Radiation flux is computed by using a 96-group spectral model in the optical interval 10^3 - 10^5 cm^{-1} of wavelength. The volume absorption coefficient of radiation is computed by the computer program ASTEROID (Surzhikov, 2000), courtesy of Prof. S. Surzhikov. Radiation transition rates in the gas mixture are assumed to be in local thermodynamic equilibrium with the translational temperature of heavy particles.

One can see that radiative heating rate varies from 27.69 % to 12.63 % of conductive and diffusion heat flux, given by Eq. (2.10) and 11.23 - 21.68 % of the total heating rate. The conductive and diffusion mechanisms of heating are prevailing over the radiation heating rate for these re-entry conditions. While the radiation heating falls rapidly downstream, the surface at the base of RAM-C II probe receives nearly 10-20 W/cm^2 of heating rate primarily due to conduction and diffusion mechanisms of heat transfer.

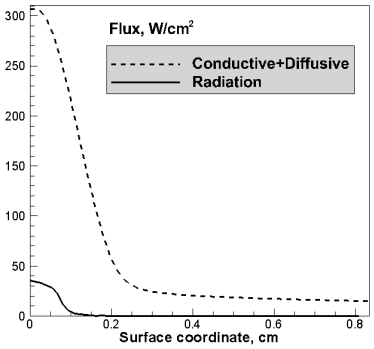

Fig. 5.14: Flux density, altitude of 61 km

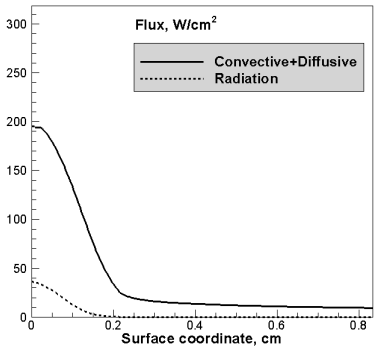

Fig. 5.15: Flux density, altitude of 71 km

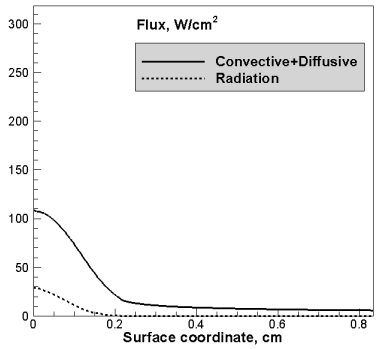

Fig. 5.16: Flux density, altitude of 81 km

Altitude, Flux	Cond.-Diff.	Radiative	Total	rad/cond+diff, %	rad/total, %
61 km	305.59	38.61	343.90	12.63	11.23
71 km	191.53	36.31	227.84	18.96	15.94
81 km	105.20	29.13	134.33	27.69	21.68

Table 5.2: Heating rates, W/cm^2

Radiation heating rates of RAM-C II probe were not previously published in literature. However calculations were performed for other space vehicles at the orbital re-entry conditions ($V_\infty \approx 7$ - 8 km/s). In the work Gorshkov (2010) the integral radiation intensity was calculated for Souz-TMA vehicle at similar re-entry conditions. The integral radiation heating rate in case of Souz vehicle does not exceed 10 W/cm^2 at the stagnation point. Also, both equilibrium and non-equilibrium calculations of radiation transfer were performed. The overestimation of radiation intensity is the factor of 2 - 8 in case of equilibrium calculations in UV spectrum. The exact numbers provided in work Gorshkov (2010) are not applicable for comparison with present results due to the different shapes of space vehicles, however the overestimation of heating rates using the assumption of LTE

indicates that radiation heating rates reported in present work should be considered as the upper limit.

5.4.3 Ray tracing method on unstructured grid

In order to explore the capability of ray tracing method the consecutive search methodology is generalized on triangular unstructured grids. An example of a triangular grid used in present calculations and an approximated temperature field are shown in Fig. 5.3 and 5.4. Approximation of temperature, pressure and gas composition is performed by assigning the data to the node of unstructured grid from the information of the nearest neighbor located on the structured grid.

Consecutive search algorithm

The construction of tables containing candidates of the nearest neighbor is described in Section 5.2. The performance of consecutive search algorithm on unstructured grid is shown in Table 5.3. Calculations are performed only for the stagnation point of RAM-C II. A number of rays is chosen to be the equal for both azimuthal and radial directions and is varying from 21 to 61 ray in each direction. The maximal number of rays to cover half-space is equal to 3721 and provides the converged solution. Total number of nodes contained in the unstructured grid is N_{node} = 10712 and 15282, total number of elements is N_{elem} = 20880 and 30056 for coarse and fine grid calculations.

Uniform spaced intervals and trapezoid rule are used to obtain solution along each ray, given by Eq. (2.81). The number of points along the tracing ray varies from 100 to 400. The computational time required to obtain spectral radiation flux in single spectral

region 29000-30000 cm^{-1} is presented for cases of brute and consecutive searches. The latter performs the search over the table containing N_{level} = 3 layers (levels) of adjacent cells as candidates for the nearest neighbor. While the actual number of cells that must be analyzed to retrieve the nearest neighbor can be different, the N_{level} = 3 used in present work corresponds to the crudest distribution of points along the ray for the shock layer radiation. When points of integration on the tracing ray are clustered (as for Gauss-Lobatto quadrature) the spacing between points decreases, leading to the smaller required value of N_{level}.

N, 21x21 ray	t_c, s, cons. search	t_b, s, brute search	t_b/t_c
100	4.34	11.69	2.69
200	8.24	22.50	2.73
400	18.57	44.62	2.4
N, 41x41 ray	t_c, s, cons. search	t_b, s, brute search	t_b/t_c
100	15.26	45.02	2.95
200	25.07	81.61	3.25
400	60.13	156.11	2.59
N, 61x61 ray	t_c, s, cons. search	t_b, s, brute search	t_b/t_c
100	37.57	113.14	3.00
200	86.21	219.42	2.54
400	148.66	433.64	2.91
400*	159.75	370.61	2.31

Table 5.3: Cost of ray tracing method, consecutive and brute search algorithms, stagnation point

While the absolute computing time depends on computational compatibilities and op-

timization, the ratio of the computing time offers useful insight. It follows from Table 5.3 that the computing time is proportionally increasing with the number of rays for both methods of search, since the total number of points grows by the same manner. For a given grid the ratio of performance is a factor of 3. The last row marked with upper symbol corresponds to the calculation performed on coarse grid with N_{node} = 10712 and N_{elem} = 20880. One can see the advantage of nearest neighbor search using table is increasing with mesh number density. This is explained by the fact that the range of search within the table of candidates does not depend on grid but depends on the number of levels of adjacent cells chosen to find nearest neighbors.

A number of numerical experiments are performed to understand the efficiency of consecutive search without involving calculation of optical properties and radiation transfer equation. The corresponding results are given in Table 5.4. The performance of consecutive search is analyzed for three different N_{level} = 3, 4 and 5. It is possible to see that the efficiency of consecutive search, compared to the brute search, drops as more adjacent cells are considered as possible nearest neighbor candidates. For N_level equal to three an approximate number of candidates included in the table is of the order of 50. For N_{level} equal to four the size of table is nearly 400, for N_{level} equal to five the size of table is nearly 1500 which is comparable to the size of the entire grid.

The ratio of time spent on search by brute and consecutive search algorithms is given in the third column of Table 5.3 and basically represents the ratio of the overall number of nodes to the number of nodes in the table of neighbor candidates. The small difference of given times is caused by the size of the particular table. The size of the table is quickly

Algorithm, coarse grid	Time, s	Ratio
Brute	1.62x10^{-4}	
Cons. N_{level}=3	1.2 - 1.5x10^{-6}	108-135
Cons., N_{level}=4	3.5-5.0x10^{-6}	32-46
Cons., N_{level}=5	1.81 - 1.83x10^{-5}	8.5-9.3
Algorithm, fine grid	Time, s	Ratio
Brute	1.80-2.0x10^{-4}	
Cons., N_{level}=3	1.3 - 1.7^{-6}	105-153
Cons., N_{level}=4	3.5-4.9x10^{-6}	36-57
Cons., N_{level}=5	1.81 - 1.85x10^{-5}	10-11

Table 5.4: Cost of consecutive and brute search algorithms, stagnation point

growing with the number of adjacent cells that are taken into account. The efficiency of consecutive search algorithm changes from 100-150 to the order of 10 for the typical grid, depending on the number of adjacent cells in the table. One may conclude that the appropriate spacing of points along the tracing ray is always more advantageous not only for accuracy of integration but also for computational performance.

5.5 Conclusion

The Gauss-Lobatto quadrature is shown to generate an accurate solution of the radiation transfer equation for the laser-induced plasma generation problem when applied in the region of high temperature gradients. The accuracy of radiation flux density produced by GL quadrature is also retained when properties are interpreted from the gasdynamic grid onto the tracing ray, instead of using analytical distribution of properties.

The GL quadrature to the shock-type flow field revealed a small advantage of the approach when applied to nearly-discontinuous solution without an appropriate approximation of thermodynamic and optical properties. However if the mean free path of particles in shock wave is large and shock front is smeared, the solution by GL quadrature redeems the desired accuracy, compared to the Newton-Cotes method. This favorable situation takes place when accounting for the radiation flux on the high altitudes of trajectory. When applied to the strong shock-type solutions, GL approach may require to use an extensive database of properties and appropriate approximation for points on the tracing ray in order to demonstrate the accuracy of the RTE solution.

Both partition and consecutive search algorithms show a great increase of performance when applied to the problem of radiation flux calculation on the surface of the space vehicle. The actual gain of the efficiency depends on the number of points and tracing rays used by RTM. For typical grids applied in two-dimensional calculations the consecutive search algorithm and GL quadrature increase the efficiency of the RTM by the factors of 30 and 100 for coarse and fine grid calculations, respectively. The combined approach of GL quadrature and consecutive search algorithm is expected to increase the efficiency of RTM for grids with larger dimensions.

The idea of the consecutive search algorithm for the unstructured grids rests on the construction of the table of nearest neighbor candidates. Present work demonstrates the efficient realization of the NNS algorithm by building the multi-level table of cells adjacent to the previous cell on the tracing ray with the known nearest neighbor. However the large difference in the spacing of nodes on the grid and points on the tracing ray may require larger table size and possibly eliminates the advantage of the consecutive search algorithm

for the unstructured grids. As a recommendation for the efficient application of the RTM on the unstructured grids the clustering of the grid both to the surface and to the shock is advised.

6. VIEW-FACTOR APPROACH

6.1 Introduction

View-factor approach is applied to solve radiation transfer equation in gas media with local temperature inhomogeneity. The radiative energy balance is considered in the two dimensional axisymmetric enclosure with the temperature distribution typical for the laser-induced plasma generation (Krier and Glumb, 1984) as well as for the re-entry space vehicle. The radiative emissivity of the hemispherical isothermal layer is also calculated by the view-factor approach and RTM for comparison with the analytical solution.

The results by the View-Factor approach are verified against the ray tracing method, P_1 approximation of Spherical Harmonics method and tangent slab approximation. Spectral multi-group radiative heating rates at typical re-entry conditions are resolved by the View-Factor approach demonstrating distinct advantages over the RTM in maintaining the asymptotic accuracy of RTE solution. General recommendations are derived for the application of VF approach in the optically thin and thick media and regarding the application in three-dimensional geometry of space vehicles.

However, the application of VF approach is not restricted to the aerodynamic applications. The radiation transfer in a cylindrical closure with the strongly inhomogeneous temperature distribution is also modeled. This configuration is widely used in physics of neutron transport (Davison and Sykes, 1957) and physics of laser generated plasma (Radziemski and Cremers, 1989) and thus it is important from the engineering point of

view.

The structure of this chapter is as follows. The governing equations of radiation transfer in the framework of VF concept are briefly described in the section 6.2. Three considered cases of radiation transfer and the specific derivation of the VF approach is provided in the section 6.3. Analysis of the radiative heating rates and the efficiency of VF approach is given in the section 6.4, followed by the conclusion.

6.2 Governing equations

The conservation equation of radiative energy under the assumption of LTE is used to describe the propagation of radiation in non scattering media. The validity of the LTE assumption is important, because it allows to dramatically simplify the source term in the RHS of Eq. (2.73). The VF approach can be generalized for non-Boltzmann thermodynamics by including the priorly calculated non-equilibrium emissivity of the gas media J_{em} in the RHS of RTE. However the detailed, state-to-state resolved radiation of gas media is out of the scope of present study. The LTE assumption allows to obtain the solution of RTE in a closed form, given for the radiative directional intensity $J\left(r,\Omega\right)$ by Eq. (2.81).

Boundary conditions have to be formulated for Eq. (2.81). One can consider the process of radiation transfer along the ray **s**, emitted from the elementary volume V_i in the direction of receiving surface A_j. Then the boundary condition for Eq. (2.81) must be formulated for the radiation intensity at the point $s = S$, located at the V_i When the external

radiation intensity is present, the boundary condition at $s = S$ can be written as

$$J_\nu\left(s\right)\mid_{s=S}= J_0\left(S\right). \tag{6.1}$$

The solution of the radiation transfer equation along particular direction Ω eliminates the angular component in radiation transfer and under the assumption of LTE the expression for the radiation intensity J may be obtained in a closed form:

$$J(\tau) = J_0(\tau_0)e^{-\tau} + \int_{\tau_0}^{\tau} J_b(\tau')e^{-(\tau-\tau')}d\tau', \tag{6.2}$$

where τ is the optical thickness of the participating media:

$$\tau = \int_{S_0}^{S} \kappa(s')ds'. \tag{6.3}$$

The numerical representation of integral in Eq. (6.2) in the absence of the external radiation, J_0 = 0, is then written in the next form:

$$J(\tau) = \sum_{k=1}^{N-1} \tilde{J}_b e^{-(\tau_k-\tau')}\left(\tau_{k+1} - \tau_k\right), \tag{6.4}$$

where the interval $[S, S_0]$ along the ray **s** is divided into N-1 uneven subintervals, $\tilde{J}_b$ is the average emissivity of the black body of the interval $[\tau_k, \tau_{k+1}]$. The summation in Eq. (6.4) is along the entire path of the photon emitted between points $s^{'}$ and S_0, corresponding to the surface. Typically, for the numerical estimation of integral in Eq. (6.4) the black body emissivity $\tilde{J}_b$ is chosen as the arithmetic mean value of the values on the edges of the

interval $[\tau_k, \tau_{k+1}]$. Density of radiation flux density and radiation energy can be found by integration of radiation intensity over the entire solid angle Ω, as it is shown in Eq. (2.82) and (2.83).

The optical model adopted by the View-Factor approach is the same as in the ray tracing method. A spectral interval of 10^3 - $10^{\ 5}$ cm^{-1} consists of 96 optical group. In each group the spectral absorption coefficient is averaged for the rotational structure of the spectrum via program code ASTEROID (Surzhikov, 2000). The proposed number of groups is typically enough to obtain group-independent solution for the flux density using the multi-group approach (Andrienko et al., 2012).

6.2.1 Basics of View-Factor approach

The VF approach is described in two-dimensional and three-dimensional geometries. The detailed derivation of the view factor for the particular problem is given in the next section. Assume the configuration of emitting volume V_i and irradiating surface A_j given in Fig. 6.1. The view factor of the volume element V_i from the point located at the A_j is given by

$$F_{i,j} = \frac{B_{i,j}}{V_i} \int\limits_{A_j} \int\limits_{V_i} T_{i,j,\nu} \frac{\cos\theta_{i,j}}{4\pi r_{i,j}^2} dV_i dA_j, \tag{6.5}$$

where the factor $B_{i,j}$ accounts for the shadowing between elements A_j and V_i and $T_{i,j,\nu}$ is the attenuation factor of the radiation intensity along the distance $r_{i,j}$, generally depending on the wave frequency. Note, that Eq. (6.5) is valid for any mutual location of V_i and A_j.

The spectral radiation flux density on the surface of A_j is then calculated as

$$W_\nu = \int_{A_j} \int_{V_i} T_{i,j,\nu} B_{i,j} \frac{J_{i,\nu}}{A_j} \frac{\cos\theta_{i,j}}{4\pi r_{i,j}^2} dV_i dA_j, \tag{6.6}$$

where $J_{i,\nu}$ is the spectral emissive power of volume V_i.

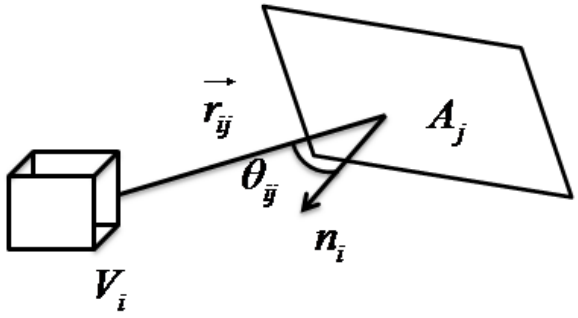

Fig. 6.1: View factor schematic

If the size of V_i and A_j is much smaller than $r_{i,j}$ then Eq. (6.5) is simplified:

$$F_{i,j,\nu} = B_{i,j} T_{i,j,\nu} \frac{\cos\theta_{i,j}}{4\pi r_{i,j}^2} A_j. \tag{6.7}$$

Generally speaking, Eq. (6.7) is valid only when $r_{i,j} \gg \sqrt[3]{V_i}$ and $r_{ij} \gg \sqrt{A_j}$. Every volume and surface can be divided into smaller sub-elements in such way that Eq. (6.7) is applicable. The view factor for sub-elements that belong to the same element is different, however thermodynamic properties are the same. The resulting radiation flux is calculated by the summation of contribution for all sub-elements.

One can consider the case when size of V_i and A_j is much smaller than the distance between them. Then the spectral flux density emitted by element V_i reaching the surface

A_j is calculated as:

$$W_\nu = \frac{F_{i,j,\nu}}{A_j} \int_{V_i} J_{i,\nu} dV_i. \tag{6.8}$$

In case of isothermal volume V_i with the constant absorption coefficient κ_i Eq. (6.8) can be further simplified:

$$W_\nu = \frac{F_{i,j,\nu}}{A_j} J_{i,\nu} V_i. \tag{6.9}$$

The attenuation factor of radiation is given by Beer - Lambert - Bouguer law as integral of the spectral absorption coefficient along the geometrical path $[S_0, S]$ of the photon of frequency ν and defined by the optical thickness of the path:

$$T_{ij,\nu} = exp\left(-\int_{S_0}^{S} \kappa_\nu\left(s\right) ds\right) = exp\left(-\tau_\nu\right). \tag{6.10}$$

When the absorption of radiation between emitting and receiving elements is small, i.e. $\tau_\nu \ll 1$, the attenuation factor turns into unity. In case of media with constant absorption, the optical thickness is proportional to the geometric path and attenuation factor is calculated as

$$T_{ij,\nu} = exp\left(\kappa_\nu\left(S - S_0\right)\right). \tag{6.11}$$

When the problem is axisymmetric, the radiating elements V_i located at the same distance $\widetilde{r}$ from the axis of symmetry can be jointed into a single ring-shape emitting element with the constant emission properties. The integration within the cylindrical volume $\widetilde{V} = 2\pi\widetilde{r}\Delta\widetilde{r}$ is then performed over the azimuthal angle $\varphi \in [0, 2\pi]$:

$$W_\nu = \int_0^{2\pi} \int_{A_j} B_{i,j,\varphi} \frac{J_{i,\varphi,\nu}}{A_j} \frac{\cos\theta_{i,j,\varphi}}{\pi r_{i,j,\varphi}^2} T_{i,j,\varphi} dA_j \widetilde{r} \Delta \widetilde{r} d\varphi, \tag{6.12}$$

where B, T, θ, I and r contain the dependence on φ unless the surface A_j is located on the axis of symmetry. Shadowing factor $B_{i,j}$ may vary from zero to unity, in other words, photons emitted only from the segment of $\widetilde{V}$ reach the surface. Equation (6.12) provides the total flux density incident on the area element A_j from the ring formed by the volume element V_i in the plane of symmetry z=0 for two-dimensional axisymmetric geometry.

In case of three-dimensional geometry integration over angle φ can not be applied since the thermodynamic properties are varying with the angle φ. The radiation flux can be calculated using modified appearance of Eq. (6.12):

$$W_\nu = \sum_{k=1}^{N\varphi-1} \int_{A_j} B_{i,j,\varphi} \frac{J_{i,\varphi,\nu}}{A_j} \frac{\cos\theta_{i,j,\varphi}}{\pi r_{i,j,\varphi}^2} T_{i,j,\varphi} dA_j \widetilde{r} \Delta \widetilde{r} \left(\varphi_{k+1} - \varphi_k\right), \tag{6.13}$$

where the factor $B_{i,j,k}$ is accounting for the shadowing between element A_j and sector k of the ring, formed by V_i and angle $[\varphi_k, \varphi_{k+1}]$ and simply depends on the sign of $cos\theta$.

Governing equations of gasdynamics are given in Chapter 2 and provide an input data for the view-factor approach to calculate the radiation heating rates at re-entry. Two other test problems, considered in present chapter adopt analytically generated temperature distribution. The parameters behind the shock front are described by the multi-temperature model including mean flow continuity equation for a mean flow Eq. (2.2), conservation of momentum Eq. (2.5), conservation of translational and rotational energy Eq. (2.7), mass conservation of species Eq. (2.21), and conservation of vibrational Eq. (2.12) and free

electron energy Eq. (2.16) separately. The energy lost due to radiation transfer equation is neglected in the energy equation.

6.3 Test cases

Three test problems are considered to investigate the capability of the view-factor approach. At first the radiation transfer in the isothermal hemispherical enclosure is considered. This test case is chosen due to the simplicity and the existence of the analytical solution for the radiation flux density at the base of the enclosure.

Second case simulates the axisymmetrical enclosure with highly inhomogeneous temperature distribution. The properly chosen spatial distribution of absorption coefficient and temperature (Surzhikov, 2004b) allows to reproduce the radiation transfer typical for the laser-generated plasma environment. Because of the specific pattern of plasma propagation this problem is often called as the laser-supported combustion (Raizer et al., 1991). Because of the high temperature gradients and the importance of the radiation heat transfer mechanism this problem appears to be challenging from the computational and physical points of view. The comparison of the radiation flux density obtained by the VF approach, ray tracing method and diffusion approximation of spherical harmonics method is provided.

The third computational case addresses the re-entry of a space vehicle by modeling the RAM-C II flight experiment (Grantham, 1970). The calculation of the integral radiation flux density on the surface of a space vehicle is provided. The VF approach, the ray tracing method and the TS approximation are brought together to investigate the advantages of the radiative transfer models in the presence of the shock wave.

6.3.1 Radiation transfer in hemisphere

The geometry is presented in Fig. 6.2. Radiative flux density in the center of the hemisphere base can be obtained analytically using the definition of the flux density, Eq. (2.82). Using the solution of the RTE along direction Ω one can obtain resulting value of flux density after integration over the solid angle:

$$W_n = \int_0^{2\pi} d\varphi \int_0^{\pi/2} J\left(R, \varphi, \theta\right) cos\theta sin\theta d\theta = \pi J_b \left(1 - e^{-\kappa R}\right). \tag{6.14}$$

The governing equation of the ray tracing method, Eq. (2.81) is the hemisphere. Since the media in the hemisphere is isothermal and has constant absorption coefficient there is no need for the refinement of the number of points along the ray. However, the convergence for the increasing number of rays has to be verified. Calculations have been performed at different numbers of rays, starting from the coarse angular resolution, provided by N_φ = N_θ = 7 up to N_φ = N_θ = 161 in each angle direction. Note, that direct application of VF approach, Eq. (6.9), yields to analytical solution.

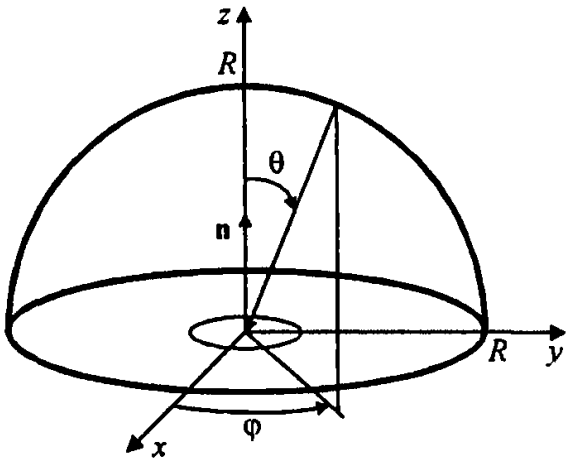

Fig. 6.2: Geometry of the hemisphere

6.3.2 Radiation transfer in the cylindrical enclosure

The axisymmetric enclosure with the inhomogeneously distributed thermodynamic properties is widely known for studying the phenomena of propagation and interaction of radiation in the weakly ionized plasma generated by a focused laser beam. Observed in the experiments by Conrad et al. (1996); Klosterman and Byron (1974); Tret'yakov et al. (1994), the laser-supported waves became a subject of thorough study in a large number of theoretical works because of their practical application in laser rocket engines (Jackson and Nielsen, 1974; Krier and Glumb, 1984).

The cold plasma with the temperature 1-2 ev generated by weakly focused laser beams is the essence of laser-supported waves. It has been shown, that for the large diameters of the beam (greater that 5 mm for some types of laser, e.g. CO_2 laser) the heating of the media, adjacent to the beam, is caused primarily by radiation processes. The failure to account for the radiation as a heating mechanism may lead to a significant underestimation of the velocity of the LSC wave (Jackson and Nielsen, 1974).

Present work considers the cylindrical enclosure with the spherical region of high temperature decaying exponentially. The temperature distribution with the maximum 18000 K is shown in Fig. 6.3. Absorption coefficient is varying from 10^{-2} to 1 cm^{-1}. This is a typical condition in LSC waves.

The interest of present work is the calculation of radiative flux density on the surface of the cylindrical volume. Both the RTM and VF approach are applied to obtain flux density at the analytically given temperature distribution and constant absorption coefficient. The analytical solution of RTE is not available, however the results are compared to the diffusion approximation of radiation transfer equation, which has been previously applied to encounter radiation-gasdynamic interaction in LSC waves (Jackson and Nielsen, 1974; Surzhikov, 2009). Although it has been shown that diffusion approximation may miscalculate the thermal radiation transfer in optically thin media (Andrienko and Surzhikov, 2012; Jackson and Nielsen, 1974) and specially in the case of anisotropy of temperature, the diffusion approximation is used as a simple and efficient approach to provide information on the accuracy of calculations.

View-factor formulation

The geometry of the cylindrical enclosure is shown in Fig. 6.4. The application of Eq. (6.12) combined with geometric relations (6.15) and (6.16) gives an expression for the flux density, Eq. (6.17).

$$\mathbf{r} = \left(\widetilde{r}cos\varphi + R,\ \widetilde{r}sin\varphi,\ z_i - z_j \right)^T, \tag{6.15}$$

$$r cos\theta = \widetilde{r} + R \tag{6.16}$$

$$W_j = \int_{V_i} \frac{2J_i \widetilde{r} \left(\widetilde{r} cos\varphi + R\right)^3}{\left(\widetilde{r} + R\right)^2 \left(\widetilde{r}^2 + R^2 + \left(z_i - z_j\right)^2 + 2R\widetilde{r} cos\varphi\right)^{3/2}} d\widetilde{r} d\varphi dz \tag{6.17}$$

Integral in Eq. (6.17) can be expressed in the elliptic integrals of first and second kind, giving the analytic expression for the flux density on the area A_j. Final expression for the general appearance of integral (6.17) is given in appendix B. The integration in Eq. (6.17) is performed for the entire range of φ from 0 to 2π, since there is no shadowing between V_i and A_j.

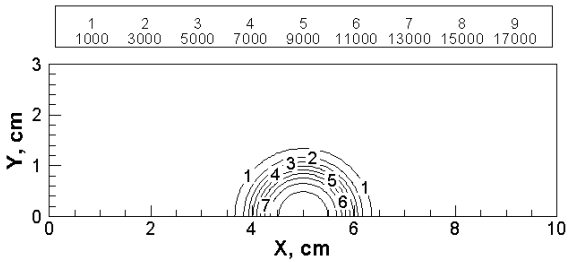

Fig. 6.3: Temperature distribution in the axisymmetric closure

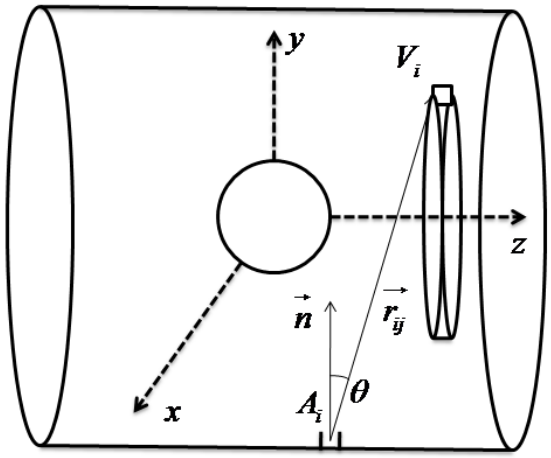

Fig. 6.4: Geometry of LSC waves

Diffusion approximation

The RTM and VF approach are compared with the P_1-approximation of spherical harmonics method (Davison and Sykes, 1957). The main reason for this comparison is to demonstrate the accuracy and efficiency of the VF approach compared to the well known and widely used method. The governing equation of the P_1 approximation is formulated for the

volume density of radiation energy U given by Eq. (6.18) and flux density $\mathbf{W}$ obtained by Eq. (6.19).

$$\nabla \left(\frac{c}{3\kappa} \nabla U \right) + c\kappa U = 4\pi c\kappa J_b \tag{6.18}$$

$$\mathbf{W} = \frac{c}{3\kappa} \nabla U \tag{6.19}$$

Since the exact boundary condition can not be formulated for spherical harmonics method in principle, an approximate BC is applied. Three types of boundary condition by Mark (1947), Marshak (1947) and Pomraning (1964) are employed to obtain the solutions of Eq. (6.18) and (6.19).

6.3.3 Radiation transfer at the re-entry conditions

The entry conditions are taken from the work Grantham (1970) and gasdynamic parameters and chemical composition are taken from the solution of governing equations with Park chemical mechanism, Treanor-Marrone model of preferential dissociation and three-temperature thermodynamic model. Tangent slab approximation is used to obtain an estimation of the radiation flux density.

The schematic of the emitting volume and receiving surface for the re-entry space vehicle is shown in Fig. 6.5. Substituting the expression for the radius vector $r_{i,j}$ and directional angle $\theta_{i,j}$ into Eq. (6.12) the expression for radiation flux density can be obtained:

$$W_v = JsR_i \int_{\varphi_1}^{\varphi_2} \tau_{ij} \frac{(x_i - x_n)\, n_x - y_n n_y + R_i n_y \cos\varphi}{\left((x_i - x_n)^2 + R_i^2 + y_n^2 - 2R_i y_n \cos\varphi\right)^{3/2}} d\varphi, \tag{6.20}$$

where s is the area of the ring formed by intersection with the plane z=0, R_i is the radius of the ring, (n_x, n_y), (x_n, y_n) are coordinates of the unit normal vector **n** to A_j and the location of the center of A_j. The shadowing factor B_{ij} in Eq. (6.20) is replaced by integration over the incomplete angle φ. The shadowing angles φ_1 and φ_2 can be easily computed for two-dimensional axisymmetric geometry and for three-dimensional geometry because such computation is not applicable, since shadowing factor simply takes the boolean value. In case of no shadowing φ_1 = 0 and φ_2 = 2π. Integral in Eq. (6.20) cannot be expressed in elementary functions. However, an accurate calculation is available using elliptic integrals of the first and second kind. The numerical calculation of elliptic integrals is a well-known problem and efficient solutions are available (Abramowitz and Stegun, 1964) and given in appendix C. The total flux on the surface element A_j can be obtained by summation in Eq. (6.20) over all radiating volumes V_i.

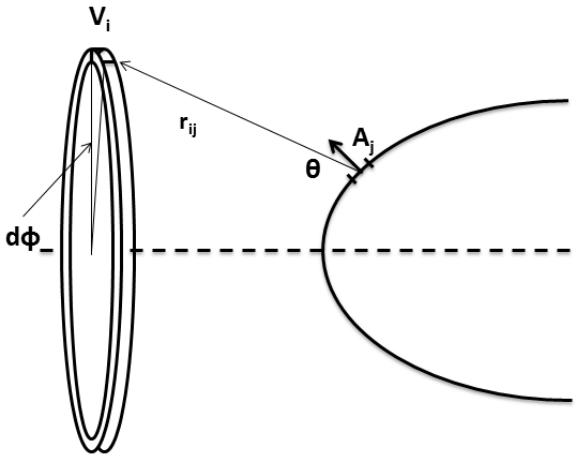

Fig. 6.5: Schematic of the VF approach for the re-entry environment

It is important to understand that Eq. (6.20) is derived under the assumption that surface element A_j and volume element V_i are far enough from each other such that the radius vector and directional angle $\theta_{i,j}$ in Eq. (6.8) can be assumed constant during the integration over V_i and A_j. In case of closely spaced elements V_i and A_j an additional subdivision into smaller elements may be necessary, as it is shown in Bose and Wright (2004). This situation takes place when attempting to account for the contribution of elements located close to the surface. Although the emission near the wall is typically much lower compared to the contribution of the shock layer, the absorption of radiation may be significant. It will be shown below that for a trajectory point at a low altitude the absorption of radiation is noticeable and accurate treatment of closely spaced elements is required.

Eq. (6.20) provides a semi-analytical expression for the flux density on the surface of space vehicle resulting from the arbitrary volume V_i in the shock wave. The total flux density is found by simple summation over the entire shock front and relaxation zone. This means that Eq. (6.20), as well as Eq. (6.17), provides a semi-analytical solution of RTE. The VF approach is expected to generate an asymptotically accurate solution of RTE at a given database of thermodynamic and optical properties. Please note, that no approximation of properties is required to obtain J_{em} as in case of RTM.

6.4 Results

6.4.1 Hemisphere

View factor is given by Eq. (6.8) and yields to the analytical expression of the flux density at the center of hemisphere's base with $T_{i,j} = exp\,(-\kappa r)$ and $F_{i,j} = 1$. Since both analytical

solution and VF approach become equivalent to each other, the results of latter is not presented. The normalized flux density given by the RTM at different numbers of rays emitted from the center of the base is presented in Fig. 6.6. The RTM provides an asymptotically accurate solution of Eq. (2.73) when the number of rays is large enough. The convergence rate does not depend on the optical thickness since the optical properties are uniform along each ray. The convergence for the number of nodes along a particular ray demonstrates the trivial equivalence of the integration procedure since the media is isothermal. However, the Fig. 6.6 indicates that the results of the ray tracing method can be used as a reference solution in case when an analytical solution is not available.

6.4.2 Cylindrical enclosure

The flux density to the surface of the cylinder is given by the RTM, VF approach and the P_1 approximation in Fig. 6.7, 6.8 and 6.9, corresponding to the absorption coefficient varying from 1 to 0.01 cm^{-1}, respectively. First of all, the asymptotically accurate solution by RTM is perfectly reproduced by the VF approach in the entire range of optical thickness. At small optical thickness the P_1 approximation fails to predict the flux density compared to the VF approach, regardless of the boundary condition. At κ = 1 cm^{-1} the difference between the peak value of flux density by P_1 approximation and VF is nearly 30 % and the best result is obtained with the use of Mark's boundary condition. As the thickness decreases the difference between VF and P_1 approximation increases. The distribution of the flux density given by the P_1 approximation becomes less steep, eventually reaching the nearly uniform behavior. This is because of the concept of the "diffusive" propagation of

radiation adopted by the P_1 approximation and reflected in Eq. (6.19).

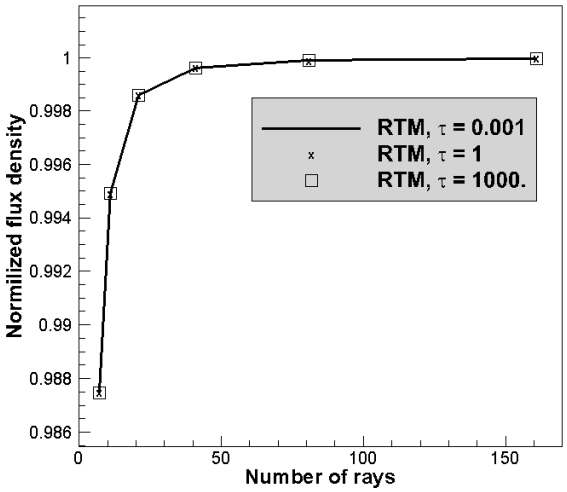

Fig. 6.6: Convergence of RTM

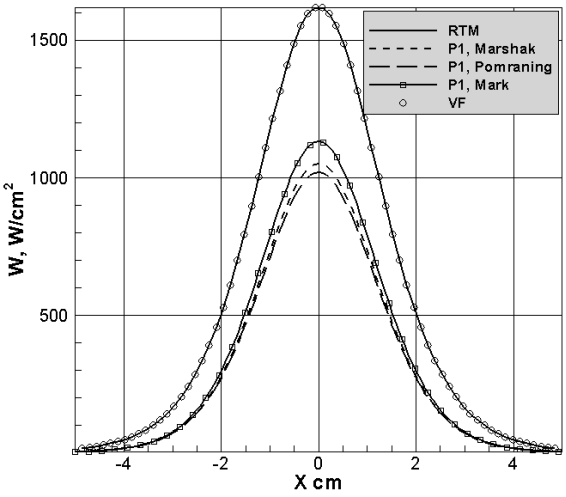

Fig. 6.7: Flux density, κ = 1 cm^{-1}

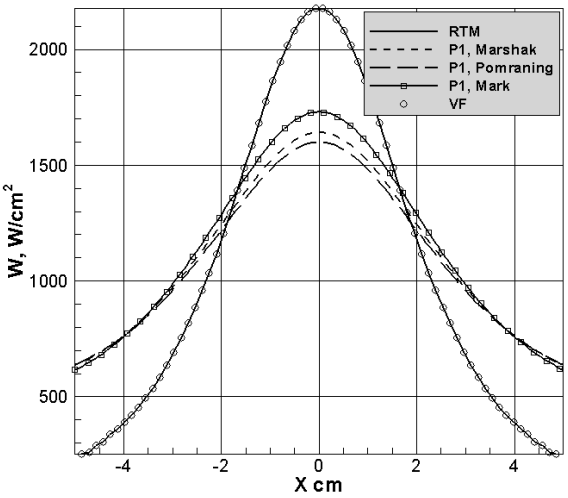

Fig. 6.8: Flux density, κ = 0.1 cm^{-1}

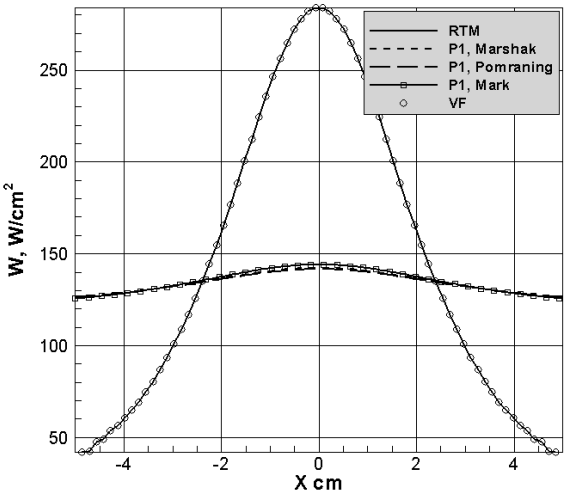

Fig. 6.9: Flux density, κ = 0.01 cm^{-1}

Note, that different approximate boundary conditions in P_1 approximation do not introduce any significant difference in the results when the gas is transparent, as it can be seen in Fig. 6.9. All three types of boundary conditions virtually yield to the condition $\partial U/\partial \mathbf{n}$ = 0 in this case. To increase the accuracy of SHM the higher order approximation can be used. However, the exact BC for SHM can not be formulated in principle.

Efficiency of RTM and VF approach is investigated. As it is stated above, to obtain solution along a particular ray in RTM the interpretation of gasdynamic properties from body-conformal grid to the grid of RTM is needed. The search of the nearest grid node at the specified location on the tracing ray consumes significant fraction of resources (Shang et al., 2014). On the other side, since no interpretation of temperature field in VF method is needed, the semi-analytical calculation of Eq. (6.4) takes nearly negligible amount of computational time compared to the RTM. Regardless of the optical thickness of media, the VF approach is 94.3 times more effective than RTM when flux density on the wall of cylindrical enclosure is calculated. Compared to the P_1 approximation, the VF approach demonstrates 10.5 times greater efficiency at κ = 0.01 cm^{-1} and approximately the same performance at κ = 1 cm^{-1}.

6.4.3 Radiation transfer at the re-entry

Comparison of the radiative flux at the altitudes of 61, 71 and 81 km is presented in Fig. 6.10, 6.11 and 6.12. The results by RTM and the VF approach are obtained for two cases: when the media between the shock front and surface of the space vehicle is considered to be transparent for the electromagnetic radiation (T = 1 in Eq. (6.7)) for the entire range of wavelength and when absorption is taken into account. The study of the absorption is for better understanding of the attenuation and due to the significant difference in the formulation of the VF approach when absorption is taken into account. The results by tangent slab approximation are given by the dashed curve.

The following parameters have been used to obtain flux by the RTM and VF approach.

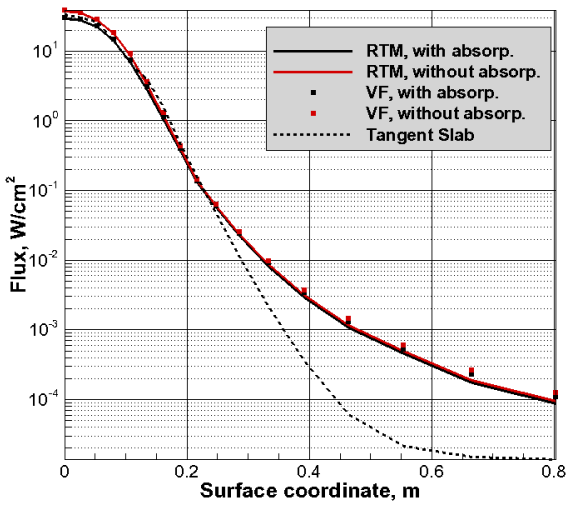

Fig. 6.10: Integral radiative flux, altitude of 61 km, coarse grid

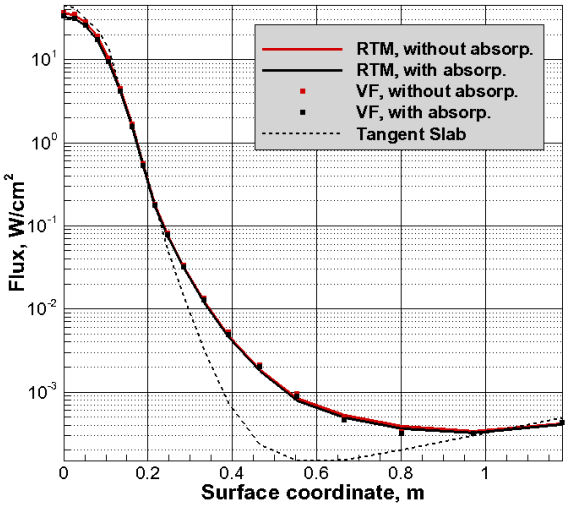

Fig. 6.11: Integral radiative flux, altitude of 71 km, coarse grid

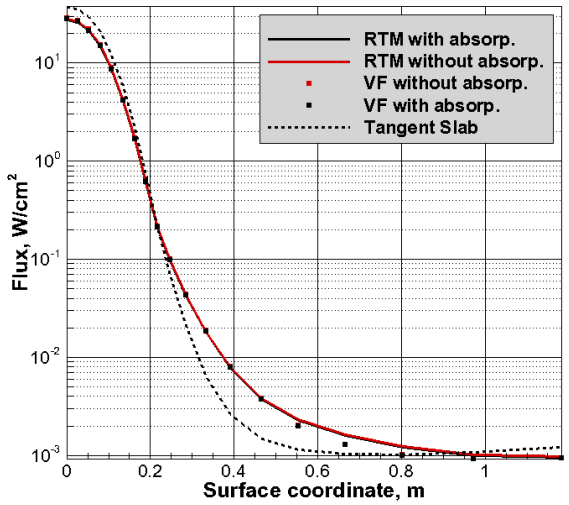

Fig. 6.12: Integral radiative flux, altitude of 81 km, coarse grid

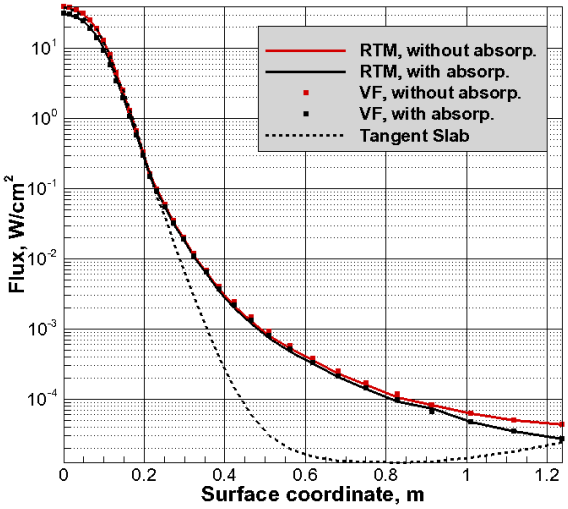

Fig. 6.13: Integral radiative flux, altitude of 61 km, fine grid

The RTM uses $N_\varphi = 41$ rays in azimuthal direction and $N_\vartheta = 41$ rays in the radial direction of the local spherical system on the surface of vehicle. It was shown that this number of rays is sufficient to reach convergence (Shang et al., 2013). The number of points N along each tracing ray is nearly equal to the number of grid points between shock front and surface and varies from 80 for altitude 81 km to 60 for altitude 61km. No attempt has been made

to interpolate the gas properties from the information of the nearest neighbors. Properties at the particular location on the tracing ray are simply assigned as the properties of the nearest neighbor of the gasdynamic grid. As it is shown below, zero order approximation is satisfactory for a typical gasdynamic mesh and corresponds to the actual amount of data originally contained in the gasdynamic mesh.

When absorption of radiation is neglected, the Eq. (6.20) is used to calculate flux to the surface. Attenuation factor is equal to unity for every emitting element of the gasdynamic grid and no approximation of gas properties is needed to calculate optical thickness of the media. However, in order to properly account for the emission from cells located close to the wall, the refinement of participating elements is undertaken. The indicator of the refinement for a particular cell is chosen as the ratio of the maximum size of the cell to its distance toward the surface. When this ratio is small, say, 0.1, no refinement is needed. In opposite situation each gasdynamic cell is divided into 9 cells in i and j direction by recommendation of Bose and Wright (2004). This procedure allows to obtain converged results for taking into account even cells next to the surface of the space vehicle. It's worth mentioning that although the refinement is needed, the cost of it is still much smaller than the cost of calculating the emitting properties. In the present case, the refinement does not take more than 10 % of the total computational time.

The case when absorption is taken into account makes utilization of VF approach more complicated and expensive. The optical thickness between each pair of emitting and receiving elements has to be calculated and thus the search of the nearest neighbor is involved. Points of integration along the distance between the emitting volume and receiving surface are equally distributed and gas properties are evaluated at their locations. In order to avoid

an unnecessary large number of points for short distances (when computation is performed near the surface), the available number of the gasdynamic grid points between the emitting element and surface is estimated. For the surface location at point (i_s, j_s) and location of the emitting volume (i_v, j_v) the number of points is estimated as $max\left(\left|i_s - i_v\right|, \left|j_s - j_v\right|\right)$. This step allows to save large amount of the computational time.

Several observations are extracted from the flux density when absorption is accounted for. First of all, the tangent slab approximation gives a reasonable value of the radiative flux only on the hemispherical cap of the vehicle, since the bow shock configuration is valid only there. The difference between TS approximation and RTM or VF approach does not exceed 30 %, which is in the range of expected correction factor, given in the work Wright et al. (2005) for the blunt body configuration. The severe deviation of the flux density by TS method at the afterbody of space vehicle from RTM and VF approach is observed for the entire range of altitudes. This fact is explained by the pattern of the flow field which has no shock structure and cannot be approximated as a slab.

The stagnation flux calculated by RTM for absorbing and transparent media is given in Table 6.1 in W/cm^2. The absorption of the radiation at given entry conditions is significant only for low altitude points of trajectory. The insignificant absorption at high altitudes can be explained by the relatively low entry velocity (nearly satellite speed) as well as low density. However, at altitude of 61 km attenuation of the absorption is more than 20 % of the total value and has to be taken into account.

Finally one may note, that the proposed realization of RTM and VF approach allows a very good matching of the results between these two techniques. The maximum of the

Altitude	With absorption	Without absorption	Difference
81 km	27.42	28.21	0.028
71 km	32.60	36.06	0.096
61 km	28.90	36.92	0.217

Table 6.1: Radiation heating rate with and without absorption taken into account

relative difference is less than 5 % for forebody and 10 % for the afterbody. The difference is caused most probably by the zero-order approximation of properties implied by RTM and can be eliminated by the gasdynamic mesh refinement. Calculation of the flux density on refined mesh for the altitude of 61 km is presented in Fig. 6.13. Difference in the flux at forebody does not exceed 1.8 % and 5.5 % for the afterbody.

Efficiency of the view-factor approach

The quantitative study of the efficiency of RTM and VF approach is provide for the stagnation point and afterbody radiation heat flux. Table 6.2 provides the computational time depending on the refinement of cells (sub-cell) closely spaced to the surface, in order to properly take the absorption into account.

Point on the surface	m=1, n=1	m=5, n=1	m=5, n=5	m=5, n=5, fine mesh
i = 1 (front)	4.29	4.41	4.52	8.30
i = 171 (afterbody)	28.51	29.42	30.83	72.56

Table 6.2: Time required by VF for the mesh refinement, s

The number of sub-cells varies from $n = m = 1$ (no refinement) to $n = m = 5$ in i

and j grid directions. View factor varies for each sub-cell that is at the same cell, however gasdynamic properties are the same for all sub-cells. As it can be seen from Table 6.2 the refinement of the closely spaced cells increases the computational time of VF approach by 5 % indicating that the major part of time is spent on the radiation properties calculation, while calculation of the view factor is much less expensive. The refinement of the mesh spacing by a factor of two along each grid direction increases the computational time of VF approach by approximately two times. Calculation of the flux at the afterbody is more expensive, since more cells are involved in contribution of the total heat flux. This phenomenon is purely geometrical and can be eliminated by reconstructing the gasdynamic mesh.

Table 6.3 demonstrates the efficiency of the VF approach and the ray tracing method. Comparison is performed for both cases when absorption is neglected as well as when absorption is taken into account. To highlight the factor describing the computational expenses of the particular case, the total operations count and count for the optical properties are included.

Approach/parameters	Time, s	Total count	Properties count
TS	0.5	$1.02\text{x}10^{9}$	$7.59\text{x}10^{8}$
VF, no absorption	3.4	$1.41\text{x}10^{10}$	$5.20\text{x}10^{9}$
VF, with absorption	$4.0\text{x}10^{2}$	$7.41\text{x}10^{11}$	$1.20\text{x}10^{11}$
RTM	$5.2\text{x}10^{2}$	$1.02\text{x}10^{12}$	$8.09\text{x}10^{11}$

Table 6.3: Comparison of time, VF, RTM and TS, coarse grid (187x93)

First, among all the techniques the tangent slab approximation is the most efficient

and least accurate radiation transfer model. The efficiency of the TS approximation is due to the semi-analytical integration of the angular dependence of the radiation intensity using integral-exponential functions of Chandrasekhar, introduced in Chandrasekhar (1960), while the two other methods are essentially performing direct angular integration. The accuracy of TS method is poor due to the significant curvature of the surface and it is not recommended to be applied at the afterbody.

Second, it can be seen that the presence of the absorption makes no difference in the efficiency of the ray tracing method, while the VF demonstrates 118.7 times decrease of the efficiency when the calculation of the attenuation factor is required. The difference in the efficiency is 151.5 times comparing VF and RTM when absorption is neglected. The VF accounting for the absorption is still more efficient then the RTM.

Finally, the significant decrease of efficiency of the VF approach when absorption is taken into account is caused primarily by cost of the calculation of the optical properties. This conclusion follows from the increase of operational counts for properties evaluation nearly by the same factor as the total operational count of the calculations. In this sense the development of more efficient optical models is highly desired as the factor restricting the efficiency of radiation transfer model.

6.5 Conclusion

The radiation transfer model based on the view-factor approach is developed for the numerical solution of RTE under the assumption of LTE using the multi-group optical model. Solution for the radiative flux in several important engineering applications is obtained.

Radiation transfer model demonstrated high efficiency and asymptotically accurate results for the adopted thermodynamical and optical model.

The view-factor approach dramatically simplifies the solution of RTE in the weakly absorbing media. As a matter of fact, in two dimensional axisymmetric geometry it is possible to obtain a semi-analytical expression for radiation flux density in terms of elliptic integrals of first and second kind. This fact allows substantial reduction of the cost of numerical solution of RTE compared to the ray tracing method but maintaining the asymptotic accuracy. In case of strongly absorbing media the accurate treatment of attenuation factor is needed which is accomplished by the consecutive nearest neighbor search algorithm. The overall cost of view-factor approach is two orders of magnitude lower than the ray tracing method using proposed techniques for the nearest neighbor search.

The concept of the view-factor approach does not rely on the approximation of thermodynamic properties from the gasdynamic solution. Radiation energy exchange is calculated directly between emitting and receiving elements. This advantage eliminates the interpretation of thermodynamic and optical properties from gasdynamic grid to the tracing ray, required by the RTM. Additionally, the NNS algorithm is not involved in the radiation transfer model when the gas media is weakly absorbing.

7. CONCLUSION

Conclusions of the present work are divided into three categories, according to the number of objectives, articulated at the beginning of this manuscript. The first paragraph addresses the experience for integrating the finite rate chemistry model with compressible Navier-Stokes equations to predict the structure of diffusive flames in subsonic counter-flowing jets. The second paragraph presents the summary of computational results on the re-entry of RAM-C II probe. The third conclusion is about the development and implementation of a novel approach for ray tracing method and the view-factor approach for radiation transfer under the local thermodynamic equilibrium for the hypersonic re-entry phenomena.

The compressible Navier-Stokes equations are loosely coupled with the finite rate chemistry module to describe the combustion phenomenon in low speed counter-flowing jets. The simulation results are verified by comparison with an incompressible solution via the artificial compressibility method. A comprehensive study of the chemical mechanism, boundary conditions, global strain rate and difference in the numerical scheme due to the dilatation term is conducted. A satisfactory agreement for the flame thickness, temperature and species concentrations between the present approach and the reference solution has been established.

An extinction of the flame is observed at a global strain rate higher than 1000 s^{-1}. The time evolution of species concentration during the extinction indicates that diminishing of the OH radical reflects the decrease of temperature in the flame front. The rapid temperature drop is observed at 790 K and is recognized as the explosion limit at the atmospheric

pressure.

Application of the compressible Navier-Stokes equations to a flow with an extremely low Mach number is probably beyond the practical range of the present approach. This is confirmed by a maximum of 30-% difference in the flame thickness compared to the conventional approach. The solutions by compressible Navier-Stokes equations give a steeper profile for the axial component of velocity, while the solution by the reference approach exhibits a nearly linear pattern. This difference leads to a thinner flame than in the incompressible counterpart.

The non-equilibrium radiating flow field is rigorously investigated using compressible Navier-Stokes equations coupled with reactions of dissociation, ionization, recombination and the energy conservation equations for internal degrees of freedom. Two- and three-temperature models are applied to assess the electron concentration in the shock layer. A distinct advantage of the individual equation for the free electron energy is observed. The data by Langmuir probe and microwave reflectometers is successfully described by means of three-temperature model, Park chemical mechanism and Treanor-Marrone dissociation model. The uncertainty of the chemical composition and heating rates is studied for different types of species boundary conditions, models of the non-equilibrium dissociation and sets of chemical reactions.

The radiation heat transfer is studied for the laser-supported combustion waves as well as for the re-entry of the space vehicle. The Gauss-Lobatto quadrature is used to solve the line-of-sight radiation transfer equation. In the hypersonic flow a better accuracy of the approach is observed when the shock front is smeared along several grid points, as it occurs during the re-entry at high altitudes. Using the analytical distribution of temperature

in laser-induced combustion it was shown that Gauss-Lobatto quadrature retains a higher order accurate solution compared to the Newton-Cotes method even if using gas properties crudely approximated on the tracing ray. For both laser-supported combustion wave and re-entry problems Gauss-Lobatto quadrature allows to reduce the number of points along the tracing ray.

The efficiency of the ray tracing method is also significantly increased by introducing two space partition algorithms for the nearest neighbor search. These algorithms employ either a reference by the surface outward normal vector or an information from the previous nearest neighbor available by the ray tracing procedure. The consecutive search technique is generalized for both structured and unstructured grids and revealed a drastic decrease of the numerical operations required to locate the nearest neighbor.

Search process is combined with the clustered distribution of the integration points in the high gradient domain along the tracing rays by the Gauss-Lobatto polynomial. Number of points can be reduced by a factor of four when clustered near the shock wave and in the vicinity of surface. The overall performance of RTM is improved by a factor of 40-100 for the typical grid used in the re-entry computations. The efficiency is expected to increase with the number of nodes in the grids.

The radiation heating rates are reported for the RAM-C II re-entry vehicle. The integral radiation flux at the stagnation point is of 10-20 % of the total heating rate for the altitudes between 61 and 81 km. The radiation transfer model consists of 96 optical groups unevenly distributed in the infrared-ultraviolet spectrum. The calculations are performed under the assumption of local thermodynamic equilibrium, thus the present heating rates should be considered as the upper limit values.

Finally, the radiation transfer equation is solved by means of the view-factor approach. A semi-analytical expression for the spectral flux density is obtained for the axisymmetric geometry in the weakly absorbing media. In this case, the cost of VF is comparable with the tangent slab approximation. The interpretation of thermodynamic properties from the flow field is not required since the VF approach computed the radiation transfer directly between exchanging elements, which is a tremendous advantage over the RTM.

Future work will concentrate on the high fidelity models of air thermochemistry and radiation transfer. The kinetics of molecular nitrogen and nitrogen/oxygen mixtures will be considered by the concept of a potential energy surface, accurately resolving vibrational and rovibrational transitions. This approach will verify and designate the applicability of the multi-temperature model. Accurately resolved state-to-state kinetics combined with the view-factor approach will open a new research possibility to build an efficient and accurate radiation transfer model.

Bibliography

Abramowitz, M. and I. A. Stegun (1964). *Handbook of mathematical functions with formulas, graphs, and mathematical tables*, Volume 55 of *National Bureau of Standards Applied Mathematics Series*. Washington, D.C.: U.S. Government Printing Office.

Anderson, D. A., J. C. Tannehill, and R. H. Pletcher (2012). *Computational fluid mechanics and heat transfer*. New York: CRC Press.

Anderson, J. (1989). *Hypersonic and High Temperature Air Gas Dynamics*. Reston, VA: McGraw Hill, Inc.

Andrienko, D., S. Surzhikov, and J. Shang (2012). Three-dimensional radiative heating of descent space vehicle based on spherical harmonics method with unstructured grids. In *Proceedings of the 50th AIAA Aerospace Sciences Meeting, AIAA-2012-653*.

Andrienko, D. A. and S. T. Surzhikov (2012). P1 approximation applied to the radiative heating of descent spacecraft. *Journal of Spacecraft and Rockets 49*(6), 1088–1098.

Andrienko, D. A., S. T. Surzhikov, and J. S. Shang (2013). Spherical harmonics method applied to the multi-dimensional radiation transfer. *Computer Physics Communications 184*(10), 2287–2298.

Anfimov, N., Y. A. Dem'yanov, Y. A. Zavernyaev, G. Zalogin, V. Kamenshchikov, Y. A. Plastinin, S. Surzhikov, and B. Khmelinin (1981). On the measurement of some parameters of planetary atmospheres by means of the radiation generated by the descent of landers. *Fluid Dynamics 16*(1), 25–34.

Appleton, J. and K. Bray (1964). The conservation equations for a nonequilibrium plasma. *J. Fluid Mech 20*(4), 659–672.

Arya, S., D. M. Mount, N. S. Netanyahu, R. Silverman, and A. Wu (1994). An optimal algorithm for approximate nearest neighbor searching. In *Proceedings of the 50th annual ACM-SIAM symposium on Discrete algorithms*, pp. 573–582. Society for Industrial and Applied Mathematics.

Arya, S., D. M. Mount, N. S. Netanyahu, R. Silverman, and A. Y. Wu (1998). An optimal algorithm for approximate nearest neighbor searching fixed dimensions. *Journal of the ACM 45*(6), 891–923.

Beam, R. M. and R. Warming (1978). An implicit factored scheme for the compressible navier-stokes equations. *AIAA journal 16*(4), 393–402.

Bilger, R. (1976). The structure of diffusion flames. *Combustion Science and Technology 13*(1-6), 155–170.

Bird, G. (1989). Computation of electron density in high altitude re-entry flows. In *Proceedings of the 20th Fluid Dynamics, Plasma Dynamics and Lasers Conference, AIAA 1989-1882*. AIAA.

Bird, G. A. (1994). *Molecular gas dynamics and the direct simulation of gas flows*. Clarendon.

Bird, R. and W. Stewart (2007). *Transport phenomena*. New York: John Wiley and Sons.

Bortner, M. H. (1966). Suggested standard chemical kinetics for flow field calculations-a consensus opinion. *AMRAC Proceedings 14*(Part 1), 569–581.

Bose, D. and G. V. Candler (1997). Simulation of hypersonic flows using a detailed nitric oxide formation model. *Physics of Fluids 9*(4), 1171–1181.

Bose, D. and M. J. Wright (2004). View-factor based radiation transport in a hypersonic shock layer. *Journal of thermophysics and heat transfer 18*(4), 553–555.

Bourdon, A. and A. Bultel (2007). Detailed and simplified kinetic schemes for high enthalpy air flows and their influence on catalycity studies. DTIC Document RTO-EN-AVT-142, NATO.

Bourdon, A. and P. Vervisch (1997). Electron-vibration energy exchange models in nitrogen plasma flows. *Physical Review E 55*(4), 4634.

Boyd, I. D. (2007). Modeling of associative ionization reactions in hypersonic rarefied flows. *Physics of Fluids 19*(9), 096102.

Burgoyne, J. and F. Weinberg (1953). A method of analysis of a plane combustion wave. In *Proceeding of the 4th International Symposium on Combustion*, pp. 294.

Burke, S. and T. Schumann (1948). Diffusion flames. In *Proceedings of the Symposium on Combustion*, Volume 1, pp. 2–11. Elsevier.

Burke, S. P. and T. E. W. Schumann (1928). Diffusion flames. *Ind. Eng. Chem 20*, 998–1004.

Candler, G. V. and R. W. MacCormack (1991). Computation of weakly ionized hypersonic flows in thermochemical nonequilibrium. *Journal of Thermophysics and Heat Transfer 5*(3), 266–273.

Capitelli, M., I. Armenise, D. Bruno, M. Cacciatore, R. Celiberto, G. Colonna, O. De Pascale, P. Diomede, F. Esposito, and C. Gorse (2007). Non-equilibrium plasma kinetics: a state-to-state approach. *Plasma Sources Science and Technology 16*(1), S30.

Capitelli, M., C. M. Ferreira, A. I. Osipov, and B. F. Gordiets (2000). *Plasma kinetics in atmospheric gases*. Springer.

Capitelli, M., C. Gorse, S. Longo, and D. Giordano (2000). Collision integrals of high-temperature air species. *Journal of thermophysics and heat transfer 14*(2), 259–268.

Carnahan, B., H. A. Luther, and J. O. Wilkes (1969). *Applied numerical methods*, Volume 2. Wiley New York.

Chandrasekhar, S. (1960). *Radiative transfer*. Courier Dover Publications.

Chernyi, G., S. Losev, S. Macheret, and B. Potapkin (2002). *Physical and chemical processes in gas dynamics: cross sections and rate constants, Vol. 1*, Volume 196. AIAA.

Chorin, A. J. (1967). A numerical method for solving incompressible viscous flow problems. *Journal of computational physics 2*(1), 12–26.

Coffee, T. and J. Heimerl (1981). Transport algorithms for premixed, laminar steady-state flames. *Combustion and Flame 43*, 273–289.

Conrad, R., Y. P. Raizer, and S. Sarzhikov (1996). Continuous optical discharge stabilized by gas flow in weakly focused laser beam. *AIAA journal 34*(8), 1584–1588.

Cover, T. and P. Hart (1967). Nearest neighbor pattern classification. *Information Theory, IEEE Transactions on 13*(1), 21–27.

Curtiss, C. F. and J. O. Hirschfelder (1949). Transport properties of multicomponent gas mixtures. *The Journal of Chemical Physics 17*, 550.

Dafermos, C. M. (2005). Hyperbolic conservation laws in continuum physics, volume 325 of grundlehren der mathematischen wissenschaften [fundamental principles of mathematical sciences].

Davison, B. and J. B. Sykes (1957). *Neutron transport theory*. Clarendon Press Oxford.

Dirac, P. A. M. (1981). *The principles of quantum mechanics*. Oxford university press.

Dixon-Lewis, G. (1979). Kinetic mechanism, structure and properties of premixed flames in hydrogen-oxygen-nitrogen mixtures. *Philosophical Transactions for the Royal Society of London. Series A, Mathematical and Physical Sciences 292*, 45–99.

Dombrovsky, L. A. (1996). *Radiation heat transfer in disperse systems*. Begell House New York.

Domingo, P., A. Bourdon, and P. Vervisch (1995). Study of a low pressure nitrogen plasma jet. *Physics of Plasmas (1994-present) 2*(7), 2853–2862.

Douglas, J. and J. E. Gunn (1964). A general formulation of alternating direction methods. *Numerische Mathematik 6*(1), 428–453.

Dunn, M. G. and S. Kang (1973). Theoretical and experimental studies of reentry plasmas. Tech. Report NASA CR-2232, NASA.

Einstein, T. H. (1963a). Radiant heat transfer to absorbing gases enclosed between parallel flat plates with flow and conduction. Technical report, National Aeronautics and Space Administration.

Einstein, T. H. (1963b). Radiant heat transfer to absorbing gases enclosed in a circular pipe with conduction, gas flow, and internal heat generation. Technical report, National Aeronautics and Space Administration.

Evans, J. S. and C. J. Schexnayder (1980). Influence of chemical kinetics and unmixedness on burning in supersonic hydrogen flames. *AIAA Journal 18*(2), 188–193.

Farbar, E., I. D. Boyd, and A. Martin (2013). Numerical prediction of hypersonic flowfields including effects of electron translational nonequilibrium. *Journal of Thermophysics and Heat Transfer 27*(4), 593–606.

Farbar, E., A. Martin, I. Boyd, and M. Kim (2011). Investigation of the effects of electron translational nonequilibrium on numerical predictions of hypersonic flow fields. In *Proceedings of the 42nd AIAA Thermophysics Conference, AIAA 2011-3136*.

Feldick, A., M. Modest, D. Levin, P. Gnoffo, and C. Johnston (2009). Examination of

coupled continuum fluid dynamics and radiation in hypersonic simulations. *AIAA Paper 475*, 2009.

Ferziger, J., H. Kaper, and E. P. Gross (1973). Mathematical theory of transport processes in gases. *American Journal of Physics 41*, 601.

Fridman, A. (2008). *Plasma chemistry*. Cambridge University Press.

Galvez, M. (2005). Ray-tracing model for radiation transport in three-dimensional lte systems. *Journal of Physics D: Applied Physics 38*(17), 3011.

Gardiner, W. C. (2000). *Gas-phase combustion chemistry*. Springer.

Gautschi, W. (2004). *Orthogonal polynomials: computation and approximation*. Oxford university press.

Gnoffo, P. A. (1986). Application of program laura to three-dimensional aotv flowfields. In *Proceedings of the 24th AIAA, Aerospace Sciences Meeting, AIAA 1986-565*.

Gnoffo, P. A., R. Gupta, and J. L. Shinn (1989). Conservation equations and physical models for hypersonic air flows in thermal and chemical nonequilibrium. Tech. Report NASA-2867, NASA.

Goody, R. M. and Y. L. Yung (1996). *Atmospheric radiation: theoretical basis*. New York: Oford University Press.

Gorshkov, A. (2010). The simulation of ultraviolet radiation under conditions of re-entry of space vehicle from near-earth orbit. *High Temperature 48*(1), 12–22.

Goulard, R. (1961). The coupling of radiation and convection in detached shock layers. *Journal of Quantitative Spectroscopy and Radiative Transfer 1*(3), 249–257.

Grantham, W. L. (1970). Flight results of a 25000-foot-per-second reentry experiment using microwave reflectometers to measure plasma electron density and standoff distance. Technical Report NASA TN D-6062, National Aeronautics and Space Administration.

Grasso, F. and G. Capano (1995). Modeling of ionizing hypersonic flows in nonequilibrium. *Journal of spacecraft and Rockets 32*(2), 217–224.

Gupta, R., J. Yos, R. Thompson, and K.-P. Lee (1990). A review of reaction rates and thermodynamic and transport properties for an 11-species air model for chemical and thermal nonequilibrium calculations to 30,000 k. Tech. Report Reference Publication 1232, NASA.

Haas, B. L. and I. D. Boyd (1993). Models for direct monte carlo simulation of coupled vibration–dissociation. *Physics of Fluids A: Fluid Dynamics (1989-1993) 5*(2), 478–489.

Hammerling, P. (1960). *Ionization effects of precursor radiation from shocks in air*. Avco-Everett Research Laboratory, Avco Corporation.

Harlow, F. H. and J. E. Welch (1965). Numerical calculation of time-dependent viscous incompressible flow of fluid with free surface. *Physics of fluids 8*, 2182.

Harten, A. (1983). High resolution schemes for hyperbolic conservation laws. *Journal of computational physics 49*(3), 357–393.

Hirshfelder, J. O., R. B. Bird, and C. F. Curtiss (1964). *Molecular theory of gases and liquids*. Wiley.

Hottel, H. and E. Cohen (1958). Radiant heat exchange in a gas-filled enclosure: Allowance for nonuniformity of gas temperature. *AIChE Journal 4*(1), 3–14.

Huang, P. and T. Coakley (1992). An implicit navier-stokes code for turbulent flow modeling. In *Proceedings of the AIAA Materials Specialist Conference-Coating Technology for Aerospace Systems, AIAA 1992-547*, Volume 1.

Ismail, F., P. Roe, and H. Nishikawa (2009). A proposed cure to the carbuncle phenomenon. In H. Deconinck and E. Dick (Eds.), *Computational Fluid Dynamics 2006*, pp. 149–154. Springer Berlin Heidelberg.

Jackson, J. and P. Nielsen (1974). Role of radiative transport in the propagation of laser supported combustion waves. *AIAA Journal 12*(11), 1498–1501.

Jeans, J. (1917). The equations of radiative transfer of energy. *Monthly Notices of the Royal Astronomical Society 78*, 28–36.

Jones, W. L. and A. E. Cross (1972). Electrostatic-probe measurements of plasma parameters for two reentry flight experiments at 25000 feet per second. Technical report, National Aeronautics and Space Administration.

Josyula, E. and W. F. Bailey (2003). Governing equations for weakly ionized plasma flowfields of aerospace vehicles. *Journal of Spacecraft and Rockets 40*(6), 845–857.

Katta, V. (2011). Private communications.

Katta, V., L. Goss, and W. Roquemore (1994). Effect of nonunity lewis number and finite-rate chemistry on the dynamics of a hydrogen-air jet diffusion flame. *Combustion and Flame 96*(1), 60–74.

Katta, V. R., S. Hu, P. Wang, R. W. Pitz, W. M. Roquemore, and J. R. Gord (2007). Investigations on double-state behavior of the counterflow premixed flame system. *Proceedings of the Combustion Institute 31*(1), 1055–1066.

Katta, V. R. and W. M. Roquemore (2008). Calculation of multidimensional flames using large chemical kinetics. *Aiaa Journal 46*(7), 1640–1650.

Katta, V. R., W. M. Roquemore, and J. Gord (2009). Examination of laminar-flamelet concept using vortex/flame interactions. *Proceedings of the Combustion Institute 32*(1), 1019–1026.

Keller, J. B. and D. Givoli (1989). Exact non-reflecting boundary conditions. *Journal of computational physics 82*(1), 172–192.

Kirkbey, L. and R. Schmitz (1966). An analytical study of the stability of a laminar diffusion flame. *Combustion and Flame 10*(3), 205–220.

Klosterman, E. L. and S. R. Byron (1974). Measurement of subsonic laser absorption wave propagation characteristics at 10.6 μm. *Journal of Applied Physics 45*(11), 4751–4759.

Knab, O., H.-H. Fruhauf, and E. Messerschmid (1995). Uranus/cvcv-model validation by means of thermo-chemical nonequilibrium nozzle airflow calculations. In *Aerothermodynamics for space vehicles*, Volume 367, pp. 129.

Kong, R., M. Ambrose, and J. Spanier (2008). Efficient, automated monte carlo methods for radiation transport. *Journal of computational physics 227*(22), 9463–9476.

Krier, H. and R. Glumb (1984). Concepts and status of laser-supported rocket propulsion. *Journal of Spacecraft and Rockets 21*(1), 70–79.

Kwak, D., J. Chang, S. P. Shanks, and S. R. Chakravarthy (1986). A three-dimensional incompressible navier-stokes flow solver using primitive variables. *AIAA journal 24*(3), 390–396.

Landahl, M. T. and E. Mollo-Christensen (1992). *Turbulence and random processes in fluid mechanics*. Cambridge University Press.

Landau, L. and E. Teller (1936). Zur theorie der schalldispersion. *Phys. Z. Sowjetunion 10*(1), 34–43.

Laux, C. (2002). Radiation and nonequilibrium collisional-radiative models.

Lee, J.-H. (1984). Basic governing equations for the flight regimes of aeroassisted orbital transfer vehicles. In *Proceedings of the 19th AIAA Thermophysics Conference, AIAA 84-1729*.

Liu, Y., D. Prabhu, K. A. Trumble, D. Saunders, and P. Jenniskens (2010). Radiation modeling for the reentry of the stardust sample return capsule. *Journal of Spacecraft and Rockets 47*(5), 741–752.

Lockwood, M. K. (2003). Titan aerocapture systems analysis. *AIAA Paper 4799*, 20–23.

Losev, S., V. Makarov, and M. Y. Pogosbekyan (1995). Model of the physico-chemical kinetics behind the front of a very intense shock wave in air. *Fluid dynamics 30*(2), 299–309.

Losev, S. A., V. N. Makarov, and V. S. Nikolsky (1994). Thermochemical nonequilibrium kinetic models in strong shock waves on air. In *Proceedings of the 6th AIAA and ASME, Joint Thermophysics and Heat Transfer Conference, AIAA 1994-1990*.

Ma, A. (1995). Generalized zoning method in one-dimensional participating media. *Journal of heat transfer 117*, 520.

MacCormack, R. W. (2011). The carbuncle cfd problem. In *Proceedings of the 49th AIAA Aerospace Sciences Meeting, AIAA 2011-381*.

Macheret, S. and A. Fridman (1994). Mechanisms of nonequilibrium dissociation of diatomic molecules. In *Proceedings of the 6th AIAA and ASME, Joint Thermophysics and Heat Transfer Conference, AIAA 1994-1984*.

Magin, T. (2004). *A Model for Inductive Plasma Wind Tunnels.* Ph. D. thesis, von Karman Institute for Fluid Dynamics, Rhode-St-Genese, Belgium.

Mark, J. C. (1947). *The spherical harmonic method*. National Research Council of Canada, Atomic Energy Project, Division of Research.

Marrone, P. V. and C. E. Treanor (1963). Chemical relaxation with preferential dissociation from excited vibrational levels. *Physics of Fluids 6*, 1215.

Marshak, R. (1947). Note on the spherical harmonic method as applied to the milne problem for a sphere. *Physical Review 71*(7), 443.

Mason, E. and S. Saxena (1958). Approximate formula for the thermal conductivity of gas mixtures. *Physics of Fluids 1*(5), 361.

McNames, J. (2001). A fast nearest-neighbor algorithm based on a principal axis search tree. *Pattern Analysis and Machine Intelligence, IEEE Transactions on 23*(9), 964–976.

Michalak, K. and C. Ollivier-Gooch (2008, January). Limiters for unstructured higher-order accurate solutions of the euler equations. In *Proceedings of the 46th Aerospace Sciences Meetings, AIAA 2008-776*, pp. –. American Institute of Aeronautics and Astronautics.

Mihalas, D. and B. W. Mihalas (1999). *Foundations of radiation hydrodynamics*. Dover-Publications. com.

Millikan, R. C. and D. R. White (1963). Systematics of vibrational relaxation. *Journal of Chemical Physics 39*, 3209.

Mitchell, R. E., A. F. Sarofim, and L. Clomburg (1980). Experimental and numerical investigation of confined laminar diffusion flames. *Combustion and flame 37*, 227–244.

Modest, M. F. (2003). *Radiative heat transfer*. Academic press.

Moin, P. and K. Mahesh (1998). Direct numerical simulation: a tool in turbulence research. *Annual Review of Fluid Mechanics 30*(1), 539–578.

Monat, J., R. Hanson, and C. Kruger (1979). Shock tube determination of the rate coefficient for the reaction n¡ sub¿ 2¡/sub¿+ o no+ n. In *International Symposium on Combustion*, Volume 17, pp. 543–552. Elsevier.

Olejniczak, J., M. Wright, D. Prabhu, N. Takashima, B. Hollis, E. V. Zoby, and K. Sutton (2003). An analysis of the radiative heating environment for aerocapture at titan. *AIAA paper 4953*(2003), 250.

Oliger, J. and A. Sundström (1978). Theoretical and practical aspects of some initial boundary value problems in fluid dynamics. *SIAM Journal on Applied Mathematics 35*(3), 419–446.

Olynick, D., Y.-K. Chen, and M. E. Tauber (1999). Aerothermodynamics of the stardust sample return capsule. *Journal of Spacecraft and Rockets 36*(3), 442–462.

Oran, E. S. and J. P. Boris (1980). Detailed modelling of combustion systems. Technical report, DTIC Document.

Palmer, G. E., T. White, and A. Pace (2011). Direct coupling of the neqair radiation and dplr cfd codes. *Journal of Spacecraft and Rockets 48*(5), 836–845.

Panesi, M. (2009). *Physical models for nonequilibrium plasma flow simulations at high speed re-entry conditions*. Ph. D. thesis, University of Pisa, Pisa, Italy.

Panesi, M., T. Magin, A. Bourdon, A. Bultel, and O. Chazot (2009). Fire ii flight experiment analysis by means of a collisional-radiative model. *Journal of Thermophysics and Heat Transfer 23*(2), 236–248.

Park, C. (1984). Problems of rate chemistry in the flight regimes of aeroassisted orbital transfer vehicles. In *Proceedings of the 19th AIAA Thermophysics Conference, AIAA 84-1730*.

Park, C. (1985). On convergence of computation of chemically reacting flows. In *Proceedings of the 23rd Aerospace Sciences Meeting, AIAA 85-0247*, Volume 1.

Park, C. (1988). Two-temperature interpretation of dissociation rate data for n2 and o2. In *Proceedings of the 26th Aerospace Sciences Meetings, AIAA 1988-458*.

Park, C. (1989). *Nonequilibrium hypersonic aerothermodynamics*. New York: Wiley.

Park, C. (1993). Review of chemical-kinetic problems of future nasa missions. i-earth entries. *Journal of Thermophysics and Heat Transfer 7*(3), 385–398.

Park, C., R. L. Jaffe, and H. Partridge (2001). Chemical-kinetic parameters of hyperbolic earth entry. *Journal of Thermophysics and Heat Transfer 15*(1), 76–90.

Peters, N. (1984). Laminar diffusion flamelet models in non-premixed turbulent combustion. *Progress in energy and combustion science 10*(3), 319–339.

Pletcher, R. H., J. C. Tannehill, and D. A. Anderson (2012). *Computational fluid mechanics and heat transfer*. CRC Press.

Pomraning, G. (1964). Variational boundary conditions for the spherical harmonics approximation to the neutron transport equation. *Annals of Physics 27*(2), 193–215.

Radziemski, L. J. and D. A. Cremers (1989). *Laser-induced plasmas and applications*, Volume 21. CRC Press.

Raizer, Y. P., V. I. Kisin, and J. E. Allen (1991). *Gas discharge physics*, Volume 1. Springer-Verlag Berlin.

Ralchenko, Y., A. Kramida, and J. Reader (2010). Nist atomic spectra database (version 4.0). Technical report, NIST.

Roe, P. L. (1981). Approximate riemann solvers, parameter vectors, and difference schemes. *Journal of computational physics 43*(2), 357–372.

Roper, F. (1977). The prediction of laminar jet diffusion flame sizes: Part i. theoretical model. *Combustion and Flame 29*, 219–226.

Rudy, D. H. and J. C. Strikwerda (1980). A nonreflecting outflow boundary condition for subsonic navier-stokes calculations. *Journal of Computational Physics 36*(1), 55–70.

Sarofim, A. F. and H. C. Hottel (1966). Radiative exchange among non-lambert surfaces. *Journal of Heat Transfer 88*, 37.

Scalabrin, L. C. and I. D. Boyd (2006). Numerical simulation of weakly ionized hypersonic flow for reentry configurations. In *Proceedings of the 9th AIAA/ASME Joint Thermophysics and Heat Transfer Conference, AIAA 2006-3773*.

Scott, C. D. (1975, Oct). Reacting shock layers with slip and catalytic boundary conditions. *AIAA Journal 13*(10), 1271–1278.

Shang, J. (2001). Recent research in magneto-aerodynamics. *Progress in Aerospace Sciences 37*(1), 1–20.

Shang, J. (2004). Three decades of accomplishments in computational fluid dynamics. *Progress in Aerospace Sciences 40*(3), 173–197.

Shang, J., D. Andrienko, P. Huang, and S. Surzhikov (2014). A computational approach for hypersonic nonequilibrium radiation utilizing space partition algorithm and gauss quadrature. *Journal of Computational Physics 266*, 1–21.

Shang, J., D. Andrienko, S. Surzhikov, and P. Huang (2013). An efficient computational approach to hypersonic nonequilibrium radiation utilizing gaussian quadrature and space partition. In *Proceedings of the 21st AIAA Computational Fluid Dynamics Conference, AIAA 2013-2587*.

Shang, J., V. Katta, and P. Huang (2010). Adaptive polynomial local refinement for resolving flame structure. In *Proceedings of the 40th Fluid Dynamics Conference and Exhibit, AIAA AIAA 2010-4437*.

Shang, J. and S. Surzhikov (2010). Simulating nonequilibrium flow for ablative earth reentry. *Journal of Spacecraft and Rockets 47*, 806–815.

Shang, J. and S. Surzhikov (2012). Nonequilibrium radiative hypersonic flow simulation. *Progress in Aerospace Sciences 53*, 46–65.

Shang, J., S. Surzhikov, and H. Yan (2012). Hypersonic nonequilibrium flow simulation based on kinetic models. *Frontiers in Aerospace Engineering 1*(1), 1–12.

Shang, J. S. and S. T. Surzhikov (2011). Simulating stardust earth reentry with radiation heat transfer. *Journal of Spacecraft and Rockets 48*(3), 385–396.

Sharma, S. P., W. M. Huo, and C. Park (1988). Rate parameters for coupled vibration-dissociation in a generalized ssh approximation.[schwarz, slawsky, and herzfeld]. Technical report, San Antonio, TX; AIAA.

Siegel, R. and J. R. Howell (2002). *Thermal radiation heat transfer*. New York: Taylor & Francis Group.

Smith, G. P., D. M. Golden, M. Frenklach, N. W. Moriarty, B. Eiteneer, M. Goldenberg, C. T. Bowman, R. K. Hanson, S. Song, W. C. Gardiner Jr, et al. (1999). Gri-mech 3.0. URL: http://www. me. berkeley. edu/gri_mech.

Smooke, M. D. (2013). The computation of laminar flames. *Proceedings of the Combustion Institute 34*(1), 65 – 98.

Smooke, M. D., R. E. Mitchell, and D. E. Keyes (1986). Numerical solution of two-dimensional axisymmetric laminar diffusion flames. *Combustion Science and Technology 67*(4-6), 85–122.

Soubrié, T., O. Rouzaud, and J. Hylkema (2006). Computation of weakly ionized atmospheric entry flows using an extended roe scheme. In *Computational Fluid Dynamics 2004*, pp. 805–810. Springer.

Surzhikov, S. (2000, June). Computing system for mathematical simulation of selective

radiation transfer. In *Fluid Dynamics and Co-located Conferences*, pp. –. American Institute of Aeronautics and Astronautics.

Surzhikov, S. (2002). Radiation modeling and spectral data.

Surzhikov, S. (2004a). Numerical simulation of heat radiation generated by entering space vehicle. In AIAA (Ed.), *Proceedings of the 37th AIAA Thermophysics Conference, AIAA 2004-2379*.

Surzhikov, S. (2004b). *Radition heat transfer in gases and plasma (in Russian)*. Bauman Moscow State Technical University.

Surzhikov, S. (2008). A study of the influence of kinetic models on calculations of the radiation-convective heating of a space vehicle in fire-ii flight experiment. *Russian Journal of Physical Chemistry B, Focus on Physics 2*(5), 814–826.

Surzhikov, S. (2009). Laser-supported combustion wave in the field of gravity. *High Temperature 47*(3), 307–319.

Surzhikov, S. (2011). Numerical simulation of spectral signature of bolide entering into earth atmosphere. In *Proceedings of the Fluid Dynamics and Co-located Conferences, AIAA 2011-3152*. American Institute of Aeronautics and Astronautics.

Surzhikov, S. (2012). Coupled radiative gasdynamic interaction and non-equilibrium dissociation for large-scale returned space vehicles. *Chemical Physics 398*, 56–63.

Surzhikov, S. (2014). Three dimensional simulation of shock layer ionization for ram-c ii flight tests, aiaa 2014-1078. In *Proceedings of the 52nd Aerospace Sciences Meeting*.

Surzhikov, S. and J. Shang (2011). Radiative and convective heating of orion space vehicles at earth orbital entries. In *49th AIAA Aerospace Sciences Meeting including the New Horizons Forum and Aerospace Exposition, AIAA 2011-251*.

Surzhikov, S., I. Sharikov, M. Capitelli, and G. Colonna (2006). Kinetic models of non-equilibrium radiation of strong air shock waves. In *Proceedings of the 44th AIAA Aerospace Sciences Meeting and Exhibit, AIAA 2006-586*, Volume 586, pp. 2006.

Surzhikov, S. T. (2003). Computing system for solving radiative gasdynamic problems of entry and re-entry space vehicles. In *Proceedings of the 1st International Workshop on Radiation of High Temperature Gases in Atmospheric Entry*, Volume 533, pp. 111–118.

Surzhikov, S. T. (2006). Spectral optical properties of highly ionized plasma for radiation gas dynamics. In *Proceedings of the 37th AIAA Plasmadynamics and Lasers Conference, AIAA 2006-3767*, Volume 3767.

Surzhikov, S. T., M. Capitelli, G. Colonna, and C. Gorse (2008). Radiative gas dynamic model of hydrogen laser-supported plasma generator. *Journal of Thermophysics and Heat Transfer 22*(1), 62–70.

Tchuen, G. and D. E. Zeitoun (2009). Effects of chemistry in nonequilibrium hypersonic flow around blunt bodies. *Journal of thermophysics and heat transfer 23*(3), 433–442.

Treanor, C. E. and P. V. Marrone (1962). Effect of dissociation on the rate of vibrational relaxation. *Physics of Fluids 5*, 1022.

Tret'yakov, P., G. Grachev, A. Ivanchenko, V. Krainev, A. Ponomarenko, and V. Tishchenko (1994). Stabilization of the optical discharge in a supersonic argon flow. In *Proceeidngs of the Reports of Academy of Sciences*, Volume 39, pp. 415–416.

Tsuji, H. (1982). Counterflow diffusion flames. *Progress in energy and combustion science 8*(2), 93–119.

Vanden Abeele, D. (2000). *An efficient computational model for inductively coupled air plasma flows under thermal and chemical non-equilibrium*. Ph. D. thesis, von Karman Institute for Fluid Dynamics/Katholieke Universiteit Leuven, Leuven, Belgium.

Vincenti, W. G. and C. H. Kruger (1965). *Introduction to physical gas dynamics*. New York: Wiley.

Vlasov, V., A. Gorshkov, R. Kovalev, and Y. A. Plastinin (1997). Theoretical studies of air ionization and no vibrational excitation in low density hypersonic flow around re-entry bodies. In *Proceedings of the AIAA 32nd Thermophysics Conference, AIAA 97-2582*.

Walpot, L. M. G. F. M. (2002). *Development and application of a hypersonic flow solver*. Ph. D. thesis, TU Delft.

Warnatz, J. (1981). Concentration-, pressure-, and temperature-dependence of the flame velocity in hydrogen-oxygen-nitrogen mixtures. *Combustion Science and Technology 26*(5-6), 203–213.

Whiting, E., C. Park, J. Arnold, and J. Paterson (1996). Neqair 96, nonequilibrium and equilibrium radiative transport and spectra program: User"s manual. Technical Report NASA-RP-1389, NASA.

Wray, K. L. (1961). Chemical kinetics of high temperature air. Technical report, Avco-Everett Research Laboratory, Avco Corporation.

Wright, M. J., D. Bose, and J. Olejniczak (2005). Impact of flowfield-radiation coupling on aeroheating for titan aerocapture. *Journal of Thermophysics and Heat Transfer 19*(1), 17–27.

Yee, H. (1981). Numerical approximation of boundary conditions with applications to inviscid equations of gas dynamics. Technical report, NASA.

Yee, H. C. (1987). Upwind and symmetric shock-capturing schemes. Tech. Report NASA-TM-89464, NASA Ames Research Center.

Yuen, W. and E. Takara (1994). Development of a generalized zonal method for analysis

of radiative transfer in absorbing and anisotropically scattering media. *Numerical Heat Transfer, Part B Fundamentals 25*(1), 75–96.

Zeldovich, I., G. I. Barenblatt, V. Librovich, and G. Makhviladze (1985). *Mathematical theory of combustion and explosions*. Consultants Bureau, New York, NY.

A. Appendix

Species and reaction data for hydrogen combustion

Reaction #	Reaction
1	$2H_2+O_2=2H_2O$

Table A.1: Reaction nomenclature, global single-step mechanism

Forward rates			Backward rates		
A	B	C	A	B	C
$1.0x10^{16}$	0	120000.34	0	0	0

Table A.2: Reaction rates, global single-step mechanism

Reaction #	Reaction	Reaction #	Reaction
1	$H_2+M=H+H+M$	9	$HO_2+M=H+O_2+M$
2	$O_2+M=O+O+M$	10	$H_2+O_2=OH+OH$
3	$H_2O+M=OH+H+M$	11	$H_2+O_2=H+HO_2$
4	$OH+M=O+H+M$	12	$OH+OH=H+HO_2$
5	$H_2O+O=OH+OH$	13	$H_2O+O=H+HO_2$
6	$H_2O+H=OH+H_2$	14	$H_2O+O_2=O+HO_2$
7	$O_2+H=OH+O$	15	$H_2O+O_2=OH+HO_2$
8	$H_2+O=OH+H$	16	$H_2O+OH=H_2+HO_2$

Table A.3: Reaction nomenclature, mechanism by Evans and Schexnayder

Reaction	Forward rates			Backward rates		
	A	B	C	A	B	C
1	$5.5x10^{18}$	-1	51987	$1.8x10^{18}$	-1	0
2	$7.2x10^{18}$	-1	59340	$4.0x10^{17}$	-1	0
3	$5.2x10^{21}$	-1.5	59386	$4.4x10^{20}$	-1.5	0
4	$8.5x10^{18}$	-1.0	50830	$7.1x10^{18}$	-1	0
5	$5.8x10^{13}$	0	9059	$5.3x10^{12}$	0	503
6	$8.4x10^{13}$	0	10116	$2.0x10^{13}$	0	2600
7	$2.2x10^{14}$	0	8455	$1.5x10^{13}$	0	0
8	$7.5x10^{13}$	0	5586	$3.0x10^{13}$	0	4429
9	$1.7x10^{16}$	0	23100	$1.1x10^{16}$	0	-440
10	$1.7x10^{13}$	0	24232	$5.7x10^{11}$	0	14922
11	$1.9x10^{13}$	0	24100	$1.3x10^{13}$	0	0
12	$1.7x10^{11}$	0.5	21137	$6x10^{13}$	0	0
13	$5.8x10^{11}$	0.5	28686	$3x10^{13}$	0	0
14	$3.7x10^{11}$	0.64	27840	$1x10^{13}$	0	0
15	$2.0x10^{11}$	0.5	36296	$1.2x10^{13}$	0	0
16	$1.2x10^{12}$	0.21	39815	$1.7x10^{13}$	0	12582

Table A.4: Reaction rates for mechanism by Evans and Schexnayder

Species	ε/k_b	σ	μ	α	Z_{rot}
H	8.60	2.8101	0	0	0
O	106.70	3.0500	0	0	0
H_2	59.70	2.8270	0	0.79	280
O_2	106.70	3.4670	0	1.60	38
N_2	281.27	3.1110	0	1.76	4
OH	71.40	3.7980	0	0	0
H_2O	809.10	2.6410	1.844	0	4
HO_2	809.10	2.6410	0	0	1
H_2O_2	289.30	4.1960	0	0	3.8

Table A.5: Kinetic properties of the species in the hydrogen-air flame

B. Appendix

View factor for cylindrical enclosure

$$\int \frac{(cosx+a)^3}{(cosx+b)^{3/2}}dx = C + \frac{2}{3}\frac{1}{(b^2-1)\left(\sqrt{b+cosx}\right)}\left[A-B\right],$$

where

$$A = \sqrt{\frac{b+cosx}{b+1}}\left[\left(3a^3b-9a^2+9ab-2b^2-1\right)F\left(\frac{x}{2}|\frac{2}{b+1}\right)\right] + \sqrt{\frac{b+cosx}{b+1}}\left(3a^3b-9a^2+9a\left(2b^2-1\right)-8b^3+5b\right)\left((b+1)\left(E\left(\frac{x}{2}|\frac{2}{b+1}\right)-bF\left(\frac{x}{2}|\frac{2}{b+1}\right)\right)\right),$$

$$B = sinx\left(3a^3-9a^2b+9ab^2-4b^3-b^2cosx+b+cosx\right).$$

C. Appendix

View factor for the re-entry body

$$\int \frac{(cosx+a)}{(cosx+b)^{3/2}}dx = C + A(b-a)\sin(x)$$
$$-A\left[(b+1)(b-a)\sqrt{\frac{b+\cos(x)}{b+1}}E\left(0.5x\left|\frac{2}{b+1}\right.\right)\right]$$
$$+A\left[\left(b^2-1.\right)\sqrt{\frac{b+\cos(x)}{b+1}}F\left(0.5x\left|\frac{2}{b+1}\right.\right)\right],$$

where

$$A = \frac{2}{\left(b^2-1\right)\sqrt{b+\cos(x)}}.$$